UNIVERSITÁ DEGLI STUDI DI TRIESTE

Sede Amministrativa del Dottorato di Ricerca

Facoltá di Scienze Matematiche Fisiche e Naturali

Dipartimento di Fisica

XXI^o CICLO DEL

DOTTORATO DI RICERCA IN FISICA

Organic molecules at metal surfaces: the role of functional groups in self-assembly and charge transfer.

(Settore disciplinare: FIS03-Fisica della Materia)

DOTTORANDO

Martina Dell'Angela

COORDINATORE DEL COLLEGIO DEI DOCENTI

CHIAR.MO PROF. **Gaetano Senatore**

Universitá degli Studi di Trieste

RELATORE

CHIAR.MO PROF. **Alberto Morgante**

Universitá degli Studi di Trieste

ANNO ACCADEMICO 2007/2008

Abstract

The understanding of the interaction of organic molecules with metal surfaces is crucial for tailoring the desired properties of future devices that can be employed for molecular electronics or biomedical applications. Self-assembly of complex supramolecular structures and charge transfer through molecular films or even through single molecules are some of the properties that have recently attracted much interest both for possible applications and for more fundamental studies.

The molecule-surface interaction takes place thanks to the functional groups that constitute the molecule. The choice of appropriate functional groups of the molecules allows their use as building blocks in the fabrication of complicate architectures [1]. In fact, the functional entities can influence molecule-molecule and molecule-surface interactions, governing the self-assembly of the molecules on the surface.

In particular, in the thesis I will report on the characterization by means of Helium Atom Scattering (HAS), X-ray Photoemission Spectroscopy (XPS), Near Edge X-ray Absorption Fine Structure (NEXAFS) and Scanning Tunneling Microscopy (STM) of the self-assembly in ultra high vacuum (UHV) conditions of L-methionine molecules on different metal substrates (Ag(111), Cu(111), Au(111), Au(110)). L-methionine is an amino acid with three functional groups which can interact with the substrate or with other molecules: the amino (-NH_2), the carboxyl (-COOH) and the thioether (-S-). Moreover, the first two can change their charge state in a protonated amino group (-NH_3^+) and a deprotonated carboxyl group (-COO^-): the molecules are called zwitterionic and it is allowed the formation of hydrogen bonds between them. Hydrogen bonding between zwitterionic molecules is responsible for the crystallization in the solid state. In the thesis I have studied how, depending on the choice of the substrate and the growth conditions, L-methionine molecules form assemblies with different morphologies and different chemical states of the building blocks. L-methionine molecules deposited on Ag(111) and Au(111) are in the zwitterionic state and interact strongly via hydrogen bonding forming dimers of molecules. The weak interaction with the

substrate allows the organization of these dimers in extended bidimensional nanogratings composed of chains of length extending in the micrometer range and with tunable periodicity across the chains. At temperatures below 270K, L-methionine on Cu(111) forms short aggregates of zwitterionic dimers. By increasing the substrate temperature above 300K the charge state of the amino group changes and also the interaction with the surface. Molecules are anionic (-NH_2 and -COO^-) and form again charged nanogratings. The anionic state of the molecules can also be obtained on the Au(110) surface, where the interaction of the amino and thioether groups with the gold inhibits the formation of zwitterionic dimers via hydrogen bonding.

The functional groups in the molecules can also influence their transport properties. The final goal of miniaturization in molecular electronics research is the formation and characterization of a nanoelectronic device in which a molecule between two electrodes plays the role of an active conducting element. In such a device the interaction between the functional groups anchoring the molecule to the electrodes and the electrodes is a crucial element in order to understand and control the conduction. Recent STM-break junction experiments [2] have shown that Au-molecule-Au contacts with amino (-NH2) terminated molecules are better defined than Au-molecule-Au contacts formed with thiol (-SH) terminated molecules [3]. The strong interaction of thiols with gold surfaces is well known in literature and the self-assembly of thiolated molecules is widely employed in many applications. In contrast, the weak interaction of amino terminated molecules with gold is poorly studied. Theoretical calculations suggest that the amine lone pair is responsible for bonding and that it prefers to bind to undercoordinated gold atoms. Within this framework, in the thesis I report on the study of growth of thin films of 1,4-benzenediamine and p-toluidine on two different Au surfaces, where the atoms present different coordination: Au(111) and Au(110). Both molecules interact more strongly with the low coordination (110) surface. By means of Resonant Photoemission Spectroscopy (RPES) it has been possible to disentangle molecular orbitals and determine the ones involved in the charge transfer at the surface. In both cases the charge transfer involves states localized also on the nitrogen atoms indicating a possible interaction of the molecule with the surface through nitrogen atoms. I also studied the assembly of three benzene substituted diamines on Au(111). These results complement very well the results obtained from conduction experiments of different amine-terminated molecules and combined with theoretical investigations can help understanding the basics of the molecular charge transport mechanism.

[1] Barth J.V., Costantini G., Kern K., Nature, 437 (2005) 671
[2] Venkataraman L., Klare J. E., Nuckolls C., Hybertsen M. S., Steigerwald M. L., Nature, 442 (7105), 904 (2006)
[3] Schreiber F., Progress in Surface Science, 65 (5-8) (2000) 151

Riassunto

Lo studio dell'interazione di molecole organiche con superfici metalliche é di fondamentale importanza per la progettazione di futuri dispositivi che possiedano proprietà ben controllabili in modo tale che possano essere usati per l'elettronica molecolare o per applicazioni biomediche. L'autoassemblaggio di complesse strutture "supramolecolari" e il trasferimento di carica attraverso film molecolari o anche attraverso singole molecole sono alcune delle proprietà che hanno attratto di recente grande interesse sia per le possibili applicazioni future che per studi di tipo più fondamentale.

L'interazione molecola-superficie avviene attraverso i gruppi funzionali che costituiscono le molecole. Molecole con appropriate funzionalizzazioni possono essere usate come mattoni elementari nella fabbricazione di architetture complesse [1]. Infatti, tali gruppi funzionali possono influenzare le interazioni del tipo molecola-molecola e molecola-superficie che governano l'autoassemblaggio delle molecole sulla superficie.

In particolare, in questa tesi riporterò circa la caratterizzazione mediante diffrazione di atomi di elio (HAS), spettroscopia di fotoemissione di raggi X (XPS), misure di assorbimento di raggi X (NEXAFS) e microscopia ad effetto tunnel (STM) dell'autoassemblaggio in condizioni di ultra alto vuoto (UHV) di molecole di L-metionina su diversi substrati metallici (Ag(111), Cu(111), Au(111), Au(110)). La molecola di L-metionina è un amminoacido che presenta tre gruppi funzionali i quali possono interagire con il substrato o con altre molecole: il gruppo amminico (-NH_2), il gruppo carbossilico (-COOH) e il gruppo tioetere (-S-). I primi due possono inoltre cambiare il loro stato di carica originando un gruppo amminico protonato (-NH_3^+) e un gruppo carbossilico deprotonato (COO^-): in tal caso le molecole sono dette zwitterioniche ed è permessa la formazione di legami a idrogeno tra esse. I legami a idrogeno tra molecole zwitterioniche sono responsabili della loro cristallizzazione nello stato solido. In questa tesi ho studiato come, a seconda della scelta del substrato e delle condizioni di cescita, le molecole di L-metionina formino strutture assemblate che presentano diverse morfologie e diversi stati chimici delle molecole costituenti. Le molecole di L-metionina

depositate su Ag(111) e Au(111) sono zwitterioniche e interagiscono fortemente tra di loro tramite legami a idrogeno a formare dimeri di molecole sulla superficie. La debole interazione con il substrato permette l'organizzazione di questi dimeri in estesi reticoli bidimensionali di dimensione nanometrica composti da catene di lunghezza nel range micrometrico e con spaziatura tra le catene controllabile. A temperature sotto 270K, le molecole di L-metionina su Cu(111) formano corti aggregati di dimeri zwitterionici. Aumentando la temperatura del substrato oltre 300K lo stato di carica del gruppo amminico cambia e quindi l'interazione con la superficie. Le molecole sono anioniche (-NH_2 e COO^-) e formano di nuovo reticoli carichi. Lo stato anionico delle molecole si può ottenere anche sulla superficie di Au(110) dove l'interazione dei gruppi amminico e tioetere con l'oro inibisce la formazione di dimeri zwitterionici via legami a idrogeno.

I gruppi funzionali nelle molecole possono anche influenzare le loro proprietà di trasporto. Lo scopo finale della miniaturizzazione nella ricerca nel campo dell'elettronica molecolare è la formazione e caratterizzazione di un dispositivo nanoelettronico in cui una molecola immobilizzata tra due elettrodi gioca il ruolo di elemento conduttivo attivo. In tale dispositivo il controllo dell'interazione tra i gruppi funzionali che tengono la molecola attaccata gli elettrodi e gli elettrodi è un elemento cruciale per la comprensione e il controllo della conduzione. Recenti esperimenti del tipo STM break junction [2] hanno motrato che contatti del tipo Au-molecola-Au con molecole con terminazioni amminiche (NH_2) sono meglio definiti che contatti del medesimo tipo con molecole con terminazione tiolica (-SH) [3]. La forte interazione dei tioli con superfici d'oro è ben nota in letteratura e l'autoassemblaggio di molecole con terminazione tiolica è largamente utilizzato in molte applicazioni. In contrasto, la debole interazione di molecole con terminazione amminica con superfici d'oro è stata poco studiata. Recenti calcoli teorici hanno previsto che le molecole si legano alla superficie d'oro attraverso il "lone pair" localizzato sull'azoto e che sono preferiti i legami con atomi di oro di bassa coordinazione. In particolare, nella tesi riporterò i risultati dello studio della crescita di film sottili di 1,4-benzenediamina e p-toluidina su due diverse superfici d'oro, i cui atomi di superficie presentano diversa coordinazione: Au(111) e Au(110). Ambedue le molecole interagiscono più fortemente con la superficie di bassa coordinazione (110). Tramite la tecnica di fotoemissione risonante (RPES) è stato possibile individuare gli orbitali molecolari e determinare quelli coinvolti nel trasferimento di carica all'interfaccia. In ambedue i casi il trasferimento di carica coinvolge stati che sono localizzati anche sull'atomo di azoto, il che indica una possibile interazione della molecola con la superficie attraverso i gruppi amminici. Ho anche studiato l'assemblaggio su Au(111) di tre diverse benzene-diamine con

diversi sostituenti legati all'anello. Questi risultati sono un complemento ai risultati ottenuti da esperimenti di conduzione di molecole con diverse terminazioni amminiche e combinati con le investigazioni teoriche possono aiutare nella comprensione dei fondamenti dei meccanismi di trasporto di carica nelle molecole.

[1] Barth J.V., Costantini G., Kern K., Nature, 437 (2005) 671
[2] Venkataraman L., Klare J. E., Nuckolls C., Hybertsen M. S., Steigerwald M. L., Nature, 442 (7105), 904 (2006)
[3] Schreiber F., Progress in Surface Science, 65 (5-8) (2000) 151

To my parents.

Contents

Chapter 1

Introduction.

Self-assembly can be defined as the spontaneous formation of complex hierarchical structures from pre-designed building blocks [1]. It is a very general principle in nature and can occur with components having sizes from the molecular to the macroscopic range, provided that appropriate conditions are met [2]. Self assembly is scientifically interesting and technologically important for several reasons. First of all it is centrally important in life: in fact the cell contains an astonishing range of complex structures such as lipid membranes, folded proteins, structured nucleic acids, protein aggregates, molecular machines and many others, that are formed by self-assembly. Moreover it provides routes to create a range of materials with regular structures, such as molecular crystals, liquid crystals and semi crystalline and phase separated polymers. There is a great potential for its use in nanomaterials and in condensed matter science since it offers one of the most general strategies now available for generating nanostructures.

Molecules are the most elementary building blocks that can form self-assembled structures. Molecular self-assembly is ubiquitous in chemistry, materials science and biology. The formation of molecular crystals, colloids, lipid bilayers, phase separated polymers and self-assembled monolayers are all examples of molecular self-assembly, as are the folding of polypeptide chains into proteins and the folding of nucleic acids into their functional forms. Even the association of a ligand with a receptor is a form of self-assembly; in fact as observed by Whitesides et al. [2] the semantic boundaries between self assembly, molecular recognition, complexation and other processes that form more ordered from less ordered assemblies of molecules expand or contract at the whim of those using them.

In molecular self-assemblies the structure of the molecules determines the final structure of the assembly and the interactions between the molecules have usually non-covalent nature. Molecules can be designed and synthesized

for their ability to interact specifically with other molecules or to form higher aggregates. The branch of chemistry studying molecular self-assemblies was named *supramolecular chemistry* or *chemistry beyond the molecule* by the Nobel laureate J.M. Lehn in 1978 [3]. The goal of supramolecular chemistry is to gain progressive control over the complex spatial (structural) and temporal (dynamic) features of matter through self-organization, self-directing and self-steering [4].

The success of self-assembly in a molecular system is determined by several characteristics of the system. The molecules or molecular segments may be the same or different and the interactions between them lead from some less ordered state (a solution, disordered aggregate or random coil) to a final state (a crystal or folded macromolecule) that is more ordered. Complementarity in molecular shapes among the self assembly is crucial, as well as the control over the interactions. In fact self-assembly occurs when molecules interact with one another through a balance of attractive and repulsive interactions. It can be driven by a number of forces including hydrogen and metal-ligand bonding, electrostatics, charge transfer, van der Waals attractions, hydrophobic interactions and π stacking. These weak interactions in biology are responsible for the transduction of signals, the selective transport of ions or molecules across membranes, enzymatic reactions or the formation of layered aggregates [5]. Moreover for self assembly to generate ordered structures the association either must be reversible or must allow the components to adjust their positions within an aggregate once it has formed. The bonding energy between the components, therefore, must be comparable to the one of the forces tending to disrupt them. For molecules the bonding energy has to be comparable with the thermal vibrations. The self-assembly of molecules normally is carried out in solution or at an interface to allow the required motion of the components. The interaction of these components with their environment can strongly influence the course of the process. Finally for self assembly to occur the molecules must be mobile. Thermal motion provides the major part of the motion required to bring the molecules into contact.

Self-organization is a powerful tool for nanotechnology. It is possible to fabricate functional supramolecular entities in the form of discrete species or extended assemblies in one dimension (polymolecular chains and fibers), two dimensions (layers and membranes) and three dimensions (solids). Functional devices performing energy, electron or ion exchange or transfer processes are the core of molecular and supramolecular photonics, electronics and ionics. By means of self-fabrication it will be possible to control the assembly of ordered fully integrated and connected operational system bypassing the implementation of time and energy consuming fabrication and manipulation

procedures. Molecular self-assembly in fact has a central role in molecular electronics [6, 7]. A long term goal of molecular electronics is to rent nature's methods in order to build complex circuits or other electronically active units by molecular self-assembly from solution, which means complex organization and collective operation rather than small size and individual design. Self-organization offers the full range of self processes that determine the internal built up, the functional integration and the operation (such as self selecting and self wiring) as well as its external connection to the environment (self connection for addressing and sensing). The most complex object we know, the brain, is built up by self-organization and is self-wired and self-integrated as well as self-connected to our senses. Because the self-assembled components are in a minimum energy configuration and often align with atomic precision, self assembled devices should be more robust than devices made by traditional approaches. They can be biocompatible and chemically responsive and they use much less power because the transfer of only one or a few electrons is often enough to cause the desired effect. For example, Makasymovych et al. [8] have shown that by injecting low energy electrons with the tip of a scanning tunneling microscope into individual molecules of self assembled structures of dimethyldisulfide on Au(100) it is possible to originate a propagating chemical reaction in the entire molecular assembly. Self-assembled devices can be designed to work massively in parallel and can be much less expensive to produce. Finally self-assembled structures can bridge between the length scales accessible by covalent synthesis (up to a few nm) and by top-down patterning (down to tens of nm) [6].

When considering molecular self-assembly on surfaces it is clear that the bonding of the adsorbates to the surface plays a role of comparable importance with that of non covalent bonds typical of supramolecular complexes, that moreover needs to be balanced with respect to the energy barriers for translational and rotational motion of the adsorbate species [9, 10]. Molecules can be tailored with specific functionalities, which play a central role in the self-assembly process. The bonding of the adsorbates in self-assembled monolayers is in fact driven by the specific affinity of their functional groups to the substrate. These functional groups determine also the geometry of the final assembly by controlling the intermolecular interactions and also the electronic properties of the final structure.

The aim of this thesis is to study the fundamental role of molecular functionalities in self-assembly and charge transfer in two specific systems, that can be useful in future for the development of a molecular electronic device.

After a short description of the experimental techniques and experimental apparatus employed (chapter 2), in chapter 3 the study of the self-assembly of L-methionine molecules on metal surfaces will be presented. The interest

on these molecular assemblies resides in the fact that it was shown that L-methionine molecules on Ag(111) assemble forming 1D-nanogratings of tunable periodicity in the nanometer range [11]. These structures can be used as templates for building future devices. In fact self-assembly on surfaces can be used directly to build up electronic devices or can be used as a tool to build up templates for growing other structures. Templating is widely used in biology to limit the presence of defects in the self-assembled structures. The involvement of templates ensures for example the correct folding of proteins in competition with other possible processes (e.g. intermolecular aggregation and precipitation), as demonstrated in [12]. Geometrical templating also has proven valuable in non biological assembly [13, 14, 15]. Templating offers also the possibility of generating asymmetries in self-assembeld structures. The simplest form of self-assembly, the ordered aggregation of identical components, is the one most commonly studied; this type of process, for molecular components, leads to the formation of molecular crystals or discrete, structurally defined aggregates, usually with high symmetries. A requirement for self assembly in order to have broad applications (especially in microelectronics and photonics) is to be able to generate asymmetrical units: analogous of proteins rather than analogous of crystals. It seems that templating (that is providing constraints whether physical boundaries or a sequence in a chain) may be an important way to bring order and asymmetric structures to self-assembled aggregates [2]. I have studied the self-assembly of L-methionine molecules on different metal surfaces: Ag(111), Au(111), Cu(111) and Au(110). L-methionine is an aminoacid with three functional groups that can interact with the substrate or with other molecules: the amino ($-NH_2$), the carboxyl ($-COOH$) and the thioether ($-S-$). The aim was to characterize the interactions that lead to the formation of the ordered assemblies by changing the surface nature and geometry, exploring therefore the variations in molecule/substrate interactions that are driven by the functional groups. The results will be presented in chapter 3: a large number of self-assembled geometries can be produced depending on the specific substrate choice.

As already suggested, L-methionine assemblies on appropriate surfaces can be good templates for building up molecular electronic devices. It is important at this point to find the molecule that will be a good candidate to work as active element in the electronic device. The dream is to have a device made of an array of single molecule devices, which means an array of single molecules immobilized between two metal electrodes. Therefore in the last 10 years there was a great interest in the study of single-molecule transport properties and more in general in the study of the interaction between quantum systems, like molecules, and mesoscopic systems, that are metal electrodes.

Aminoacids are themselves good candidates to be used as conducting elements in electronic devices, but they are quite complex molecules since they contain several functional groups that can interact with the electrodes and be responsible of charge transfer. The aim of this thesis is to understand the role of a specific functional group (the amino $-NH_2$) in molecular conduction, therefore I have studied simpler molecules with respect to aminoacids containing only amino functional groups. In particular it was recently shown that amino-terminated molecules are good candidates for building single molecule devices on Au electrodes with reproducible properties [16]. In literature few is known on the assembly on Au surfaces of molecules with amino terminations, but it is clear that the knowledge on how the single molecules assemble across the junctions, whether they are bound covalently or non covalently to the electrodes and what electrode material is used plays a crucial role in either masking or revealing unique molecular electronic properties. Molecular electronics will mature into a powerful technology only if its development is based on the understanding of the molecule/electrode interface as well as methods for fabricating reliable devices and ensuring their robustness are developed. In chapter 4 I will concentrate on the first point, that is the study of the molecule/electrode interface, with a particular interest on the role of the amino functional groups in assembly and charge transfer on Au(110) and Au(111) surfaces. The results presented show that the weak bonding of the molecules takes place also via the amino group and that this functional group is responsible of charge transfer to the metallic substrate.

Bibliography

[1] Schreiber F., Progress in Surface Scienc 65 (5-8) (2000) 151

[2] Whitesides G.M., Boncheva M., PNAS, 99(8) (2002) 4769

[3] J.-M. Lehn, Angew. Chem. Int. Ed. 27 (1988) 89

[4] J.M. Lehn, Science, 295 (2002) 2400

[5] Reinhoudt D.N., Crego-Calama M., Science 295 (2002) 2403

[6] Flood A.H., Fraser Stoddart J., Steuerman D.W., Heath J.R., Science, 306 (2004) 2055

[7] Smith W.F. Nature 2 (2007) 77

[8] Maksymovych P., Sorescu D.C., Jordan K.D., Yates Jr. J.T., Science, 322 (2008) 1644

[9] Stepanow S., Lin N., Barth J.V. J Phys cond matter 20 (2008) 184002

[10] Barth J.V., Costantini G., Kern K., Nature, 437 (2005) 671

[11] Schiffrin A., Riemann A., Auwaerter W., Pennec Y., Weber-Bargioni A., Cvetko D., Cossaro A., Morgante A., Barth J.V., PNAS, 104 (13), 5279 (2007)

[12] Frydman J., Annu Rev Biochem 70 (2001) 603

[13] Choi I.S., Weck M., Xu B., Jeon N.L., Whitesides G.M., Langmuir 16 (2000) 2997

[14] Huck W.T.S., Tien J., Whitesides G.M., JACS, 120 (1998) 8267

[15] Kim E., Whitesides G.M., Chem Mater 7 (1995) 1257

[16] Venkataraman L., Klare J. E., Nuckolls C., Hybertsen M. S., Steigerwald M. L., Nature 442(7105) (2006), 904

Chapter 2

Experimental techniques and apparatus.

In the first part of this chapter I will briefly summarize the fundamentals of the experimental techniques employed in the experiments presented in chapter 3 and 4, that are Helium Atom Scattering (HAS), Photoemission Spectroscopy (XPS and UPS), Near Edge X-Ray Absorption Fine Structure (NEXAFS) and Resonant Photoemission Spectroscopy (RPES). I will not describe all the details of each technique, instead I will report only the information that will be useful in the analysis of the experimental results. In the second part of the present chapter I will briefly describe the experimental apparatus employed.

2.1 Experimental Techniques.

2.1.1 Helium Atom Scattering (HAS).

Helium atom scattering (HAS) is a surface analysis technique that measures the diffraction of a monochromatic beam of helium atoms incident on the surface of a sample which presents long range order. In other words HAS measures the *surface dynamic structure factor* $S(\Delta\mathbf{k}, \omega)$, which contains information on the static and dynamic properties of the surface. A detailed description of this technique can be found in [1] and ref. therein .
Low energy helium atoms (10-300 meV) have several attributes that make them uniquely suitable to the study of surfaces and surface vibrations.
• He atoms are strictly surface sensitive. Particularly for a lightweight atom such as helium, there is absolutely no penetration into the bulk. Any information carried away by the scattered atom, whether due to the structure or

to the dynamics, will relate only to the outermost layer of the crystal.
• Helium atom beams are a chemically, electrically, magnetically and mechanically inert probe. It is therefore possible to study the surface structure or dynamics of virtually any material, to do so for reactive or metastable surfaces or in the presence of electromagnetic fields and even to make measurements during UHV processing without altering the process.
• He atoms have no rotational or vibrational degrees of freedom and no accessible electronic transitions at thermal collision energies. Only the translatory motion of the incident and scattered beam need to be analyzed to extract information on energy and momentum exchange.
• For inelastic scattering studies He atoms are particularly well-matched in momentum and energy to surface phonons. This ensures that the resultant changes in scattered beam momentum are large and easily resolved. Yet the inelastic scattering cross sections are sufficiently low that, over a reasonable range of source temperatures and scattered angles, only single surface phonons are excited or deexcited thus allowing an unambiguous mapping of inelastic energy loss/gain onto vibrational frequency and wavelength.
• He atoms are extremely sensitive to adsorbates and it is possible do determine minute amounts of surface impurities (down to 10^{-4} ML) with interesting consequences with respect to technologically important investigations of surface diffusion as well as two dimensional condensation and growth phenomena.

In the experiments presented in the following chapters we are interested only in determining whether the molecules are adsorbed on the surface and whether their assemblies present long range order. This can be done by monitoring the Helium atoms elastically scattered from the surface.

In principle in a diffraction experiment from an infinite periodic array of atoms, the diffraction pattern has a delta-like shape which reflects the symmetry of the real space surface corrugation. The exact profile of the He-surface interaction potential manifests in the scattering form factor and superimposes a large-k modulation of the diffracted intensities. Surface vibrations at finite temperatures influence the time correlation of the surface scatterers and damp the diffraction intensities (the Debye-Waller effect). When considering real crystal surfaces, they do not possess infinite long range order but always contain a finite density of defects. These may occur as thermal excitations (steps and domain walls) or due to strain relief (dislocations) or may simply exist from the time of crystal formation. The reduced long range order due to the presence of defects reflects in a diminished intensity of the diffraction peaks. The same behavior manifests also due to the presence of adsorbates on the surface, which act as defects. By monitoring the modifications in the long range order of the clean surface it is possible to infer

whether molecules are adsorbed on the surface. Moreover when disordered structures are spatially correlated, additional diffraction peaks may appear.

The scattering problem

As we have already mentioned, the angular positions of the diffraction peaks allow the determination of the dimensions of the unit cell of the periodic structure on the surface as well as its orientation relative to the incoming beam.
This can be easily explained within the kinematic theory. If we consider a beam of particles of mass m and energy E_i impinging on a surface at an angle θ_i as measured from the surface normal (fig. 2.1), then the particle wavelength λ is related to the beam energy according to the De Broglie relation:

$$\lambda = \frac{h}{\sqrt{2mE_i}}$$

and the incoming wavevector is $k_i = 2\frac{\pi}{\lambda}$.

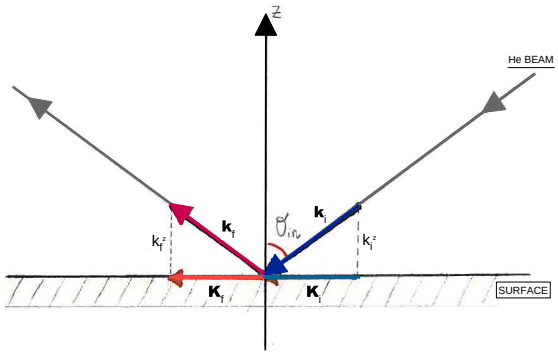

Figure 2.1: Sketch of the decomposition of the momentum vector in the scattering of He atoms with a surface.

It is useful to separate the wavevector $\mathbf{k}$ into a component $\mathbf{K}$ parallel to the surface and a component k_z perpendicular to the surface:

$$\mathbf{k}_i = (\mathbf{K}_i, k_i^z)$$

$$\mathbf{k}_f = (\mathbf{K}_f, k_f^z)$$

The well known Bragg condition for diffraction from a two dimensional periodic array relates the wavevectors $\mathbf{k}_i$ and $\mathbf{k}_f$ by

$$\mathbf{K}_i + \mathbf{G} = \mathbf{K}_f$$

where **G** denotes a reciprocal lattice vector. During diffraction the energy remains unchanged so that $k_i = k_f$, and the number of reciprocal lattice vectors for which diffraction can occur is restricted to the finite set F that satisfies $k_f^{z2} = k_i^{z2} - \mid \mathbf{K} + \mathbf{F} \mid^2 > 0$

In the scattering geometry of our setup [2, 3] the positions of the source of He atoms and that of the detector are fixed. The scattering angle between them is $\theta_{tot} = \theta_{in} + \theta_{out} = 110°$. The surface can rotate in the scattering plane. If R1 is the angle of rotation of the surface, as indicated in figure 2.2, then:

$$\mathbf{K}_i = k \sin\left(\frac{\theta_{tot}}{2} + R1\right)$$

$$\mathbf{K}_f = k \sin\left(\frac{\theta_{tot}}{2} - R1\right)$$

so the size of the parallel momentum transfer is:

$$\Delta K = K_f - K_i = 2k \sin\left(R1\right) \cos\left(\frac{\theta_{tot}}{2}\right)$$

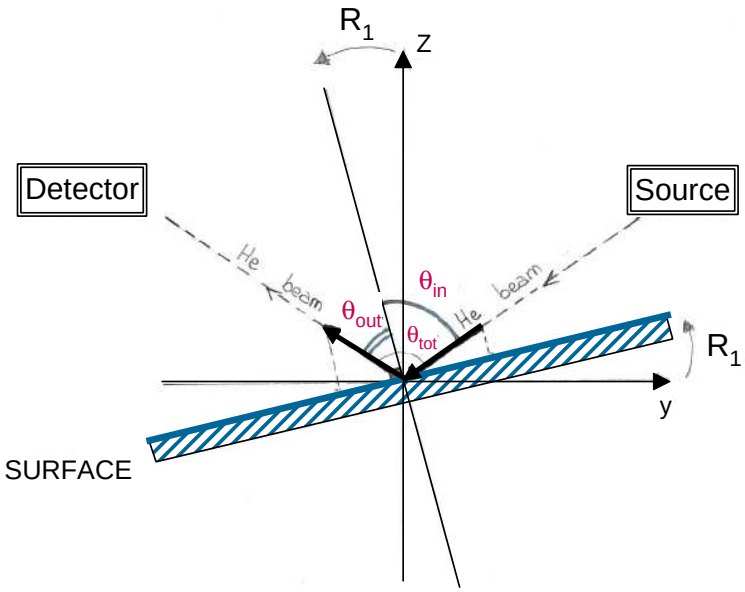

Figure 2.2: Experimental setup of a fixed He scattering geometry.

The kinematic theory allows the determination of the positions in the k-space of the diffracted peaks, but if we want to consider the behavior of the intensities of the peaks, we should consider the problem of the scattering of helium atoms from a periodic surface from a quantum-mechanical point of view.

We can start by considering the one-particle Schröedinger equation for the incident He atom, with $V(\mathbf{r})$ the interaction potential (we will discuss its form later):

$$(\frac{\hbar^2}{2M}\nabla^2 + (V(\mathbf{r}) - E))\psi(\mathbf{r}) = 0$$

Since the surface presents lateral periodicity, $V(\mathbf{r})$ can be factorized as:

$$V(\mathbf{r}) = \sum_{\mathbf{G}} V_{\mathbf{G}}(z)e^{i\mathbf{GR}}$$

and the solutions of the Schröedinger equation have then the character of a lateral Bloch-wave:

$$\psi_{\mathbf{K}}(\mathbf{r}) = \sum_{\mathbf{G}} e^{i|\mathbf{K}+\mathbf{G}|\mathbf{R}}\psi_{\mathbf{G}}(z)$$

If we substitute this solution into the Schröedinger equation, we obtain the following coupled equations (one for each $\mathbf{G}$)

$$-\frac{d^2\psi_{\mathbf{G}}(z)}{dz^2} + \sum_{\mathbf{G}'} V_{(\mathbf{G}'-\mathbf{G})}\psi_{\mathbf{G}'}(z) = k^2_{\mathbf{Gz}}\psi_{\mathbf{G}}(z)$$

where

$$V_{(\mathbf{G}'-\mathbf{G})} = \int V(\mathbf{r})e^{-i(\mathbf{G}-\mathbf{G}')\mathbf{R}}d\mathbf{R}$$

and

$$k^2_{(\mathbf{G}_z)} = \frac{2mE}{h^2} - (\mathbf{K}+\mathbf{G})^2$$

.

This is a set of differential equations which should be solved with appropriate boundary conditions.
In the asymptotic regime we can impose that the particle does not penetrate into the crystal and that far away from the surface its wave function has a plane wave form. Therefore:

$$\begin{cases} \psi_{\mathbf{G}}(z) \to 0; z \to -\infty \\ \psi_0(z) \to \exp^{-ik_z z} + c_0 \exp^{ik_z z}; \psi_{\mathbf{G}}(z) \to c_{\mathbf{G}} \exp^{ik\mathbf{G}\mathbf{z}^z}; z \to -\infty \end{cases}$$

In the previous equations the outgoing waves represent specular ($G = 0$) and diffraction ($G \neq 0$) scattering.
The probability of having a scattering event associated with a parallel momentum exchange equal to $\mathbf{G}$ can then be written as $P_G = \mid c_G \mid^2$ and is directly proportional to the scattering intensity of various diffracted peaks. However in order to solve the quantum-mechanical problem, we need to know the interaction potential $V(\mathbf{r})$. In the next section I will discuss the most commonly used approximations for $V(\mathbf{r})$.

The He-surface potential.

In this section the discussion on $V(\mathbf{r})$ will be limited to the case of scattering with atoms of thermal energies, i.e. 10 to 100 meV. In general it is plausible to make the assumption that the He-surface interaction consists of a short range repulsion V_{rep} and a long range attraction V_{att}:

$$V = V_{att} + V_{rep}$$

The repulsive part arises from the overlap of the atom and surface electronic density, whereas the attractive part has its origin in the van der Waals dispersion forces. At very long and very short distances from the top-most nuclear plane both V_{att} and V_{rep} have a well defined and physically plausible spatial form, but this is by no means the case in the intermediate region (2-20 Ångstrom) where both contributions to the potential are comparable. This is exactly the region explored by thermal He atoms (4-5 Ångstrom from the top-most nuclei plane) which makes the analysis of He scattering intensity related to the knowledge of the interaction.

If we consider a perfect infinite surface, the simplest approximation for $V(\mathbf{r})$ consist in replacing V_{rep} by a corrugated hard wall and entirely neglect the attractive forces:

$$\begin{cases} V(\mathbf{R}) = \infty, z \leq \chi(\mathbf{R}) \\ V(\mathbf{R}) = 0, z > \chi(\mathbf{R}) \end{cases}$$

with $\mathbf{r} = (\mathbf{R}, z)$.

The locus of the classical turning point for He surface scattering is then described by the corrugation function $\chi(\mathbf{R})$. He scattering from a rigidly modulated surface unit cell may be treated semi-classically, i.e. assuming that all parts of the unit cell surface contribute equally to the scattered amplitude, which results in the modulation of the diffracted intensities. This can be adopted for very smooth surfaces. To the lowest Fourier order the surface corrugation may be written as:

$$\chi(\mathbf{R}) = \chi_0[\cos(\frac{2\pi x}{a}) + \cos(\frac{2\pi y}{b})]$$

where a and b are the surface lattice vectors and $4\chi_0$ is the peak to valley corrugation of the surface. The unit cell scattering amplitude (i.e. Form factor) is obtained by integrating partial waves over this surface:

$$A_G = -\int \frac{d^2\mathbf{R}}{ab} \exp(-i[\Delta k_z \chi(\mathbf{R}) + \mathbf{GR}] \propto J_{|m|}(\chi_0 \delta k_z) J_{|n|}(\chi_0 \delta k_z)$$

where a and b are the surface unit vectors and J_m is the ordinary Bessel function of order m. Inclusion of a laterally averaged attractive interaction in the He-surface potential describes a much richer system because of the additional states formed in the He-surface potential well. This opens new resonant scattering channels that can explain the dips and peaks in the diffraction peak intensities (as a function of scattering conditions).

If we go to rough surfaces the simple approximation presented above does not hold anymore and it is necessary a more detailed representation for the repulsive and the attractive interaction respectively.

First of all we can consider the repulsive part of the interaction potential V_{rep}. As a He atom approaches the solid surface it experiences a strong short-range repulsion since the overlap of the He electronic distribution and that of the surface forces a rearrangement of the electronic states in order to ensure their orthogonality at all stages of the scattering event (Born-Oppenheimer approximation). Zaremba and Kohn [4] and later Harrish and Liebsch [5] have studied this problem within the HF approximation where they considered a He atom well outside the surface and treated it as a perturbation on the surface electrons. By carrying out the calculations to first order in the He-surface overlap integral they determined the repulsive interaction as:

$$V_{rep}(\mathbf{r}) = \int_{-\infty}^{E_f} dE n(E, \mathbf{r}) g(E)$$

where $n(E, r)$ is the local density of states for the substrate as modified by the He atom at position $\mathbf{r}$ and $g(E)$ is an energy dependent function accounting for the overlap between the He atom electrons and those of the substrate. Since $g(E')$ is almost constant in the region explored by thermal He atoms.

$$V_{rep}(\mathbf{r}) = g(E')n(\mathbf{r}) = \alpha n(\mathbf{r})$$

This result was also confirmed by DFT calculations [6].

Another common way of determining the He-surface repulsive interaction arises from the fact that many atom-atom pair potentials are known quite

accurately and the simplest extension to the atom-surface case is obtained by a geometrical superposition of pair potentials. In the case of He-insulator one can start directly from pairwise repulsive interactions between the He atom and surface constituents and try to build up the He-surface potential by summing the pairwise terms over the geometrical positions of the surface constituents. In this case, $n(r)$ is, by construction, the pairwise sum of the densities of the constituents and the previous equation turns out to be valid, again within the accuracy of the calculation. Because of the exponential decay of $n(r)$ and large values of α the repulsion close to the surface is very steep. The equipotential lines which are of interest for thermal He atoms correspond to very low electronic densities ($10^{-3} el/$ Å^3), reached about 4 Å from the top most nuclear plane. At such large distances the electron density may be fairly well represented by superposing the tails of the electronic densities of the individual atoms. On the other hand, for metals this summation is not an obvious procedure: the electron delocalization in the metallic bond may result in a different spatial distribution of the electron cloud with respect to the electron density obtained by a simple pairwise summation. The main trouble is that this approximation works well for the laterally averaged atom-surface potential V_0, while it overestimates the effective corrugation of the surface. As a practical matter the laterally averaged He surface potential is generally well approximated by

$$V_{rep}(z) = U_{rep} \exp^{-\beta z}$$

which is consistent with a pairwise summation of the Yukawa potentials

$$U_k \frac{\exp(-\beta r)}{r}$$

over a monoatomic top layer. It is even more customary to adopt a repulsive pair potential widely used in atomic physics of the Born Mayer form

$$U_k \exp(-\beta r)$$

which after summation yields

$$V_{rep}(z) \propto (1 + \beta z) \exp(-\beta z).$$

If we consider now the attractive part of $V(\mathbf{r})$, then the asymptotic interaction of a distant atom with a surface is usually described by a long-range polarization or dispersive van der Waals force. At large values of z (distance from the solid) this interaction is attractive and may be written as

$$V_{att} = -\frac{C_3}{z^3}$$

with C_3 given by the Lifshitz formula:

$$C_3 = \frac{\hbar}{4\pi}\int_0^\infty d\omega \frac{\epsilon(i\omega)-1}{\epsilon(i\omega)+1}\alpha_{He}(i\omega)$$

where ϵ is the dielectric function of the surface and α is the He atom polarizability. For a crystal consisting of localized electronic units (atoms, molecules or ions) having the polarizability α, the crudest way to compute V_{att} is to sum pairwise interactions (induced-dipole/induced-dipole) $-\frac{c_6}{|\mathbf{r}-\mathbf{r}_l|^6}$ where

$$c_6 = 3\frac{\hbar}{\pi}\int_0^\infty \alpha(i\omega)\alpha_{He}(i\omega)d\omega.$$

The sum over a monoatomic plane, spaced by d to the next crystal plane yields:

$$V_{att}(z) = -\frac{C_3}{(z-\frac{d}{2})^3}$$

Corrections to this equation arising from the higher order multipolar terms may be considered by generalizing the Lifshitz work, if we assume that the He charge density does not overlap with the surface charge density and that the response to the electrical fluctuations is linear.

For the analysis of the data presented in chapter 3 and 4 it is not needed a detailed description of the He interaction potential. It is just important to note that even in the simplest hard wall model the scattering intensities of the peaks depend on the surface corrugation. Therefore changes in the surface corrugation result in different intensities of the diffraction peaks and such changes can be induced by the presence of adsorbates. The long range order of the adsorbates, if present, will then be determined by means of the kinematic theory.

2.1.2 Photoemission spectroscopy.

Photoemission spectroscopy is a widely used technique for studying the properties of atoms, molecules, solids and surfaces [7]. It is based on the photoelectric effect discovered by Hertz in 1887 and explained by Einstein in 1900: in a metal sample connected with an electric circuit and illuminated with visible or ultraviolet light, the adsorption of electromagnetic radiation induces electron emission.

The photoemission process is sketched in figure 2.3. Following absorption of a photon $h\nu$ an electron initially bounded to an atom with binding energy E_b will be ejected with a kinetic energy E_{kin}. According to energy

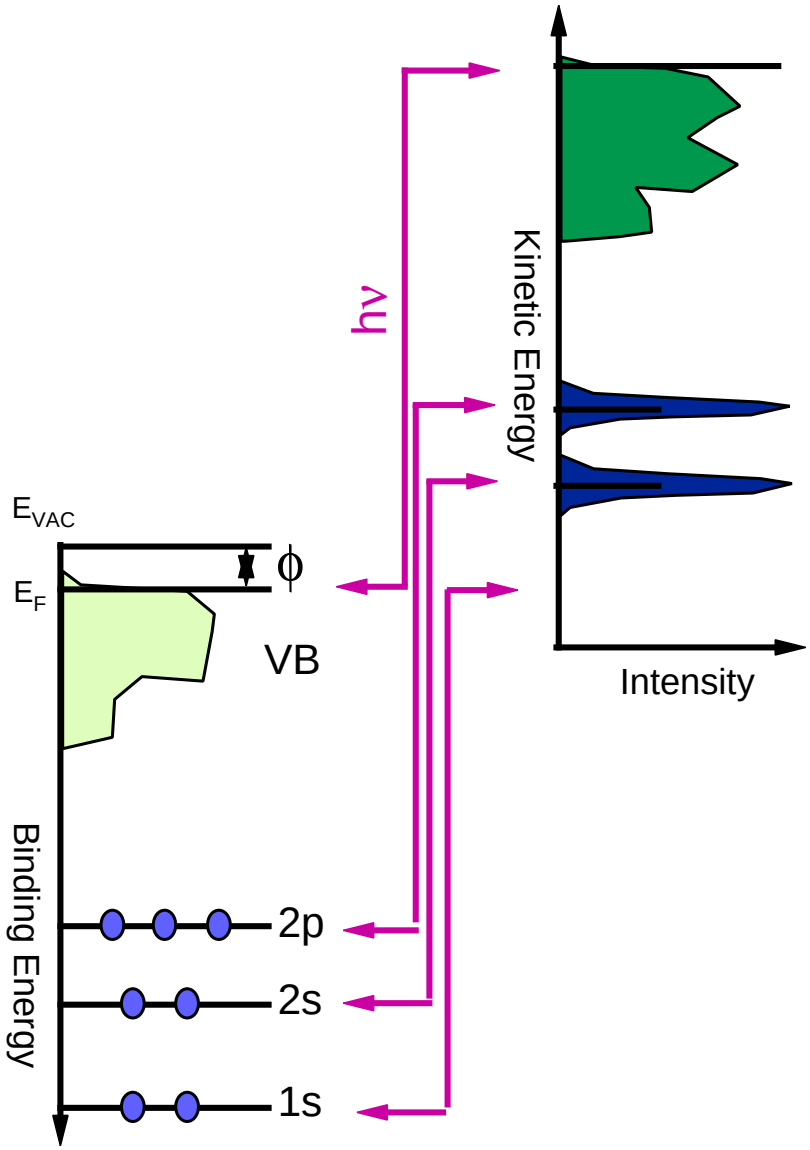

Figure 2.3: Schematic energy diagram of the photoemission process. With the selected photon energy (pink lines) the 1s level is not visible in the photoemission spectrum.

conservation, the measured kinetic energy of the outgoing electron is given by:

$$E_{kin} = h\nu - E_b - \phi$$

where ϕ is the sample work function (see fig. 2.3). By measuring the kinetic energy of the emitted electrons it is possible to determine their binding energy. The zero point for binding energy is the Fermi level E_F and it is used as a reference for measurements.

Traditionally, the photoemission technique is subdivided into UPS (Ultraviolet Photoemission Spectroscopy) and XPS (X-ray Photoemission Spectroscopy) depending on the source of exciting radiation. UPS experiments are performed with photons in the low energy range (5-45 eV) in order to excite valence electrons, whereas in XPS experiments photons are characterized by higher energy (100-2000 eV), thereby allowing the study of inner core electrons.

One of the most useful properties of the XPS technique is its surface sensitivity. A photon in the 100-1000 eV energy range penetrates for some hundred nanometers into the sample and so most electrons created are from the bulk and not from the surface. However an electron emitted from deeper layers will undergo inelastic collisions that reduce its kinetic energy and change its direction of travel. It will be emitted at very low energy or it will not be emitted and the lost energy contributes to the creation of bulk or surface plasmons and the formation of electron-hole pairs which contribute into the background. Probabilities of electron interaction with matter, however, far exceed those of the photons, so while the path length of the photons is of the order of micrometers that of the electrons is of the order of tens of Ångstroms for $E_k \approx 100 - 1000$ eV.

The photoelectron spectrum reproduces the electronic structure, that means that all the occupied electronic states of an element up to the binding energy equal to the photon energy minus the material work function are measured. This way the core levels as well as the valence band are mapped. Since each element has a unique set of binding energies, XPS can be used to identify and determine the concentration of the elements in the surface. In fact for a monolayer of a given element the photelectron intensity is usually proportional to the number of ionized atoms and hence to its concentration. It is possible to obtain the amount of adsorbate on the surface by calculating the area within the peak and converting this quantity to Monolayer (ML), if the coverage of a reference is known. Moreover the same core level can exhibit different binding energies depending on the chemical state and the environment surrounding the emitting atom. It is therefore possible to distinguish inequivalent atoms of the same chemical species or to identify

adsorption sites of atoms (and molecules) on the surface.

It is important to note that the outgoing photoelectron can undergo diffraction effects. This means that the core level intensity originating from atoms in different geometrical environments may not always directly be comparable. A photoelectron with kinetic energy of around 100 eV exhibits a wavelength of about 1 Å and is thus comparable with the characteristic lattice distances in solids or bond lenghts in molecules. This causes interference effects between the directly emitted electron and that scattered from atoms nearby. In this way the peak intensity changes as a function of the detection angle (due to the different interference directions) as well as with the photon energy (since this implies a kinetic energy change and thus wave length variation).

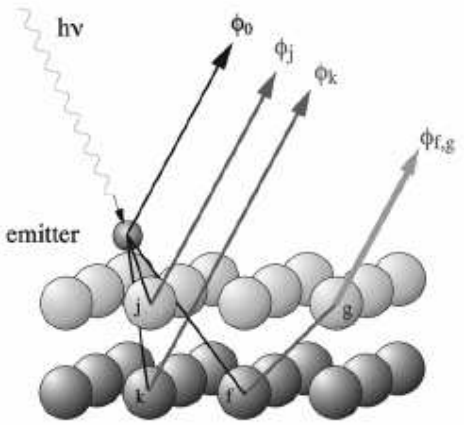

Figure 2.4: Schematic diagram of the photoelectron diffraction effect. The primary wave ϕ_0 is generated in the photoemission process relative an atom adsorbed on top on the crystal surface. The secondary waves ϕ_j and ϕ_k are created by atoms j and k of the first and second layers, respectively, while $\phi_{f,g}$ is originated by a double scattering effect.

This effect is represented schematically in fig. 2.4 in which a photon with energy $h\nu$ excites a core electron belonging to an atom adsorbed on top on a crystal surface. The outgoing wave ϕ_0 can either directly reach the detector or be scattered by atoms around the emitter. This generates waves ϕ_j, ϕ_k and $\phi_{f,g}$ that interfere with the primary wave and yield a characteristic diffraction pattern for each emitter. Therefore, in certain directions and with specific kinetic energies there is constructive interference, which

enhances photoemission intensity. However, in other directions there is reduced intensity, resulting in intensity modulation as a function of detection angle and photon energy. This phenomenon is usually exploited in order to determine the geometry of the excited atom, i.e. bond lengths and bond angles: unlike the Low Energy Electron Diffraction (LEED) technique which requires a long range order, photoelectron diffraction is a local scattering phenomenon which depends only on the configuration of the atoms in the vicinity of the emitter mainly due to the mean free path of the electrons.

2.1.3 Near Edge X-Ray Absorption Fine Structure (NEXAFS).

In this section I will briefly report some notes about NEXAFS technique; for more details see ref. [8].

Near Edge X-Ray Absorption Fine Structure (NEXAFS) is a synchrotron based technique in which the X-ray absorption of a material is measured across the excitation edge of a certain atomic shell. In a NEXAFS measurement the photon energy is scanned in an energy range of about 50 eV starting below a core level binding energy. For certain photon energies (as depicted in figure 2.5) an electron from the inner shell can be excited to one of the unoccupied states. The X-ray absorption cross section $\sigma(hv)$ is then defined as the number of electrons excited per unit time divided by the number of incident photons per unit time per unit area. In particular, when considering a thin film of molecules on a surface, in the limit of small adsorbate concentrations, the number of photons adsorbed in the molecular layer is

$$N_{abs} = I_0 A_0 (1 - \exp^{-\sigma(h\nu)\rho}) \approx I_0 A_0 \sigma(h\nu)\rho$$

with A_0 the area exposed to the beam, I_0 the incident photon flux density, ρ the atomic area density.

The core holes created by photon absorption are then annihilated via the emission of Auger electrons (non radiative decay) or fluorescent photons (radiative decay). Both decay channels are a direct measure of the probability of the existence of a core hole created by X-ray absorption and are used in NEXAFS measurements. Auger decay (in the right graph of fig. 2.5) dominates for the K-shell excitation of low Z atoms and for the L-shell excitation of all atoms with $Z < 90$.

If we consider the transition from the initial state $|i>$ (that is the core level) to the final state $|f>$ (that is an empty state) caused by an electromagnetic wave (photon) with electric field vector $\mathbf{E} = E\mathbf{e}$, then the X-ray absorption cross section can be calculated by using Fermi's Golden Rule:

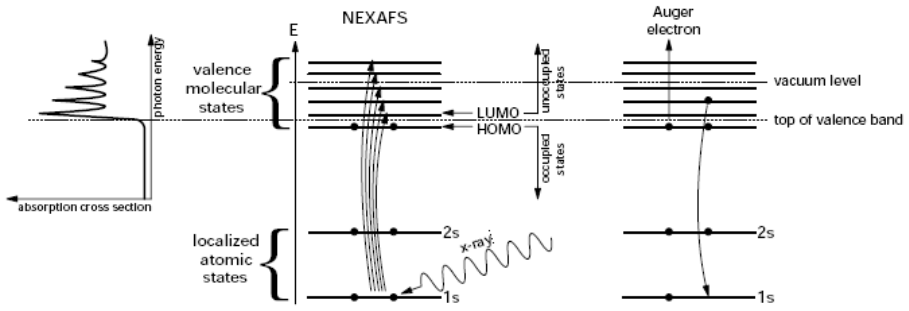

Figure 2.5: The mechanism of NEXAFS (middle), a corresponding X-ray absorption spectrum (left) and Auger emission (right).

$$\sigma = \frac{4\pi^2\hbar^2}{m^2}\frac{e^2}{\hbar c}\frac{1}{\hbar\omega}| < f|\mathbf{e} \bullet \mathbf{p}|i > |^2\rho_f(E)$$

with $\mathbf{e}$ a unit vector in the direction of the electric field, $\mathbf{p}$ the linear momentum operator of the electron and $\rho_f(E)$ the energy density of the final states. Therefore we can conclude that for the molecular film the adsorbed photons are:

$$N_{abs} \propto | < f|\mathbf{e} \bullet \mathbf{p}|i > |^2\rho_f(E).$$

It is clear from the previous equation that for a given initial state $|i >$ not all the final states $|f >$ are allowed for the excited electrons. This point will be better discussed later in this section.

How is performed the NEXAFS measurement? -It is interesting to consider how the measurements are performed in order to better understand the information that can be obtained and relationship with Resonant Photoemission Spectroscopy which will be presented in the next section. We will consider only measurements employing Auger electrons (non radiative decay).

In figure 2.6 is reported a schematic photoemission spectrum taken from ref.[8]. For simplicity it is assumed that the sample consists of two kinds of atoms: adsorbate atoms which have a core level A and a valence level which overlaps with the valence band (VB) of the substrate, and substrate atoms

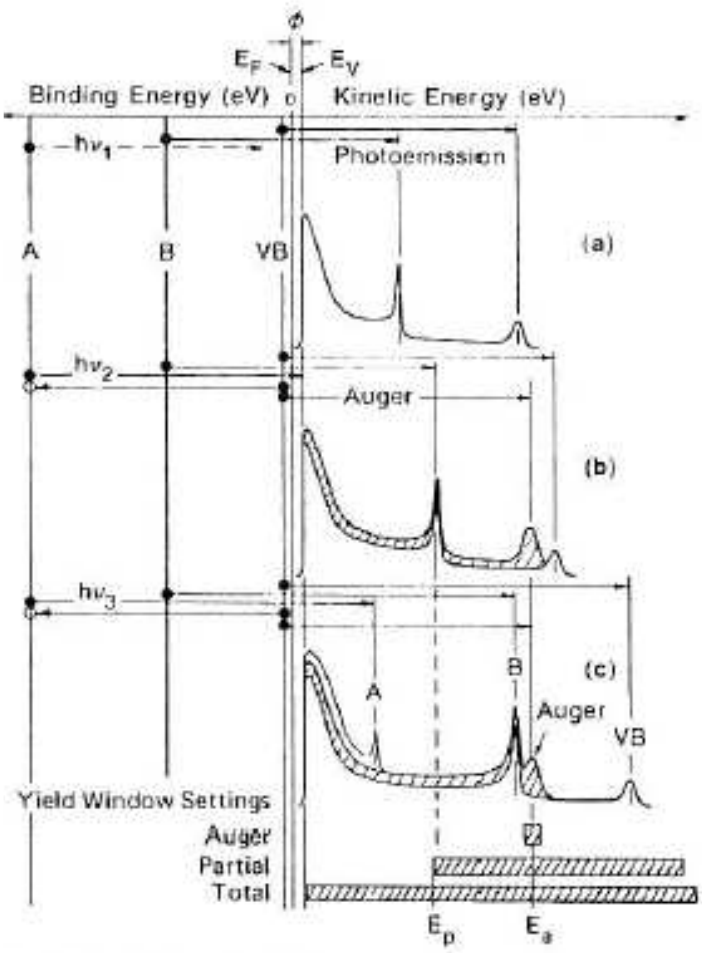

Figure 2.6: Energy level diagram and schematic photoemission spectra at different photon energies for a sample containing atoms with two core levels A and B and a valence band VB. The energy zero is chosen at the Fermi Level E_F, which lies below the vacuum level E_V by the work function ϕ. (a) $h\nu_1$ below the excitation threshold of core level A, (b) $h\nu_2$ just above the absorption threshold of shell A but below its photoemission threshold, (c) $h\nu_3$ far above threshold of shell A. At each energy the various photoemission and Auger peaks and their inelastic tails are indicated. At the bottom, window settings for different electron yield detection modes are shown. In the Auger yield mode the detector window is set around the energy E_a of the Auger peak. For partial yield detection only electrons with a kinetic energy in access of E_p are detected while all electrons are collected in the total electron yield mode. Image from [8].

with a shallow core level B and the valence band also overlapping VB. The electron binding energies (E_b) are measured relative to the Fermi level (E_f) of the substrate. The Fermi level also defines the zero of the photoelectron kinetic energy and is separated from the vacuum level (E_v) by the work function (ϕ). As the photon energy is increased from below [$h\nu_1 < E_b(A)$] to just above the absorption threshold [$h\nu_2 > E_b(A)$] of shell A, the creation of the core hole results in the appearance of a characteristic Auger peak in the photoemission spectrum at kinetic energy E_a while the photoemission peaks move with the photon energy. The Auger peak is characteristic of the adsorbate atoms and originates from the decay of an adsorbate valence electron into the core hole in the shell A with transfer of the decay energy to another adsorbate valence electron. At the shown energy $h\nu_2$ the electron excited from the adsorbate shell A is not free to leave the sample because its kinetic energy is not enough to overcome the work function. As the photon energy is increased further more ($h\nu_3$) a photoemission peak corresponding to level A is observed while the Auger peak remains at fixed kinetic energy. The intensity of the Auger peak however will change with photon energy and follow the X-ray absorption cross section of shell A. It has to be noted that in this model only one Auger peak was considered for simplicity, but other Auger electrons can result from the core-hole de-excitations that involve core electrons and have lower kinetic energy.

The X-ray absorption measurement can be performed in several ways. By using an electron energy analyzer we can select a window and center it at the fixed energy E_a of the Auger peak. The recorded intensity will directly give the X-ray absorption cross-section of the shell A of the adsorbate atom (Auger Electron Yield (AEY) detection scheme). However a fraction of the Auger electrons from the adsorbate suffer an energy loss and emerge from the sample with a kinetic energy less than E_a. Because the primary Auger kinetic energy is independent of hv so is the energy distribution of the inelastic Auger electrons. Therefore the inelastic Auger intensity will follow the elastic one. This fact is utilized in the partial electron yield (PEY) detection variant, where only electrons of kinetic energy larger than a threshold energy E_p are detected. The elastic and part of the inelastic Auger intensity are collected together in the signal. By suitable choice of E_p one can avoid photoemission peaks of the substrate entering the kinetic energy window of the detector over the NEXAFS energy range. Some photoemission peaks may already fall into the window at the lowest photon energy of the NEXAFS scan, but these simply increase the overall background. The third and simplest detection scheme consists of collecting electrons of all energies from the sample and is referred as total electron yield (TEY) detection. The TEY signal is dominated by low energy electrons with kinetic energy below 20 eV,

the so-called inelastic tail. A fraction of the electrons composing the inelastic tail are inelastically scattered Auger electrons from the adsorbate and it is this fraction which is responsible for the desired NEXAFS signal.

The setup that I have used is for PEY measurements, therefore we are collecting all the electrons above a certain edge, which was set at 245 eV for all the Carbon K-edge NEXAFS measurements and 370 eV for all the Nitrogen K-edge NEXAFS measurements. PEY detection is more surface sensitive and presents a better signal to background ratio than TEY. Moreover it is less time consuming than AEY.

How can be measured the molecular orientation? If we go back to the formula for the NEXAFS intensity

$$N_{abs} \propto | < f|\mathbf{e} \bullet \mathbf{p}|i > |^2 \rho_f(E)$$

it is clear that in order to have the transition from $|i>$ to $|f>$ some symmetry conditions have to be satisfied between the initial molecular state ($|i>$) and the final molecular state ($|f>$), in particular between the spatial orientation with respect to the electric filed. Before discussing the angular dependence of K-shell resonances it is convenient to classify the molecules into general groups. The classification is based on the concept that bonds and the associated MOs (molecular orbitals) in molecules are highly directional. Such directionality even exists in chemisorbed molecules although the overall symmetry of the adsorbate complex will generally be different from that of the free molecule. The valence electron states, in particular those involved in the molecular bonding, can be described with a spatial distribution of $\pi^\star$ and $\sigma^\star$ orbitals: in $\pi^\star$ orbitals the charge distribution is orthogonal to the bond, while in $\sigma^\star$ orbitals it is along the bond. If we denote as ϵ the angle between the electric field and the direction normal to the bond in the case of $\pi^\star$ symmetry or the direction of the bond in case of $\sigma^\star$ symmetry, then for a 1s initial state the direction of maximum intensity of the NEXAFS signal is given by:

$$| < f|\mathbf{e} \bullet \mathbf{p}|i > |_p^2 \propto I_p = sin(\epsilon)^2.$$

In the coordinate system and with the angle definition given in figure 2.7:

- (x, z) = Electron orbit plane in the storage ring.
- y = Normal to the electron orbit plane in the storage ring
- n = Direction perpendicular to the sample surface
- N = Direction normal to the planar orbital plane for $\pi^\star$ states or along the bond for $\sigma^\star$ states

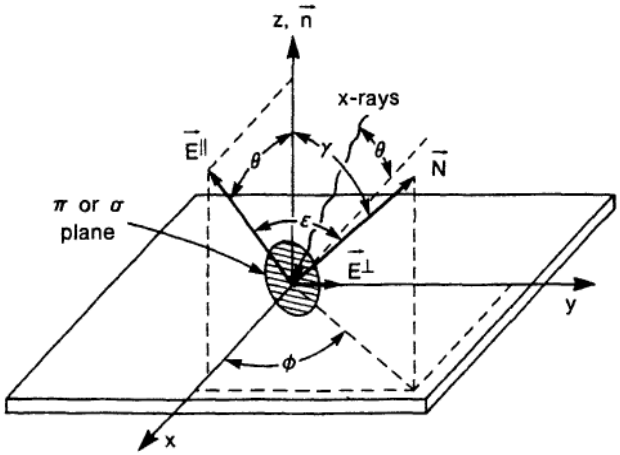

Figure 2.7: Coordinate system for a $\pi^\star$ or $\sigma^\star$ plane. The plane is characterized by the polar γ and the azimuthal ϕ orientation of its normal N. The plane is tilted from the surface by γ [8].

- $E^{\parallel}$ = Electrical field component parallel to the orbit plane: it lies in the (x,z) plane
- $E^{\perp}$ = Electrical field component perpendicular to the orbit plane: it is parallel to the y direction.
- θ = X-rays incidence angle with respect to the sample surface
- ϕ = Azimutal angle of the planar orbital with respect to the sample surface
- γ = Tilt angle of the planar orbital with respect to the surface
- ϵ = Angle between E and the normal of the plane N

we can express the angle ϵ in terms of the angles θ, ϕ and γ. Considering all the molecules forming a single domain on the surface, we have:

$$I_p = 1 - \cos\theta^2\cos\gamma^2 - \sin\theta^2\sin\gamma^2\cos\phi^2 - 2\sin\gamma\cos\gamma\sin\theta\cos\theta\cos\phi$$

The angular dependence of the resonance intensities given by the previous formula explicitly depends on the azimuthal orientation of the molecule relative to the substrate through the angle ϕ.

This azimuthal dependence in many cases is eliminated by the symmetry of the surface that induces the formation of orientational domains. Therefore by averaging with respect to the azimuthal angle according to the surface symmetry for a twofold surface symmetry we obtain:

$$I_p = 1 - \cos\theta^2\cos\gamma^2 - \sin\theta^2\sin\gamma^2\cos\phi^2.$$

For a higher surface symmetry (threefold or manifold the expression is the same) we obtain:

$$I_p = 1 - \cos\theta^2\cos\gamma^2 - \frac{1}{2}\sin\theta^2\sin\gamma^2.$$

Thus for a threefold or higher symmetry the azimuthal angle dependence vanishes and the expression are equivalent to those for cylindrical symmetry about the surface normal. This has the importance that the resonance intensities can become independent from the X-ray incidence angle θ, at the so called magic angle. For the case of perfect linear polarization for planar orbitals the magic angle is 54.7 degrees. This means that if all the molecules are oriented at the magic angle, then the NEXAFS intensity is indistinguishable from that of a completely randomly oriented molecular film.

2.1.4 Resonant X-Ray Photoemission Spectroscopy (RPES).

Charge transfer dynamics is a topic with wide relevance in many fields, including femtochemistry, photochemistry, surface reaction dynamics, molecular electronics, solar energy, photosynthesis and photography [10]. There is nowadays an intense scientific interest to characterize and understand the nature and mechanisms of charge transfer across various interfaces, including molecule/metal, molecule/semiconductor and molecule/molecule interfaces. In particular when considering the electron transfer process at a molecule-substrate interface, it can be described as a spontaneous transition from a metastable initial state in molecules or substrates to a stable state, where the initial state (excited state) is generated by external excitation sources, such as photoabsorption. The electronic transition or interfacial electron transfer can be described as a consecutive tunneling process from the transiently occupied molecular state (initial state) through n ($n = 0, 1, 2, ...$) different discrete and localized bridge molecular states to the substrate continuum (final state) or vice versa. It is therefore clear that the interfacial electron transfer largely depends on the electronic interaction or wave function mixing between a discrete molecular state and the substrate continuum, as well as coupling between consecutive localized molecular states [11]. The electron transfer processes occur in the femtosecond time scale, therefore suitable experimental techniques are needed to probe these ultrafast processes. The most widely used technique for the direct access to dynamic electronic properties with high temporal resolution, down to a few fs, is the pump-probe technique, whereby an ultrafast laser pulse (pump) populates the sample into its excited state and a second laser pulse (probe), with an adjustable time delay, probes the transient excited states as a function of the delay time, by measuring the transmission, reflection, fluorescence or photoemission of the sample. Resonant X-Ray Photoemission Spectroscopy (RPES) provides an alternative route to pump and probe laser based techniques in studying charge dynamics at the femtosecond and sub-femtosecond time scale. In this chapter the fundamental ideas are presented, for more details several reviews have been published recently on the use of this technique in molecular systems [12, 13, 14, 15].

Analogous to the pump-probe technique, RPES relies on an intrinsic time scale, based on the lifetime of excited core-hole states, and it is therefore referred as core-hole clock spectroscopy. In the RPES experiment the valence band (VB) photoemission is measured as the photon energy is tuned across a specific absorption edge. This means that while doing a NEXAFS measurement, instead of summing up all or part of the electrons of different kinetic

energies emitted (AEY, PEY or TEY detection schemes described in the previous section) due to the annihilation of the core hole, formed after the promotion of the core level electron into an empty conduction band state or an unoccupied molecular orbital (UMO), the photoemission spectra are acquired, one for each photon energy. Whereas below the absorption edge the VB photoemission spectra reflect the occupied electronic structure of the measured system via direct photoemission process, at the X-ray absorption edge the spectra contain also contributions from the resonant autoionization emission. Note that the decay via non-radiative Auger electron emission dominates over the radiative emission [16] and that the core excited states are usually short lived. For most atomic species of organic materials (C1s at 284 eV, N1s at 401 eV and O1s at 531 eV) the decay takes place on the timescale of a few fs ($\tau_{C1s} = 6fs, \tau_{N1s} = 5fs, \tau_{O1s} = 4fs$) [17].

Although in many respects the near-edge X-ray absorption (NEXAFS) and autoionization electron emission make part of a single step process, the RPES is often visualized and understood as a two step process. In figure 2.8 the RPES working principle is summarized.

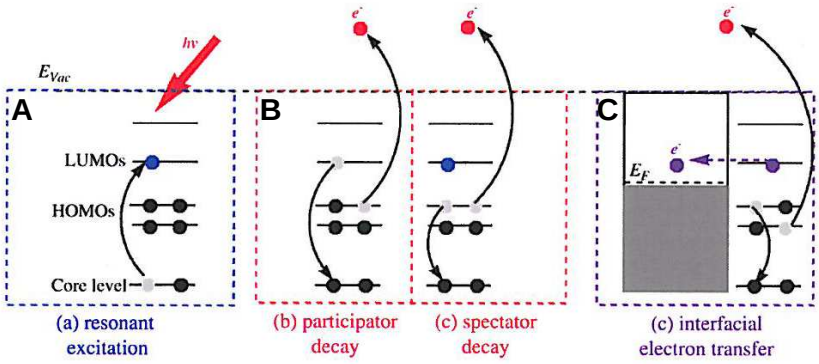

Figure 2.8: Schematic overview of the working principle of the RPES. (A) A core level electron is resonantly excited into the lowest unoccupied molecular orbital (LUMO) of the adsorbate. In the core-hole lifetime, this excited electron (B) can either participate in the decay process leading to a one-hole final state (participator decay) or be passive as a spectator leading to a two-hole-one-electron final state (spectator decay), or (C) directly transfer to the substrate conduction band, if the molecular orbital strongly couples with substrate density-of-states [12].

The core-hole is created by the X-ray absorption (fig.2.8 A), which can be followed by a core-hole autoionization. The creation of a core hole at the X-ray absorption edge in the figure involves resonant transitions from

the core electron occupied state to an unfilled molecular orbital (UMO). The radiationless decay of the resonantly excited system with a core-hole may then proceed via two distinct autoionization channels (fig.2.8 B): in the participator decay, the promoted electron participates in the decay process and the system is left in a final state with a single valence hole, whereas in the spectator Auger decay the promoted electron is left in the excited state and the Auger emission leaves the system final state with two valence holes plus an excited electron. The participator autoionization decay is energetically degenerate with the direct photoemission, yet it occurs resonantly with the creation of the core-hole. Core-hole assisted protoemission generally has much larger cross section for the core levels of interest and in the case of strongly localized systems like molecules it often dominates the valence band spectrum across the absorption edge [14]. It is worthwhile to note here that in the case of molecules adsorbed on solid substrates the electronic emission from the highest occupied molecular orbitals is often superimposed on the valence band photoemission from the solid substrate which makes the determination of the electronic structure of the adsorbate/substrate system quite a difficult task. Due to the resonant nature of electron emission process near the X-ray absorption edge, RPES may detect spectral features in the valence band spectra which are otherwise extremely difficult to resolve in a conventional X-ray photoemission experiment. There is a final point that should be underlined: for a participator decay the spatial overlap among the involved wavefunctions ($\psi_{core}, \psi_{UMO}, \psi_{OMO}$) is required, which makes the process intrinsically suitable for probing their spatial distribution [15]. In fact, the occurence of resonating spectral features in the VB spectrum in correlation with NEXAFS absorption peaks (core-UMO transitions) proves that the filled state wavefunction (ψ_{OMO}) is spatially located close to the core site and so must be also the ψ_{UMO}. This way RPES enables a direct chemical identification of the VB emission site. In other words, across the absorption resonance it is possible to assign various valence band peaks to the different chemical species that compose the material and also in certain cases to inequivalent sites of the same chemical element in the molecule if enough energy resolution is provided by the experimental apparatus [18].

If the transiently occupied molecular orbital is delocalized over many atomic centers, i.e., strongly coupled to the substrate, a transfer of the excited electron to the substrate (charge transfer) competes with the decay process that takes place during the core-hole lifetime. The core-hole then decays via the normal Auger channel (see fig. 2.8 C) and the resonant peak intensity results modified. By monitoring the intensity changes in the resonant peaks, the interface electron transfer on the low-fs or sub-fs timescale can be evaluated using the core hole lifetime as an internal reference clock.

In particular by comparing the peak intensities associated with the localized resonance and the delocalized ultrafast charge transfer process, a temporal range of charge transfer times (τ_{CT}) of $0.1\tau_{core} < \tau_{CT} < 10\tau_{core}$ (with τ_{core} the core hole lifetime) becomes accessible depending on the resolution and sensitivity of the spectroscopy. This is possible since the energies of the decay electrons will be different depending on whether the excited electron is still localized on that atom at the instant of core-hole decay or whether it has been transferred away before the core-hole decay (fig 2.9).

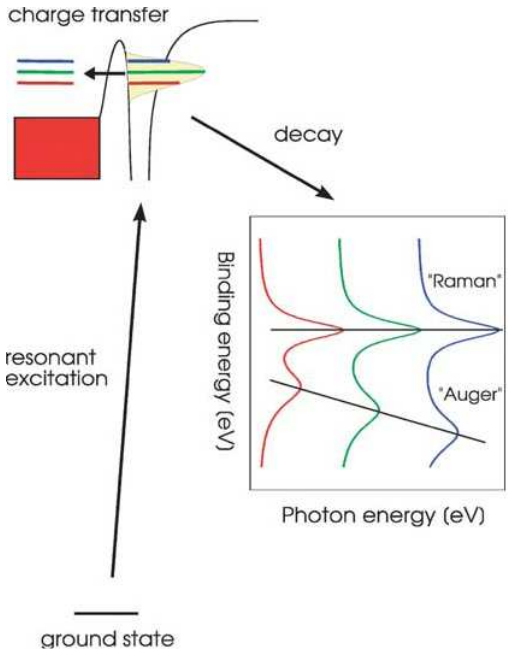

Figure 2.9: Scheme of the branching of the de-excitation paths of a resonant core excitation of an adsorbate. If the excited electron is transferred before core-hole decay then the kinetic energy of the secondary electrons emitted will remain constant with the photon energy (leading to Auger lines). If the electron is not transferred to the substrate, the binding energy of the secondary electrons emitted will remain constant with the photon energy (leading to Raman lines). [13]

In particular, in the case that the excited electron is still localized on the atom with the core hole, the decay spectra (called Raman decay which includes participator and spectator processes) will shift with changed photon energy $h\nu$, that means that the binding energy BE will stay constant. If the excited state has been transferred to the substrate before the core hole decay,

then it will take an excess energy $\Delta h\nu$ with it and the initial state of decay will always be the same, that is the Auger decay. The kinetic energies of these true Auger electrons behave in the way known from Auger spectroscopy: they are independent of how they have been created. The fact that the two spectral components shift differently when $h\nu$ is tuned through the resonance can be used to unequivocally separate those two components. At this point the extraction of charge transfer times can be made by considering the core hole decay and the charge transfer as two independent rate processes each with its characteristic exponential decay. The ratio of the total numbers of events through the two channels $N_{1,2}$ (each of which is proportional to the integral $I_{1,2}$ of its spectral component $P_{1,2}$) is proportional to the ratio of the rate coefficients $k_{1,2}$ or inversely proportional to that of the corresponding decay times $\tau_{1,2}$:

$$I_{1,2} = I(P_{1,2}(E))dE; \frac{I_1}{I_2} = \frac{k_1}{k_2} = \frac{\tau_2}{\tau_1}$$

For a certain atom and level, the core hole lifetimes, τ_{ch}, do not vary much with the chemical environment of the atom and can be taken from tables [13]. The charge transfer time, τ_{CT} can then be obtained directly from the ratio of the integrated spectral components:

$$\tau_{CT} = \frac{I^{ch}_{Raman}}{I^{CT}_{Auger}} \tau_{ch}.$$

2.2 Experimental apparatus.

All the experiments reported in this thesis were performed at the ALOISA beamline (INFM-CNR) at Elettra. Elettra is a synchrotron radiation facility located in Trieste, Italy. It is a third generation synchrotron radiation source operating at a storage ring energy of 2.0 and 2.4 GeV. The light is produced in a broad continuous spectrum extending from less than an eV to tens of keV, from the infrared to the hard X-ray. This allows performing investigations in many scientific disciplines where material structure can be examined by means of its interaction with the electromagnetic radiation.

The ALOISA (*Advanced Line for Overlayer, Interface and Surface Analysis*) beamline is a multipurpose beamline for surface science experiments [19]. It has been designed to work in a wide spectral range (120-8000 eV) and hosts two experimental chambers: the first one, ALOISA, is dedicated to X-ray diffraction, X-ray spectroscopy and X-ray absorption experiments, while the second one, HASPES, offers scattering of thermal helium atoms, X-ray photoemission spectroscopy and X-ray absorption. In the beamline optics is mounted a switching mirror which lets the beam passing directly

into the ALOISA chamber or deflects it (when inserted) to the HASPES chamber.

X-ray source and optics.

The ALOISA photon beam is produced by U7.2 Wiggler/Undulator Insertion Device of the Elettra sinchrotron. This is a planar undulator, with permanent magnets allocated in an array of 19 periods each of them 80.36 mm long for a total length of 1527 mm. This undulator produces photons in the range of 120-8000 eV. The main characteristic is the possibility to switch between two dispersing systems: a Plane Mirror/Grating Monochromator (PMGM), for the 120-2000 eV range, and a Si(111) channel-cut crystal for the 2.8-8.0 keV range [20] with a photon flux at the sample of about 5×10^{11} in the low energy range (120-2000 eV undulator mode) and about 5×10^{10} in the high energy range (2.8-8.0 keV wiggler mode) with spot size of about 40x200 μm^2 and a resolving power ($E/\Delta E$) between 2000 and 7500. The light is linearly polarized (polarization degree of about 95%) in the plane of the electron beam orbit (horizontal plane).

The complete optical layout of the beamline is sketched in figure 2.10.

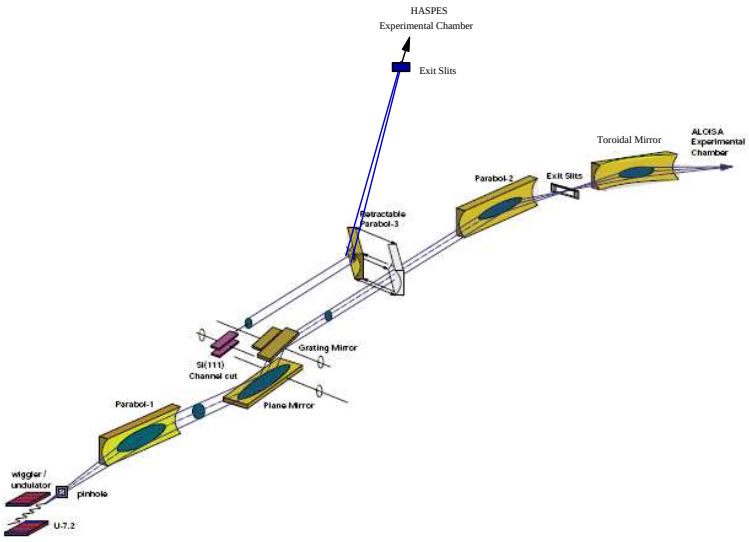

Figure 2.10: Sketch of the optics of the ALOISA beamline.

The light is collected from the pin hole by a paraboloidal mirror (P1) and collimated toward the dispersing system. Then the monochromatic beam

(still parallel) is focused at the exit slit (ES) by a second paraboloidal mirror (P2). The exit diverging beam is re-focused on the sample (placed at the center of the experimental chamber ALOISA) by a toroidal mirror (RT), producing a spot of approximately 20 $\mu m \times 150$ μm. The system is characterized by the absence of an entrance slit. Moreover the optics are used in the sagittal focusing configuration (i.e., perpendicular to the scattering plane) to minimize the aberrations in the dispersive plane induced by the slope errors. All the optics are designed to work at grazing incidence with a deflection angle of 1° for P1, P2 and RT. Due to the high power density generated by the insertion device, the first paraboloidal mirror and the PMGM and the channel cut crystal are water cooled. All the optical surfaces have a gold coating to minimize chemical contamination and losses in the photon flux. Moreover gold presents a large critical angle for reflection. A third paraboloidal mirror P3 is used to deviate the beam to the HASPES chamber. No additional refocusing mirrors are used in this case due to the very long distance of the HASPES chamber from the bemaline optics (14m). This way a low angular divergence of less than 0.3 mrad is obtained.

The ALOISA experimental chamber.

A sketch of ALOISA experimental chamber is depicted in figure 2.11.

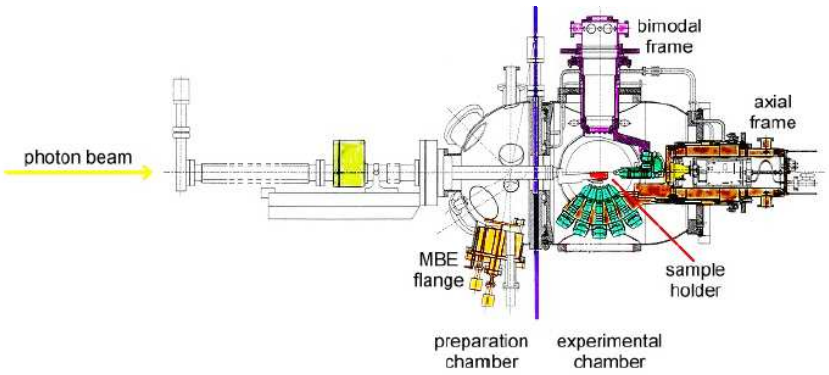

Figure 2.11: Sketch of the ALOISA experimental chamber.

The experimental chamber is composed by two parts: a hemispherical element dedicated to the sample preparation (preparation chamber) and a cylindrical one which hosts the electron analyzers and the photon detectors for sample investigations (main chamber).

The two elements are coupled via a large bronze ball bearing and a system of sliding o-rings. This configuration allows the complete rotation of the main chamber (with all detectors) around the synchrotron radiation (SR) beam axis, while the preparation chamber stands still. Two differential pumping stages allow the complete rotation of the main chamber and the frames, while maintaining a constant base pressure of 10^{-11}mbar inside the experimental chamber. The sample is placed onto a six-degree of freedom manipulator which is mounted into the hemispherical element with its main axis horizontal. The SR beam passes trough the whole manipulator and impinges at grazing incidence on the sample. The preparation chamber is equipped with a MBE (Molecular Beam Epitaxy) cryopanel which can host up to four evaporation cells. The cryopanel also holds two quartz microbalances for deposition flux calibration. A gas line allows high purity gases to be bled into the chamber. The ion gun for the Ar^+ bombardment enables sample sputtering and two filaments on the sample holder allow annealing of the sample up to 1100 K. An additional gas pipeline enables the liquid nitrogen cooling of the sample down to 150 K. A RHEED system (Reflection High Energy Electron Diffraction) with electron energy of 15 keV and the beam impinging to the surface at a grazing angle is avaible for checking the surface symmetry in-situ during deposition. The preparation chamber is additionally equipped with the sample transfer system and fast entry-lock allowing quick sample exchange.

In the main chamber, the detectors are hosted on two frames which are mounted inside the rotating element. The Axial Frame is mounted at the end of the cylindrical element and can rotate around the SR beam axis independently from the chamber. Five 33 mm electron analyzers are mounted on this frame. They are primarily dedicated for the APECS (Auger Photoelectron Coincidence Spectroscopy). There is also a phosphorous plate with the CCD camera mounted on the axial frame. The Bimodal Frame is mounted on the side of the cylindrical element and can rotate around an axis that is perpendicular to the SR beam axis; the rotation axis rotates around the SR beam axis when the cylindrical element rotates too. The bimodal frame hosts a 66mm hemispherical electron analyzer for angle resolved photoemission (AR-XPS) and photoelectron diffraction (PED). There is one Si-diode behind 1 mm collimators for measuring the total current for X-ray diffraction (XRD) and reflectivity (XRR). The bimodal frame additionally hosts two energy-resolved (Peltier-cooled) photodiodes (by Eurisis) operating in single-photon counting mode for X-ray diffraction. A wide-angle-acceptance channeltron is mounted on the axis of the bimodal frame, which is used for measuring the partial electron yield in near edge X-ray absorption fine structure (NEXAFS) experiments. The channeltron is equipped in front of its apex with

an additional grid, held at an adjustable negative potential to perform PEY NEXAFS measurements.

Finally the three rotations of the sample holder allow the sample to be rotated around the SR beam axis in order to select the surface orientation with respect to the SR polarization, to select both the grazing angle and the orientation of the surface symmetry axis with respect to the scattering plane. All the movements of the optical elements of the beamline are implemented in the Beamline Control System, the remote control system developed at ELETTRA to control the beamlines according to the ring status, and to guarantee safe working conditions. A home-made LabView program has been developed for the data acquisition, detectors control and movement of the manipulator and main chamber.

The HASPES experimental chamber.

The HASPES (Helium Atom Scattering and Photoelectron Spectroscopy) vacuum chamber consists of a main upright standing cylindrical void, a prechamber with helium atom source and a chamber for the helium detection with a quadrupole mass spectrometer. A top view scheme is reported in figure 2.12.

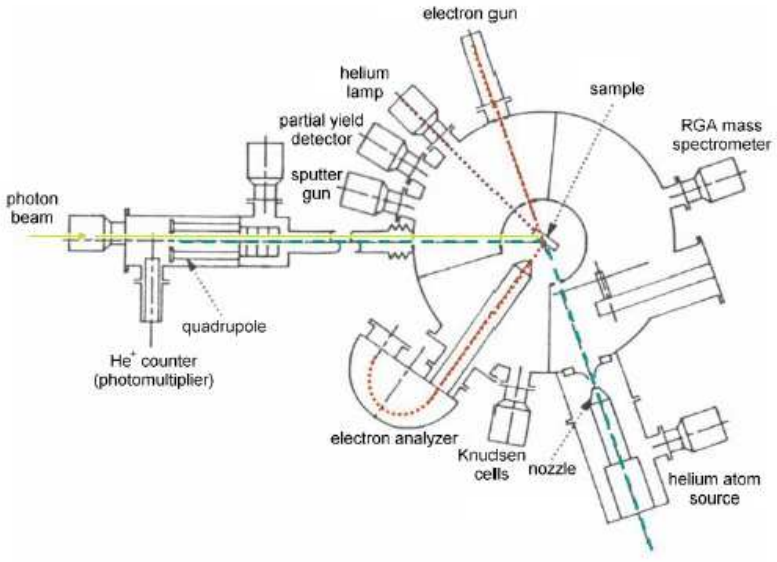

Figure 2.12: Sketch of the HASPES experimental chamber.

HASPES uses the low-energy monochromatic SR beam in the 120-1000eV energy range. The SR beam enters the HASPES chamber through the He detection part so the beam path coincides with the He scattered beam, but has the opposite direction. The main chamber hosts a vertically mounted VG CTPO manipulator with six degrees of freedom and high-precision positioning. The chamber has a fixed source-sample-detector angle of 110° for HAS and 55° for XPS. All the manipulator rotations are motorized and navigated via a home-made Labview program, which also manages the data acquisition. The manipulator is provided with a thermal link to a small cryostat filled by circulating liquid nitrogen or liquid helium. Together with the tungsten filaments or resistive (ohmic) heating (in case of semiconducting sample) it allows the sample temperature to be maintained in the 100-1100K range. The sample holder is interchangeable with that of the ALOISA chamber.
The He beam is formed by supersonic expansion from the stagnation chamber into vacuum through a nozzle with 10 μm in diameter, consisting of a standard diaphragm for electron microscopes [2]. The strong pumping system ensures that the ratio of the stagnation pressure, p_0, inside the nozzle to the background pressure in the beam chamber, p_1, is as high as $p_0/p_1 \approx 10^7$, so that no shock structures occur in the expansion region and a smooth transition from continuum to free-molecular flow takes place a few mm region downstream from the nozzle. The pressure of He in the stagnation chamber can be set in the 10-100 bar range, defining the flux and the monocromaticity of the He beam. A skimmer with the shape of truncated cone with aperture diameter of 0.5 mm follows the nozzle at a distance of about 25 mm. The angular divergence of the beam, which equals $8 * 10^{-6}$ sr. Just downstream from the skimmer, the chopper selects He beam pulses for inelastic scattering measurements. The chopper is followed by another collimator, through which the He beam enters the experimental chamber and presents a cross section of about 0.7 mm at the scattering center. The beam energy is selectable between 18.6 and 100 meV by controlling the temperature of the stagnation chamber.
Scattered He atoms enter the detection chamber through another set of collimators. Neutral atoms are first ionized by the transverse electronic beam and then filtered through the quadrupole mass spectrometer assembly. Electrons in transverse beam have kinetic energy of about 100 eV, corresponding to the maximum cross section for the ionization of He atoms, where the ionization efficiency reaches about 10^{-5}. The ions entering the quadrupole region are then selected according to the desired charge to mass ratio, e/m, with an accuracy of 0.05 e.m.u.. Finally, the He^+ ions followed by knocked-out electrons are multiplied through a series of 17 dynodes and counted by a computer. The transfer width of the apparatus (lateral correlation length of

the beam) is found to be 1200 Å.

On the main chamber are also attached a differentially pumped helium lamp to provide ultraviolet radiation and a 150 mm high resolution hemispherical electron analyzer. It hosts a 48-segment anode behind two serially-coupled multichannel plates (MCP) and offers an energy resolution of 0.5 % of the pass energy, reaching the maximum resolution of 17 meV. There is also an electron gun mounted in the scattering plane and emitting the electrons with 10-1000 eV kinetic energy that offers the angularly well resolved electron detection - LEED technique. A channeltron is also mounted at an angle of 50 degrees from above the horizontal scattering plane for the partial electron yield detection in the near edge X-ray absorption fine structure (NEXAFS) experiments. The main chamber is furthermore equipped with an ion gun for Ar^+ sputtering and a liquid-nitrogen cooled cryopanel, hosting three Knudsen evaporation cells. There is also a fast entry lock allowing quick sample exchange.

Bibliography

[1] Farias D., Rieder K.H., Rep. Prog. Phys 61 (1998) 1575

[2] D. Cvetko, A. Morgante and F. Tommasini, K. C. Prince, M. Sastry, Measurements, Science and Technology 3 (1992) 997

[3] Cvetko D., Self-Ordering of Low Dimensional Systems: Erosion and Growth at Solid Surfaces, PhD thesis 1996

[4] Zaremba E., Kohn W., Phys. Rev. B 15 (1977) 1769

[5] Harrish J., Liebsch A., J. Phys. C 15 (1982) 2275

[6] Norskov J. K., Lang N., Phys. Rev. B 21 (1980) 2131

[7] Fadley C.S., Basic Concepts of X-Ray Photoelectron Spectroscopy in Electron Spectroscopy: Theory, Techniques and Applications, C. R. Brundle and A. D. Bakes, eds. (Academic Press, London, 1978), 2, 124

[8] Stöhr Nexafs Spectroscopy, Springer-Verlag, Berlin, 1992

[9] Ultra-fast charge transfer dynamic in thin and ultra-thin films of organics studied with synchrotron radiation, PhD thesis 2007

[10] Miller J. D., Surface Electron Transfer Processes, VCH Publishers, 1995

[11] May V., Kühn O., Charge and Energy Transfer Dynamics in Molecular Systems, Wiley-VCH, Weinheim, 2004

[12] Wang L., Chen W., Wee A., Surface Science Rep (2008)

[13] Menzel D., Chem Soc Rev, 37 (2008) 2212

[14] Vilmercati P., Cvetko D., Cossaro A., Morgante A. ?

[15] Brüwiler P.A., Karis O., Märtensson N., Rev Mod Phys 74 (2002) 703

[16] Walters D.L., Bhalla C.P., Phys Rev A, 3 (1971) 1919

[17] Darrah T., Coville M., Phys Rev A 43 (1991) 6053

[18] de Jong M.P., Friedlein R., Sorensen S.L., Öhrwell G., Osikovvicz W., Tongsted C., Jönsson S.K.M., Fahlman M., Saloneck W.R., Phys Rev B, 72 (2005) 035448

[19] http://www.tasc.infm.it/research/aloisa/scheda.php

[20] L. Floreano, G. Naletto, D. Cvetko, R. Gotter, M. Malvezzi, L. Marassi, A. Morgante, A. Santaniello, A. Verdini, F. Tommasini, G. Tondello, Rev. Sci. Instrum. 70 (1999) 3855

Chapter 3

Self-assembly of L-methionine on metal surfaces.

3.1 Introduction.

The fabrication methods employed in the microelectronic industry have been refined to produce smaller and smaller devices, but it is well known that they will soon reach their fundamental limits. As described in chapter 1, a promising alternative route to even smaller functional systems with nanometer dimensions is the self-ordering and self-assembly of atoms and molecules on atomically well-defined surfaces [1]. In this framework the understanding of the supramolecular aggregation starting from the basic interactions of the constituent molecules is a prerequisite to eventually control the self-assembly process.

In general, adsorbed molecules are dynamic and evolving entities displaying different characteristics in response to conditions such as adsorption temperature and adlayer coverage. This range of response is directly attributable to the functional groups of the molecules which can lead to a number of surface-molecule and molecule-molecule interactions. Most of these interactions are balanced in a delicate equilibrium, leading to a rapid system response to varying conditions. This complexity in behavior is manifested at two levels: at the local level, variations of the molecular form, orientation and bonding are observed; while at the extended level, a variety of ordered assemblies can be observed. Therefore it can be appreciated that even the combination of just one type of organic molecule and one surface can unleash a cascade of phases, each possessing a different combination of chemical, orientational and self-organizational behavior. This concepts are clarified in the following graph (fig. 3.1).

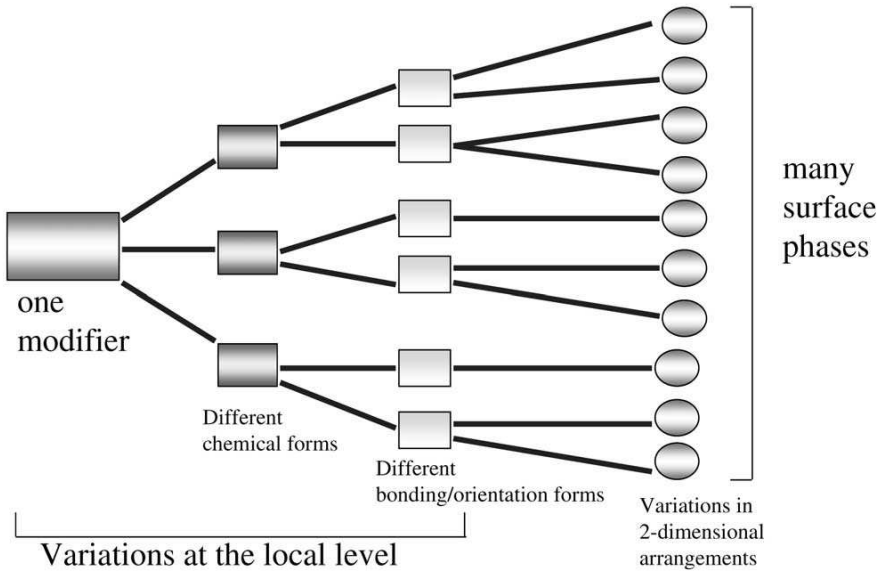

Figure 3.1: Schematic diagram to show how the adsorption of one simple molecule can unleash a cascade of phases on a particular surface from ref.[2, 3].

Amino acids are an important class of building blocks for molecular self-assemblies that are of interest for molecular architecture on metal surfaces. The study of their self-assembly on metal surfaces is motivated by the fundamental understanding of protein-surface linking and by possible applications in the field of the electronic industry but it is also connected to the development of bioanalytical devices or biocompatible materials. All of them contain the amine (-NH_2) and the carboxyl (-COOH) functional groups and can be represented as in figure 3.2:

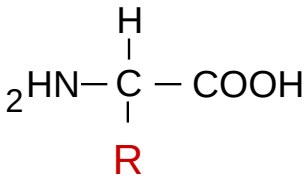

Figure 3.2: General molecular structure of the amino acids. R is an organic substituent.

Their general formula is H_2NCH-R-COOH, where R is an organic sub-

stituent. Different aminoacids are characterized by different R substituents, which can contain additional functional groups.
The -NH_2 and -COOH groups can change their oxidation state depending on the environment: aminoacids can exist in a variety of chemical forms that are zwitterionic (NH_3^+CH-R-COO^-), anionic (NH_2CH-R-COO^-), cationic (NH_3^+CH-R-COOH) and neutral (NH_2CH-R-COOH) forms. The neutral form is found for molecules in the gas phase, while the zwitterionic form is found in the solid state: aminoacids in the zwitterionic state crystallize via hydrogen bonding. The anionic and cationic forms are found for the molecules in solution and their chemical nature depends on the pH of the solution. This flexibility in chemical nature also persist when aminoacids are adsorbed at surfaces with the form that is present being metal dependent [2]. The binding of the amino acids to the substrate is governed on one hand by the interaction of their functional groups with the metal surface, and therefore the chemical form of the aminoacid determines the binding geometry. On the other hand molecule-molecule interactions determine the self-assembly geometries thanks to hydrogen bond interactions that allow molecular crystallization. For any given chemical form of an aminoacid there is a great flexibility in the supramolecular organizations that can occur at a surface, i.e. amino acid/metal system presents polymorphism [3].

L-methionine is a sulphur containing aminoacid which was shown to self-assemble on Ag(111) forming long range ordered nanogratings [4]. The gratings are composed of rows of zwitterionic molecules with length in the millimeter range whose interstripe distance can be tuned by controlling the surface coverage. These tunable nanogratings were used for example as templates for the immobilization of Co and Fe atoms into regular arrays [5]. In section 3.3 a summary of the results on the characterization of the self assembly of L-methionine molecules on Ag(111) complemented with more recent observations will be presented. The experimental techniques employed are: Helium Atom Scattering (HAS) which provides information on the morphology of the films, X-ray Photoemission Spectroscopy (XPS) and Near Edge X-Ray Absorption Spectroscopy (NEXAFS) which provide information on the chemical state of the molecules, on the involvement of different functional groups in molecule/molecule and molecule/surface interactions and on the geometry of the adsorbed molecules. The details about these techniques have been presented in chapter 2, here I want to underline that XPS is particularly well suited for obtaining information on the involvement of different functional groups in the chemical bonds and on their chemical state since the same atoms in different chemical bonding environments can be separated through their chemical core level shifts. NEXAFS spectroscopy is sensitive to fine details of the electronic structure of organic molecules, so that it can

give information to reveal the exact character of the chemical bonding and the orientations of the bonds.

The formation of such large and regular gratings of methionine molecules on Ag(111) is surprising. Since the molecules are in the zwitterionic form as in the solid crystals, hydrogen bonding could be the key interaction driving the assembly. However even the substrate should play a role. One of our aims is to understand which is the role of the substrate in the self-assembly of L-methionine molecules, therefore we have studied their assembly on different metal substrates. The results will be presented in this chapter.

In section 3.4 the role of the substrate in the formation of the nanogratings will be investigated by comparing the self-assembly of L-methionine molecules on two different metal surfaces: Au(111), that has a similar geometry and lattice parameter of the Ag(111), and Au(110), whose surface atoms present a different coordination with respect to Au(111). Gold is a technologically important material for which sulphur has a specific binding affinity. In fact one common way for immobilizing proteins on gold surfaces is to insert in their sequences methionine or cysteine (another sulphur containing amino acid) residues with genetic engineering techniques [6, 7]. However while cysteine is known to form strong covalent bonds to gold through the thiol group [8], the binding to gold of the methionine is not completely understood. Cooper et al.[9] and LeParc et al.[10] studied films of methionine grown on polycrystalline gold and on Au(110), and attributed the binding to the surface to the lone pairs localized on the sulphur and the nitrogen atoms. In chemistry, the lone pair is a (valence) electron pair of an atom without bonding or sharing with other atoms. According to recent STM break junction measurements and theoretical calculations the binding through the lone pair is stronger with undercoordinated gold atoms [11, 12], therefore we expect the molecules to bind stronger on Au(110) with respect to Au(111). From the measurements reported in section 3.4 it is clear that L-methionine molecules deposited on Au(111) and on Au(110) present different chemical states: the former are zwitterionic while the latter are ionic and neutral. HAS measurements revealed that the morphology of the films formed on Au(111) is identical to the ones on Ag(111) and from XPS and NEXAFS measurements we can conclude that the amino group is not bound to the surface, but is involved in the formation of the zwitterionic dimers. The only functional group that can be interacting with the substrate is the thioether (C-S-C). On the other hand, XPS and NEXAFS measurements on L-methionine films on Au(110) revealed that in this case both the amino and the thioether groups are involved in the formation of the bond to the surface and the geometry of the adsorbed molecules is completely different with respect to the ones on Au(111) and Ag(111), as confirmed by NEXAFS measurements.

In section 3.5 the self-assembly of L-methionine molecules on Cu(111) will be presented. Cu(111) surface presents the same symmetry of Ag(111) and Au(111) surfaces, but the lattice parameter is 10% smaller. On Cu(110) surfaces most of the aminoacids are known to adsorb via the amino and carboxyl groups [13, 14, 15] and these interactions can inhibit the formation of the nanogratings. At temperatures below 250K L-methionine molecules assemble in the zwitterionic chemical state, as on Au(111) and Ag(111), but they originate only short stick-like clusters without forming long nanoarrays. If we suppose that the amino and carboxyl groups are not involved in the bonding with the surface but only in the hydrogen bonding, the different geometry of the final assembly can be explained with the molecules adsorbing as different conformers to match the smaller lattice parameter. At higher temperatures there is an interesting transition from zwitterionic to anionic molecules. From NEXAFS and XPS measurements we can attribute this transition to the deprotonation of the molecules and to the bonding to the surface via the amino and carboxyl groups. The anionic phase is again characterized by regular nanogratings, whose stabilization is connected to the polarization effect of the metal.

In conclusion, the formation of the zwitterionic nanogratings is controlled by the hydrogen bonding and takes place only on (111) surfaces with lattice parameter comparable with the full extension of the molecule (5.8 Å). Au(110) and Cu(111) (at temperatures of 330K) are catalytic surfaces on which the bonding of the L-methionine molecules involves the loose of a proton and takes place through the amino and/or the carboxyl groups. On these surfaces it is possible the formation of nanogratings with different chemical nature.

3.2 Experimental Details

All the measurements presented in this chapter were performed at the ALOISA/HASPES beamline. The Ag(111), Au(111), Cu(111) and Au(110) samples were prepared in ultrahigh vacuum by repeated Ar+ sputtering cycles, followed by annealing at temperatures of about 700-800K. Before each deposition the surfaces were checked to be contaminat free (oxygen, carbon, sulphur). The enantiomerically pure L-methionine molecules (purity 99.5%; Sigma-Aldrich, St. Louis, MO) were vapor-deposited onto the substrates from a borum nitrite crucible heated to a temperature of 370 K. All XPS and NEXAFS spectra have been measured from freshly deposited films and by keeping the sample temperature below 150K to minimize the radiation damage. In fact exposures to the synchrotron radiation beam can cause

molecular damage which becomes evident in the modification of the XPS profiles [16]. The damage can be reduced to substantially lower rates when the sample is kept below 300 K. The reported XPS spectra have been taken with an overall energy resolution of 300 meV with a beam of photon energy 600 eV [17]. The binding energies on the XPS spectra were calibrated with respect to the literature values for $Au_{4f_{\frac{7}{2}}}$, $Ag_{3d_{\frac{5}{2}}}$ and $Cu_{3p_{\frac{3}{2}}}$ that are 84 eV, 368.3 eV amd 75.2 eV respectively [18, 19]. All the spectra were fitted with Voigt curves plus a background obtained with polinomial curves plus Shirley backgrounds. C K-edge and N K-edge partial yield NEXAFS measurements were performed on the sample with an incident grazing angle of 6°. The absolute photon energies were calibrated with the absorption spectra of gas phase CO and N_2 measured in the ALOISA ionization cell [17]. All the measured spectra were normalized by dividing the signal from the film with the one of the clean substrate, as described in [20].

3.3 L-methionine on Ag(111).

3.3.1 Film morphology.

The growth of L-methionine thin films on Ag(111) was studied by Schiffrin et al.[4] by means of the combination of two experimental techniques: Scanning Tunneling Microscopy (STM) and Helium Atom Scattering (HAS).

STM measurements revealed that the self-assembly of L-methionine molecules on Ag(111) is characterized by the formation of one dimensional elongated structures (stripes) that follow the close-packed $< 110 >$ orientations of the substrate (fig. 3.3(a)). The distance between methionine stripes strongly depends on the coverage θ. If the coverage is $0.1 < \theta < 0.6$ ML, methionine rows order in domains with interstripe distances in the range $85 - 190$ Å (fig. 3.3(b),(c)). The stripe lengths are in the micrometer range and the gratings are stable at room temperature. If the coverage θ is $\theta > 0.65 - 0.7$ ML, L-methionine rows merge and form highly anisotropic 2D molecular islands (fig. 3.3(d)).

The formation of ordered nanogratings on the surface can be measured by means of Helium Atom Scattering experiments. HAS, as already described in chapter 2, is a diffraction technique that maps the reciprocal space, while STM measures the structures in the real space. By using the kinematic theory it is possible to easily determine the position of the diffraction peaks.

In figure 3.4(a) and (b) are reported respectively the real space arrangement of the atoms of a clean (111) surface and the corresponding diffraction pattern. The arrows are the basis sets for the two spaces, that will be used

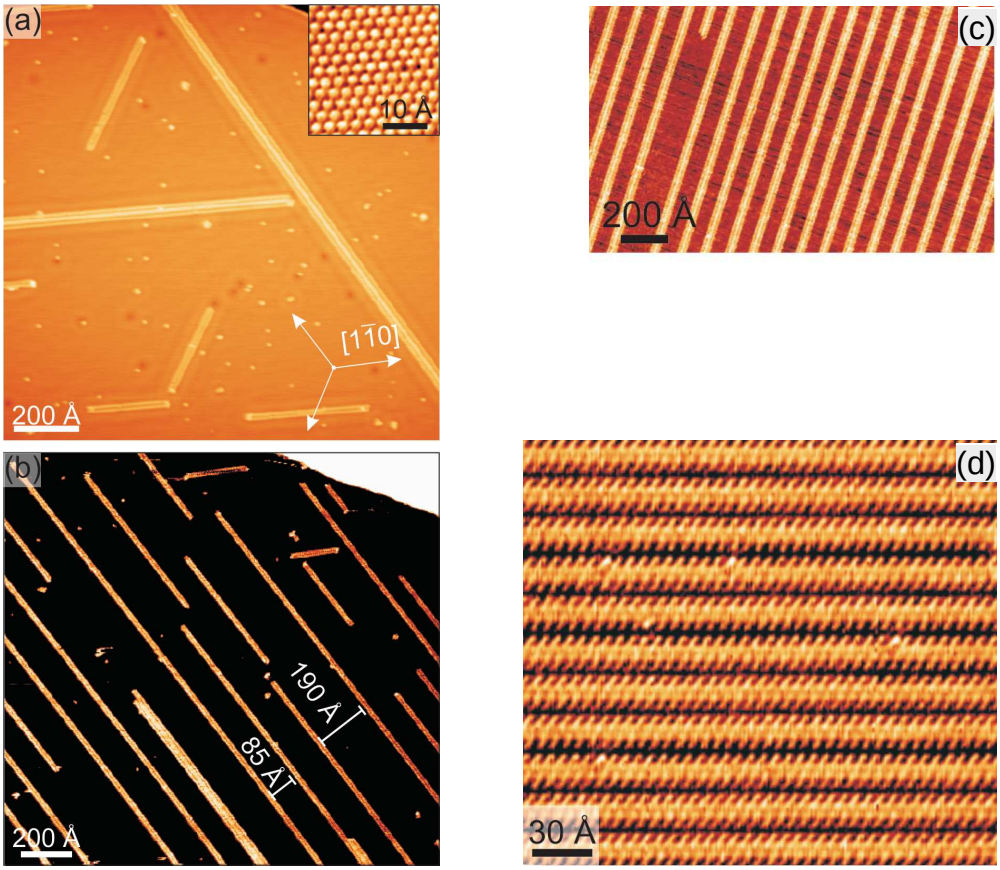

Figure 3.3: Low-temperature (4K) STM topographic data of L-methionine self-assemblies on Ag(111) formed at various coverages. (a) $\theta = 0.05ML(I = 0.7nA, U = -120mV)$ Inset: Atomic resolution of Ag(111). (b) $\theta = 0.12ML(I = 0.8nA, U = -200mV)$. (c) $\theta = 0.38ML(I = 0.1nA, U = -500mV)$.(d) $\theta = 1ML(I = 0.11nA, U = -250mV)$. From ref [4].

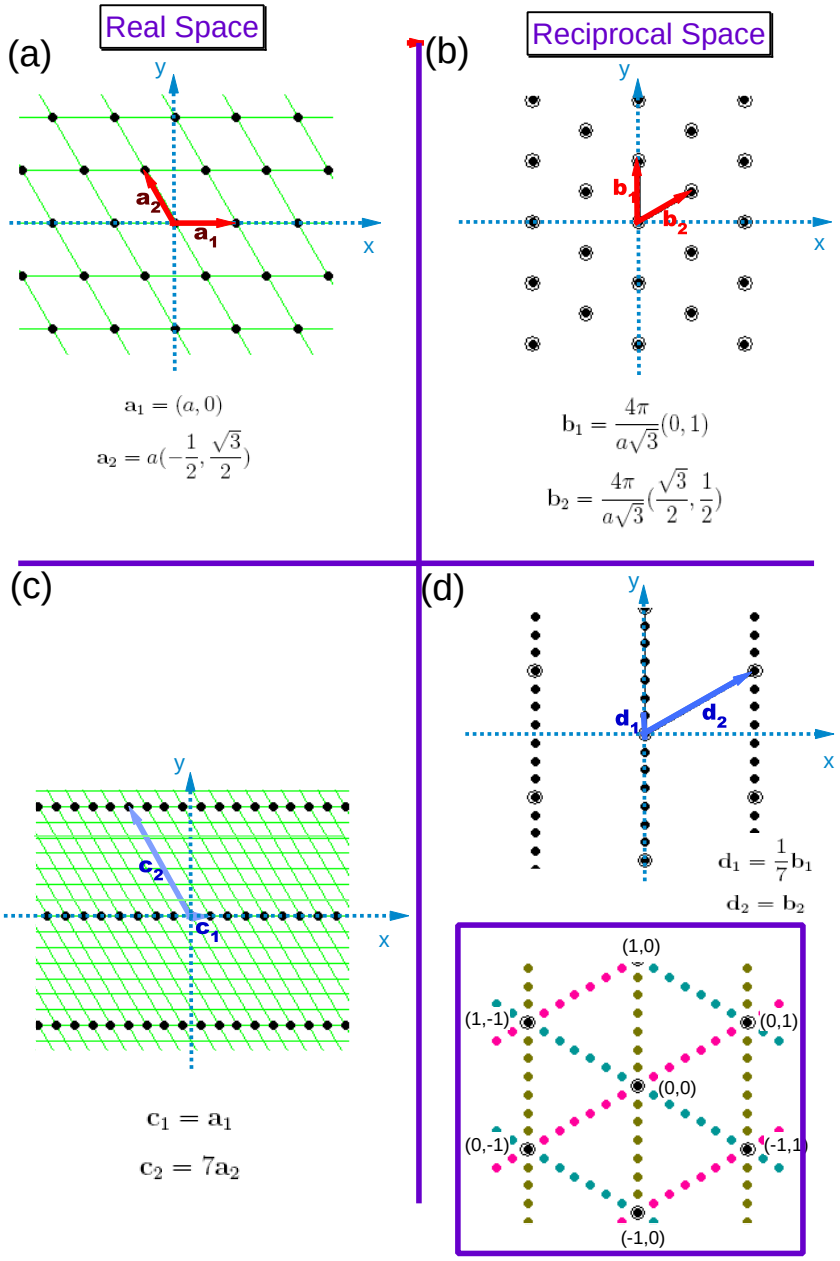

Figure 3.4: (a) Arrangement of the atoms in a clean (111) surface. (b) Diffraction pattern for the clean (111) surface. (c) (1x7) Superstructure on the clean (111) surface: this structure is the one of the L-methionine nanogratings. (d) Diffraction pattern for the structure (c) considering one single domain (top figure) or three domains (bottom figure).

in this chapter. If we consider for example the nanograting reported in fig. 3.4(c) (an arrangement of a L-methionine nanograting with the rows spaced by $7a\frac{\sqrt{3}}{2}$), the corresponding reciprocal space is reported in the top scheme of fig. 3.4(d). This pattern is the combination of the previous one plus some extra spots along the direction identified by $\mathbf{b}_1$. By taking into account that because of the surface symmetry L-methionine nanogratings are formed following all the three equivalent $< 01 >$ directions, the final diffraction pattern will contain diffraction spots in three equivalent directions, that means that it will be composed of all the markers in the bottom scheme of figure 3.4(d).

In figure 3.5(a) are reported helium diffraction spectra along the [10] substrate direction measured at different deposition stages.

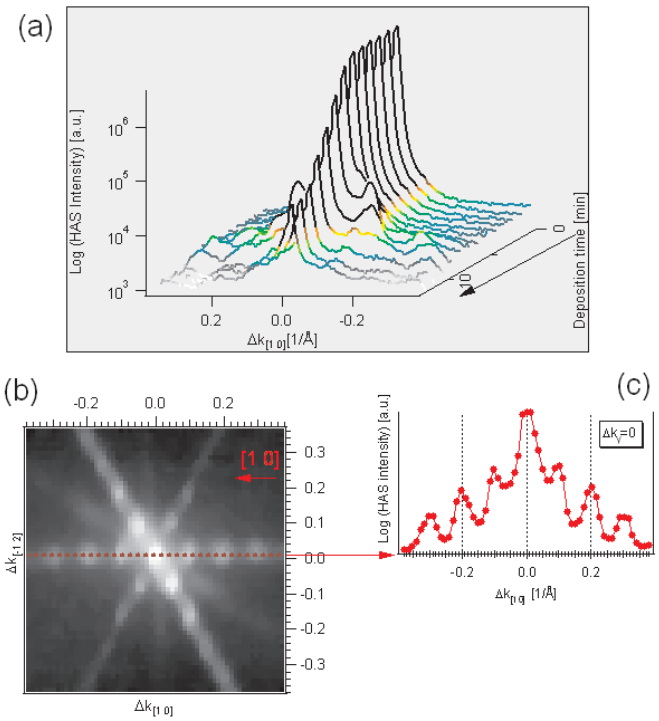

Figure 3.5: (a) HAS Diffraction spectra along the [10] direction acquired during deposition. (b) 2D helium diffraction map around the specular peak for a submonolayer coverage of L-methionine. (c) Line profile of (b) representing a diffraction scan along the [10] direction.

The deposition is performed at room temperature. In the first spectrum (corresponding to deposition time zero) only the specular diffracted peak arising from the substrate is visible. It should be noted that the distance

from the specular of the first order diffraction peaks in the reciprocal space for the clean (111) surface is $\frac{4\pi}{a\sqrt{3}} = 1.778$ Å^{-1}, that is outside the range considered. As the coverage increases, the specular peak decreases down to a saturation intensity. In the intermediate range other diffracted peaks appear, corresponding to long range periodicity (hundreds of Angstroms). Their presence suggests the existence of a long range order of the adsorbates on the surface, that can be connected with the formation of the nanogratings observed by STM, as already explained. At the final deposition stages, when 2D islands are visible in the STM pictures (fig. 3.3(d)), the spacing between the stripes is not anymore visible by HAS.

Fig 3.5(b) is a 2D-helium diffraction map around the specular peak for a film of L-methionine at intermediate coverage ($\theta \approx 0.4$ ML). The presence of a periodic structure in real space gives raise to diffraction peaks that follow the $< 10 >$ orientations in the reciprocal space. Figure 3.5(c) is a section of the previous map and shows that the peaks are spaced by about 0.1 Å^{-1}, which corresponds to a periodicity of

$$D = \frac{2\pi}{k} = 63 \text{ Å}.$$

STM observations have evidenced that the widths of the stripes in the nanogratings are integer multiples of 19 Å and they are composed by two parallel lines of elliptical features with a long axis of 8 Å (fig. 3.9). This distance corresponds to the full extension of a single molecule and therefore each unit was identified with an individual molecule. The long axis of the methionine footprint is oriented at an angle of $60° \pm 5°$ with respect to the stripe orientation and the separation between two adjacent molecules in this direction amounts to 5.8 Å that is about twice the Ag(111) surface lattice parameter (2.88 Å): this can be an indication that the substrate coupling dictates the row periodicity.
In the coverage range $0.1 < \theta < 0.6$ ML, mostly stripes with 19 Å and 38 Å width are formed, i.e. they are composed by two or four methionine lines. By annealing methionine gratings at 320 K after deposition it is possible to promote the formation of regular gratings made of quadruple rows and decrease the number of the double rows. Hence, stripes of double or quadruple molecular rows are very close in energy, and the latter must be stabilized by interactions beyond direct intermolecular coupling. In order to understand the role of the flash in the formation of improved nanogratings, we have followed the evolution of the helium diffraction peaks while annealing an L-methionine film (fig. 3.6(a)). We started with a film with a periodicity of 81 Å (P1) and we annealed it up to 330 K. After an increase in the quality of the diffraction pattern, there is a transition to a different periodicity of 61

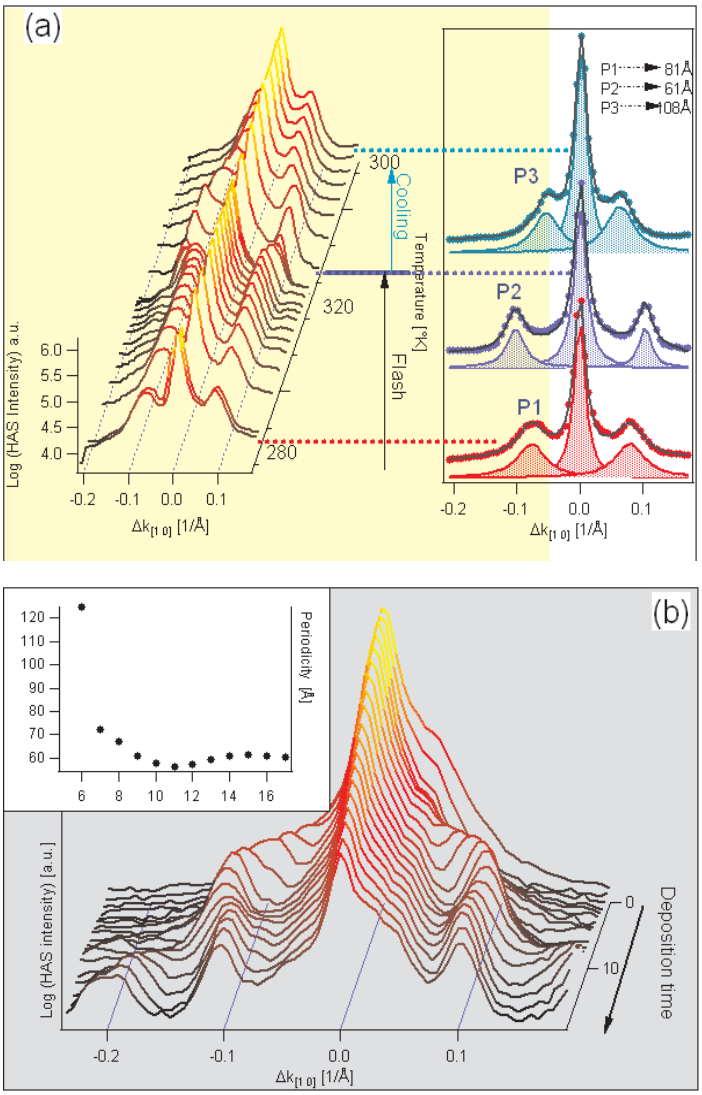

Figure 3.6: (a) On the left, Helium diffraction spectra along the direction [1 0] for different annealing temperatures of a L-methionine film. On the right is reported the fit of selected HAS spectra is reported. (b) Evolution of the HAS diffraction pattern along the direction [1 0] during a deposition with the substrate at 300 K. Inset, periodicity of the film at each deposition stage deduced from the fit of the position of the first diffracted peak.

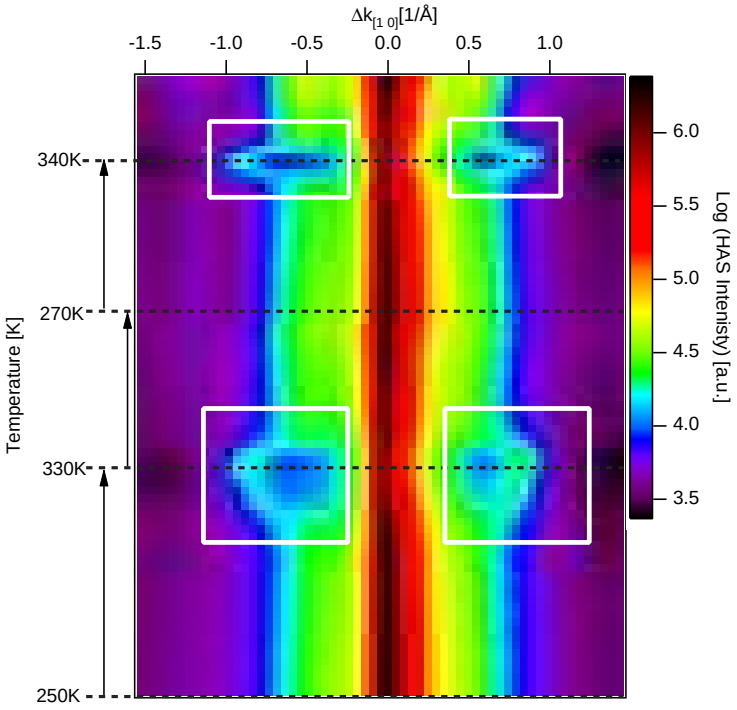

Figure 3.7: L-methionine phase transition for two consecutive heating cycles. In the abscissa the momentum exchanged is reported, in the ordinate the temperature is reported, while in the color scal the measured HAS intensity is represented. The temperature was not increased at constant rate, therefore the ring for the second transition (indicated by the white rectangles) looks smaller.

Å (P2). By heating to higher temperatures (350 K, not shown) desorption takes place, as indicated by the increase of the specular intensity. By cooling the methionine film with the periodicity of 61 Å (P2) down to 270 K a larger periodicity of 108 Å (P3) is recovered. The transition from P2 to P3 is a reversible phase transition. In fact in figure 3.7 consecutive HAS diffraction scans as a function of temperature for two heating-cooling cycles are shown. It is clear that the process is reversible.

In figure 3.6(b) are reported consecutive measurements of the HAS diffraction pattern during a deposition with the substrate kept at 330 K. In the inset is reported the fitted position of the first diffraction peak vs deposition time. At this temperature it is possible to obtain only gratings with periodicity P2 and this can be considered a saturation condition.

This scenario can be explained in the following way: after the deposition at low temperature the measured periodicity of 81 Å is originated by the coexistence of double and quadruple molecular rows. The heating of the sample produces the separation of quadruple rows into ordered double rows with a periodicity of 61 Å, and as a consequence the spacing between the lines decreases. As soon as the sample is cooled down, quadruple rows are recovered with a periodicity of 108 Å.

3.3.2 Molecular chemistry and the coupling model.

We have already observed that under certain conditions amino acids are known to be zwitterions, that means that the carboxyl groups are deprotonated ($-COO^-$) and the amino groups are protonated ($-NH_3^+$). The hydrogen bonding between zwitterions is responsible of the formation of layered amino acid crystals and we will show in this paragraph that it is also responsible of the formation of L-methionine nanogratings on Ag(111).

X-ray photoemission spectroscopy (XPS) measurements have been performed in order to determine the chemical state of the molecules [4]. The N1s and O1s XPS spectra in figure 3.8 show a single component respectively at $E_{N1s} = 401.15 \pm 0.10$ eV and $E_{O1s} = 531.2 \pm 0.1$ eV, indicating a unique chemical state of the amino acid. In previous XPS experiments performed on the L-cysteine/Au(110) system [8], the N 1s spectra related to the neutral amino group NH_2 and the positively charged $-NH_3^+$ group were assigned respectively to peaks at 399.5 eV and 401.5 eV. Moreover, the O1s spectra of the same system showed peaks at 531.2 eV, 532.3 eV and 533.6 eV, with the first corresponding to the equivalent resonating oxygens of the carboxylate group $-COO^-$ and the other two corresponding to the chemically inequivalent oxygen atoms of the $-COOH$ group. Following the same assignments, L-methionine molecules on Ag(111) are in the zwitterionic state, therefore

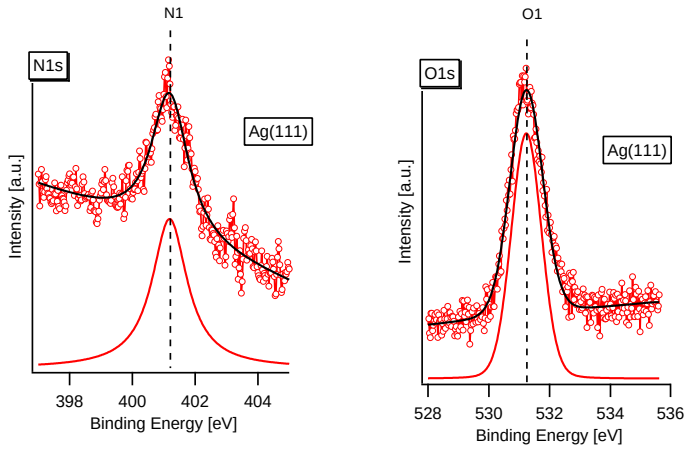

Figure 3.8: XPS N 1s and C 1s spectra of a monolayer of L-methionine on Ag(111). The dotted lines are the experimental data and the black lines the result of the fit. On the bottom of each spectrum the peaks obtained from the best fits are also reported (red lines).

nanogratings have zwitterionic nature as expected.

In fig 3.9(a) a model for the assembly of double rows of molecules is reported [4]. In this model dimerization between two amino acid zwitterions and lateral coupling are accomplished through hydrogen bonding involving the ammonium and the carboxylate group. The type of interactions that were taken into account was esthabilished from the results of a simple molecular mechanics simulations for a pair of methionine molecules [4]. The same adsorption scheme was applied to explain the assembly of the molecules in 2D islands. In fig 3.9(b) the structure proposed in ref [4] is reported for a saturated L-methionine monolayer that uses the same characteristic pairing structure. In the model red circles represent the Ag(111) atomic lattice. By describing the unit cell of the Ag(111) lattice with the vectors $\vec{a}_1$ and $\vec{a}2$, the lateral methionine ordering is commensurate along the direction parallel to $\vec{a}_1$, whereas it is not commensurate along $\vec{a}_2$. If $\vec{b}_1$ and $\vec{b}_2$ are the vectors of the unit cell of the supramolecular lattice, then $\vec{b}_1 = 2\vec{a}_1$ and $\vec{b}_2 = \frac{5}{2}\vec{a_1} + \frac{15}{2}\vec{a}_2$ [4]. Along the growth direction the molecule is adsorbed at equivalent substrate sites, whereas within a given molecular dimer two molecules bind differently to the surface.

We have performed XRD (X-ray Diffraction)and RHEED measurements on the methionine monolayer (not shown) and the periodicity along $\vec{a}_2$ results

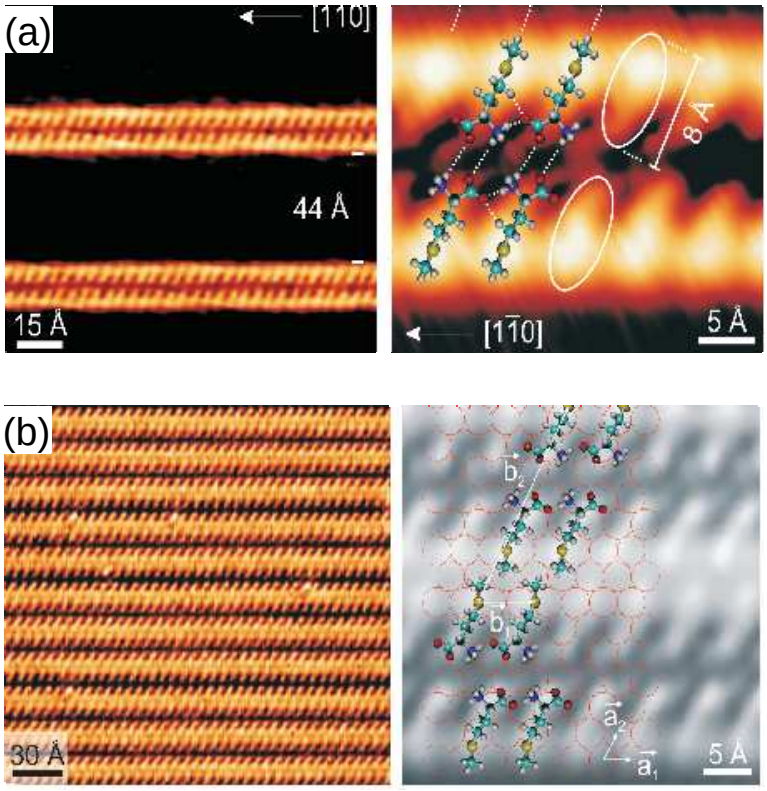

Figure 3.9: (a) On the left, STM Molecular resolution imaging of double rows of L-methionine with 61 Å periodicity (I=0.6 nA, U=-500 mV). On the right, schematic arrangement of the molecules in the double rows: each molecule appears as an elliptical feature with a long axis of 8 Å. They are arranged in pairs, with a lateral separation of 5.8 Å corresponding to about twice the nearest-neighbor distance between silver surface atoms (2.88 Å). (b) On the left, STM Molecular resolution image of saturated L-methionine monolayer (I=0.11 nA, U=-250 mV). On the right, proposed model for the self-assembly. The molecular ordering follows the atomic lattice of the Ag(111) substrate. Vectors ($\vec{a}_1$, $\vec{a}_2$) define a basis for the unit cell of the Ag(111) atomic lattice (I=0.30 nA, U=200 mV). The unit cell of the monolayer structure is marked in white. Images from ref [4].

$\vec{b}_2 = 7\vec{a}_2$. This discrepancy can be explained by taking into account that the measured XRD peaks are generated by the coherent sum of contributions from domains whose width can be estimated to correspond to the lateral extension of six L-methionine double lines. From the STM pictures 3.9(b) it is visible that the periodicity over this range shows spatial variations: in fact the width of the black lines is not constant. When measuring the unit cell from the STM images these variations probably become averaged in an incommensurate cell.

In conclusion, in this section the self-assembly of L-methionine on Ag(111) was reviewed. The molecules assemble in tunable nanogratings of zwitterionic nature. In the next section we will compare the adsorption and assembly of L-methionine molecules on Au(111) and Au(110) surfaces.

3.4 L-methionine on Au(111) and Au(110)

3.4.1 Film structure and morphology on Au(111).

L-methionine monolayers on Au(111) were grown by thermal evaporation with the substrate kept at 300 K. In the left graph of figure 3.10 the variation of the intensity of the specular peak I(0,0) of the helium diffracted signal during deposition is reported. At the deposition time labeled as (A), the surface is clean and the intensity of the specular peak is maximum. The helium diffraction map of the clean surface is reported in the right graph of fig. 3.10. It corresponds to the well known $22 \times \sqrt{3}$ herringbone reconstruction [21].

At the deposition time (B), the surface is partially covered and the intensity of the specular peak is decreased. The helium diffraction map of the film at this coverage is reported in the graph on the left of fig. 3.11: there is a diffraction structure along the [1 0] direction indicated by the dashed yellow lines (the directions are identified with the conventions in fig. 3.4). By comparison with the results on Ag(111), this structure can be associated with the formation of 1-D arrays of molecules spaced on average by 40 Å. Moreover there is another structure rotated with respect to this one that can be the signal from the herringbone reconstruction of uncovered substrate regions.

At the deposition time (C), the helium I(0,0) signal saturates close to zero, indicating the full shadowing of the substrate surface, possibly corresponding to the completion of the first layer. The helium diffraction pattern close to the specular (not shown) presents no diffraction structures, therefore we cannot appreciate any long range order. The RHEED diffraction pattern of the monolayer (fig. 3.11 right graph) reveals a times 7-fold periodicity along the

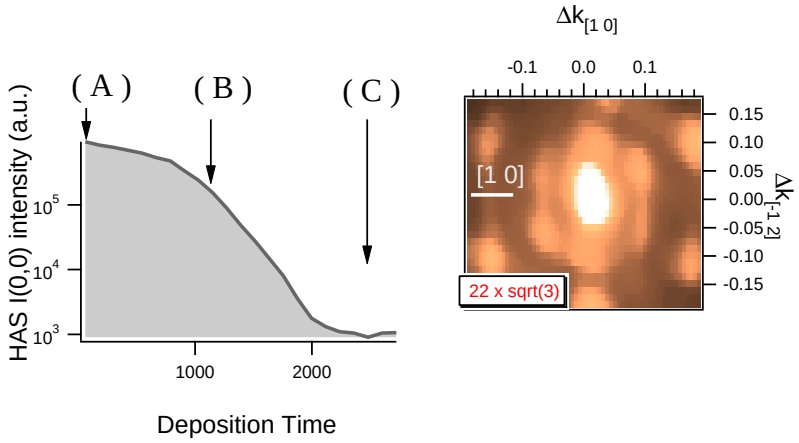

Figure 3.10: On the left, variation of the HAS specular intensity during deposition. On the right, HAS diffraction map of the clean surface at the deposition time (A) as indicated on the left graph.

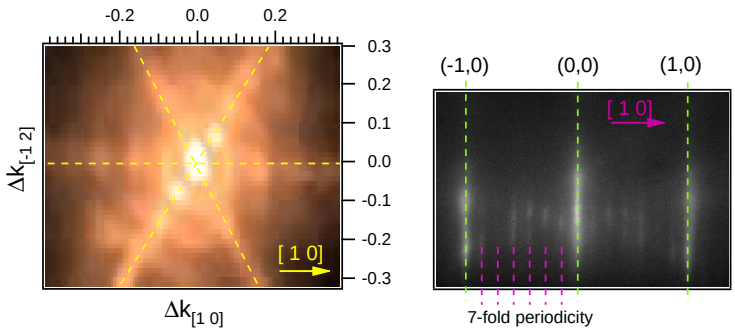

Figure 3.11: On the left, HAS diffraction map of the L-methionine film obtained at the deposition time (B) in figure 3.10. On the right, RHEED pattern for a saturated monolayer of L-methionine on Au(111).

[1 0] direction, similar to the one observed for the monolayer on Ag(111). In the following we refer to this coverage as the monolayer. Since Ag(111) and Au(111) have a similar lattice parameter, if the interaction of the molecules with the surface is small, it is not surprising that on both surfaces the film morphology is similar.

3.4.2 Film structure and morphology on Au(110).

While depositing L-methionine molecules on Au(110) at 300 K (the same temperature used for Au(111)), the HAS I(0,0) signal rapidly decreases down to the background. The first deposition stages are characterized by a reconstruction, that can equally be obtained by dosing a small amount of molecules, or by gently heating up to 400-450 K a previously deposited multilayer of L-methionine molecules.

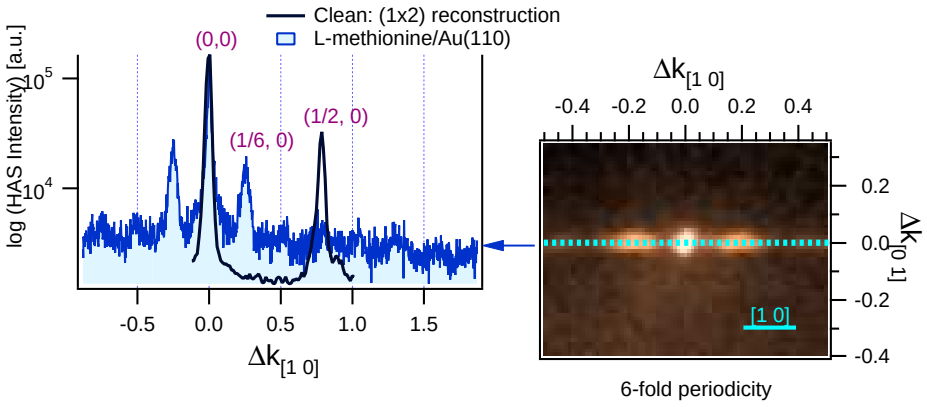

Figure 3.12: On the right, HAS 2D diffraction pattern of a submonolayer of L-methionine on Au(110). On the left, HAS diffraction spectrum along the [1 0] direction of the missing row structure (clean Au(110)) and the submonolayer of L-methionine on Au(110).

On the right of fig. 3.12 is reported the bidimensional helium diffraction map of a submonolayer of L-methionine on Au(110). (The basis set in the real and reciprocal space are defined as in figure 3.13(a) and (b), where the arrangement of atoms for the clean unreconstructed (110) surface and

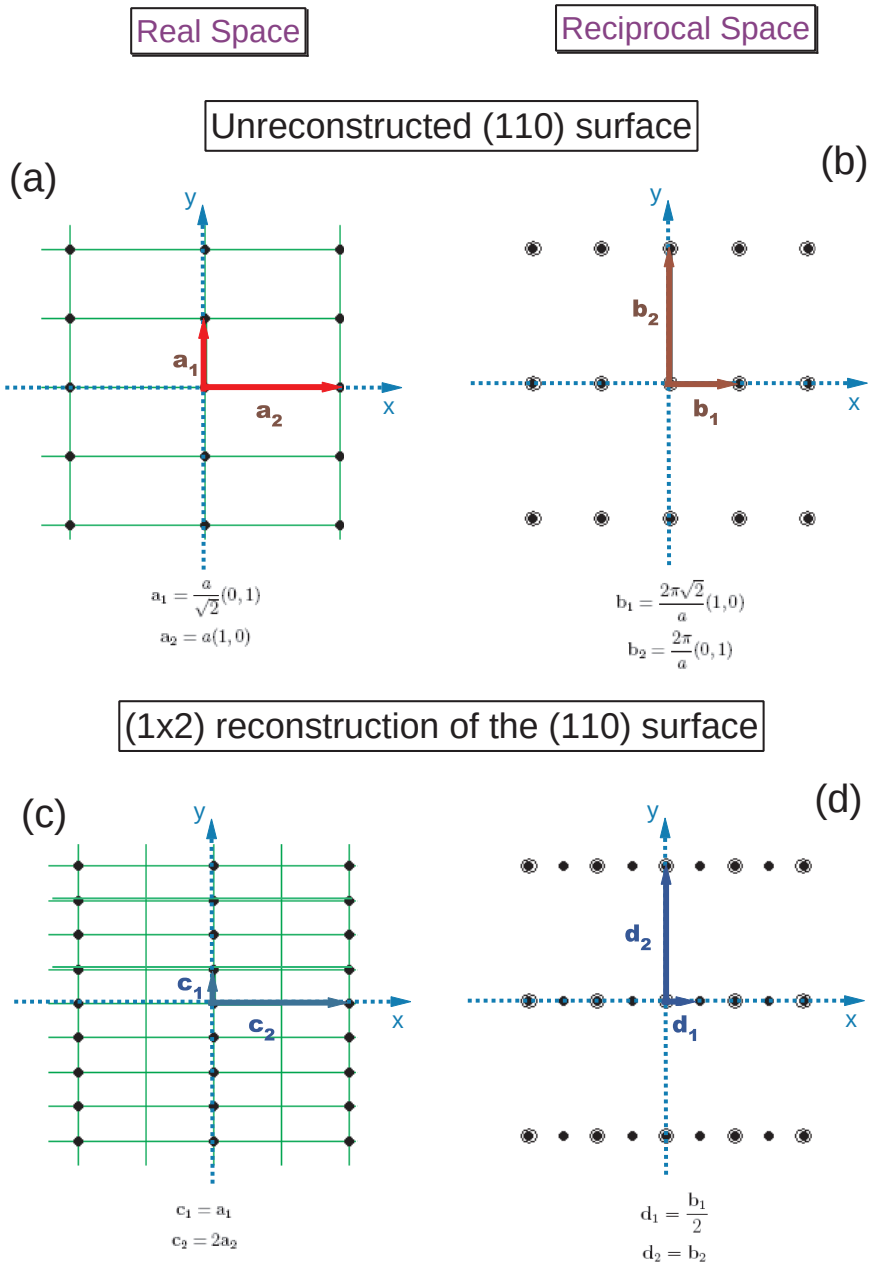

Figure 3.13: (a) Arrangement of the atoms in the unreconstructed (110) surface. (b) Pattern in the reciprocal space corresponding to the unreconstructed (110) surface. (c) and (d) real space arrangement of atoms and relative reciprocal space pattern of the (1x2) missing row reconstruction.

the relative pattern in the reciprocal space is reported. It is well known that Au(110) reconstructs forming the (1x2) missing row structure [22]. The arrangement of the atoms in the real space and the corresponding reciprocal space for the (1x2) reconstruction are reported in figure 3.13(c),(d)). In fig. 3.12(A) is shown a line profile of the bidimensional diffraction pattern along the [1 0] direction together with the one obtained along the same direction on the clean reconstructed surface. The position of the diffraction peaks for the molecular film suggest a 6-fold periodicity in the [1 0] direction.

3.4.3 Chemistry of the films.

As already described, according to the environment, the aminoacids can exist in different chemical states: the neutral (COOH-R-$CHNH_2$), ionic (COOH-R -$CHNH_3^+$), anionic (COO^--R-NH_2) and zwitterionic (COO^--R-NH_3^+) form.

The oxidation states of the molecules can be determined by looking at the N 1s and O 1s XPS spectra. The N 1s and O 1s XPS spectra for L-methionine films grown on Au(111) and Au(110) are reported in fig. 3.14. On the same figure the spectra presented in the previous section for Ag(111) are also reported. The experimental data are represented by the dotted curves, while the black lines overimposed on them are the best fits. For each fit the peaks obtained from the fitting procedure are also reported. The peak positions are summarized in the following table.

Surface	N1[eV] $\mathbf{N}H_3^+$	N2[eV] $\mathbf{N}H_2$	O1[eV] $C\mathbf{O}O^-$	O2[eV] $C\mathbf{O}OH$	O3[eV] $CO\mathbf{O}H$
Ag(111)	401.2 ± 0.1	-	531.2 ± 0.1	-	-
Au(111)	401.0 ± 0.1	-	531.0 ± 0.1	532.2 ± 0.1	533.5 ± 0.1
Au(110)	-	399.0 ± 0.1	531.2 ± 0.1	532.4 ± 0.1	533.6 ± 0.1

According to the literature values for N1s and O1s binding energies obtained for the system L-cysteine/Au(110) ([8] and references therein), N1 can be assigned to the NH_3^+ group, while N2 to the NH_2. Moreover O1 can be attributed to the oxygen atoms of the COO^- group, while O2 and O3 to the ones of the COOH group.

It is evident from the figure that the peaks show significant energy shifts for the different substrates. This can be an effect of the screening: the photoemitted electron from the molecule leaves a core behind it that induces a redistribution of the electron density inside the metal surface. This redistribution is strictly dependent on the metal surface and produce a change in the total energy of the system [23]. It is difficult to give an estimation of

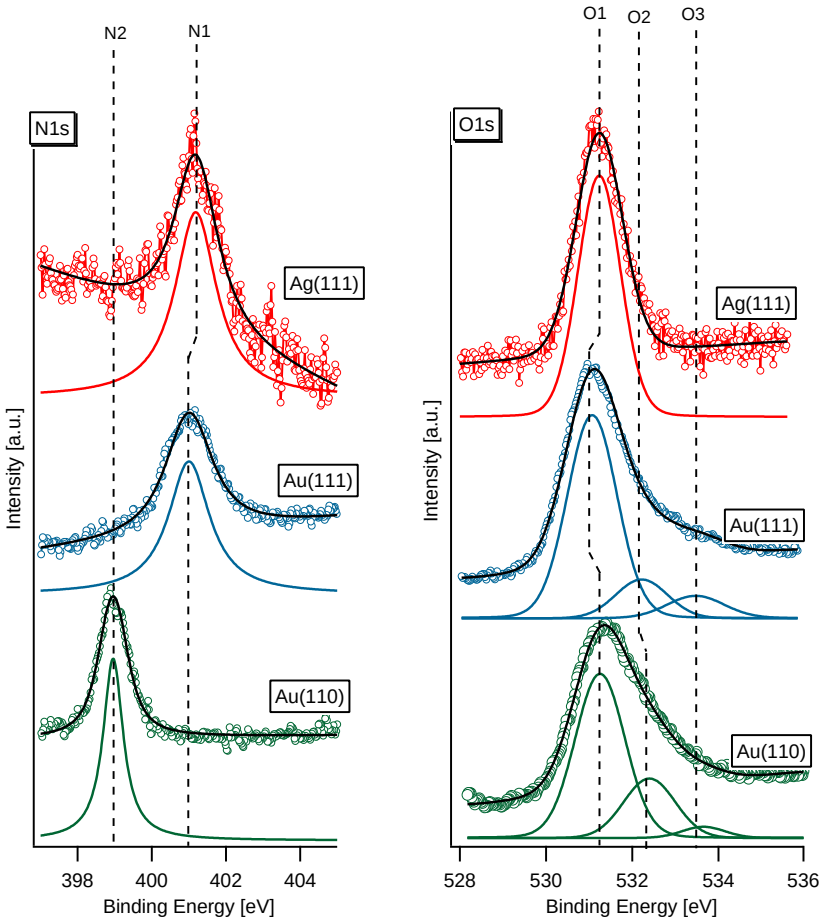

Figure 3.14: N 1s and O 1s XPS spectra for L-methionine films on Ag(111), Au(111) and Au(110). The dotted lines are the experimental data and the black lines the resulting fits. On the bottom of each spectra the peaks obtained from the best fits are also reported.

the screening, however by using the simple image charge model we can try to understand if the trend of the shifts of the binding energies between the substrates considered is consistent with our hypothesis. In this simplified model the emitted electron sees first a dipole originated by the remaining ion on the surface and a fictitious negative charge (that is an average of the charge redistribution inside the metal) located at twice the distance from the so called image plane in the surface; then the emitted electron sees a positive charge again at twice the distance from the image plane, which moves with it. Therefore the potential has the form of $-\frac{const}{z-z_0}$, where z_0 is the image plane position. The calculated values for the average image plane position reported in ref [23] are 2.07 a.u. for Ag(111), 2.18 a.u. for Au(111) and 1.74 a.u. for Au(110). The closer is the image plane to the surface, which means $z - z_0$ is smaller, larger is the potential at z, therefore larger is the screening effect. We found, in accordance with our results, that the binding energies scale in the following order from larger to smaller: Au(110), Ag(111) and Au(111). It has to be noted that the image plane position in the case of Au(110) was calculated for the missing row structure, therefore the shift can be different. It has to be taken into account that a contribution to this shifts can also be determined by the different geometries of the molecule on different surfaces, which we don't know exactly: in fact, for a certain surface (that means fixed z_0), the far is the emitting atom from the surface (that means as large is $z - z_0$), the higher is the binding energy of the electrons.

From the O1s and N1s peak positions in the table, we can conclude that L-methionine molecules on Au(111) are in the zwitterionic form, as on Ag(111). On Au(110) the molecules are neutral or anionic. According to the previous assignments, on Au(111) there are also some ionic molecules. However the O2 and O3 components in the O 1s spectra for Au(111) can be due to radiation induced damage of the molecules. We have performed careful measurements of the radiation induced damage and the evidence is that the entire XPS spectra does not show strong changes upon irradiation, a part for the oxygen peak in which the O2 and O3 components grow almost instantly (fig. 3.15). Therefore we cannot rule out the presence of damaged molecules. A second point that has to be underlined is that the FWHM of N2 (0.7 eV) is much smaller than the FWHM of N1 (1.3 eV). This can be related to two factors: the NH_3^+ group can present several geometrical configurations that determine the broadening of the peak, or the broadening can be due to charge transfer caused by the hydrogen bonding between the molecules.

A possible explanation for the different chemical states of the molecules observed on Au(110) with respect to Au(111) and Ag(111) is that the interaction of the functional groups of the molecule (amino, carboxyl and thioether) with the surface is changed. We can hypothesize that the carboxyl and/or the

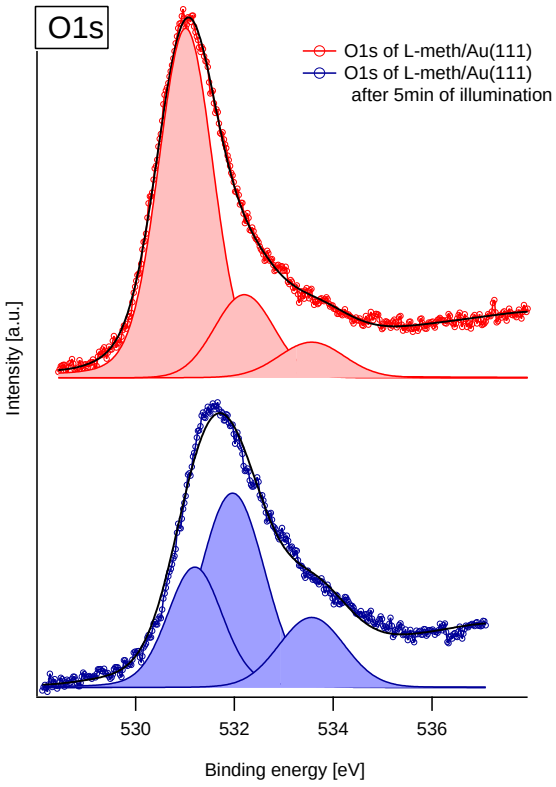

Figure 3.15: O1s XPS spectra for L-methionine films on Au(111) before and after exposure to X-rays.

amino groups bind to the surface and therefore hydrogen bonding between the molecules, that is a necessary condition to produce the nanoarrays, is inhibited. This type of bonding to the surface has been already observed for the systems of glycine and alanine on Cu(110) [14], [13]. The geometry of the entire molecule should therefore be different in the two cases and we have tried to appreciate this differences by XPS (presented in this paragraph) and NEXAFS (that will be presented in the next paragraph).

The XPS spectra of C 1s and S 2p are reported in figure 3.16 together with the fits. The peak positions are summarized in the following table. The error bars on the reported values are ±0.1 eV.

Peak	C1[eV]	C2[eV]	C3[eV]	C4[eV]	C5[eV]	C6[eV]	S[eV]
Ag(111)	285.4	285.4	285.8	286.7	288.5	-	163.6
Au(111)	285.0	285.0	285.4	286.3	287.9	289.1	163.3
Au(110)	284.7	285.1	285.3	285.9	288	288.7	163.7

The carbon C 1s spectra can be fitted with six components (C1-C6) which according to ref. [8], [24] can be assigned to the carbon atoms as indicated on the molecular model in the figure below.

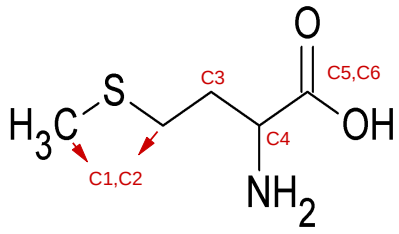

C1 and C2 are assigned to the carbons bonded to sulphur ($CH_3 - S$ and -C-S-), C3 to the carbon C-C-C, C4 to the carbon bonded to the amino group (-C-NH_2) and C5 and C6 to the carboxyl group (-COOH).

The C 1s spectra for L-methionine molecules on Ag(111) and Au(111) are identical, but just shifted according to the screening hypothesis.This is a confirmation that on this surfaces the molecules adopt the same geometrical conformation. However for Au(110) there are strong changes for all the carbon components, suggesting that the molecule adsorbs as a different conformer. The strongest changes are present for the C-S and C-N components. A possible explanation, which we will examine better in the next paragraph, is that the molecule binds to the surface via both the lone pairs on the sulphur and the nitrogen. Even the -COOH component exhibits a shift but in

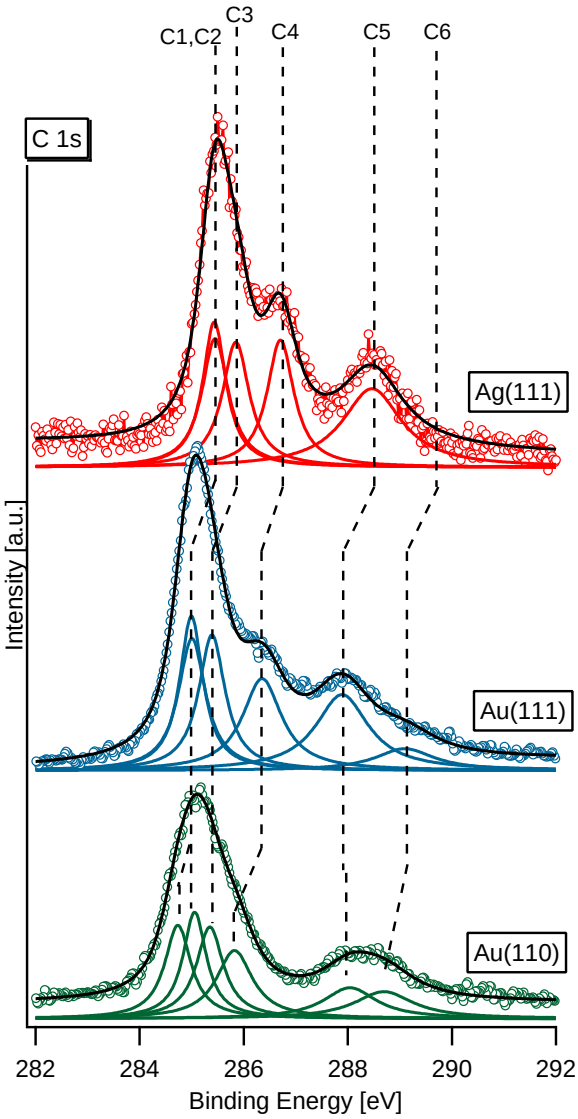

Figure 3.16: C1s XPS spectra for L-methionine films on Ag(111), Au(111) and Au(110). The dotted lines are the experimental data and the black lines the resulting best fits. On the bottom of each spectra the peaks obtained from the best fits are also reported.

the following section we will exclude the possibility of binding to the surface. The S 2p spectra can be fitted with a single doublet which shifts following the trend of the image plane positions. However, as we have observed previously, the distance of the S atom from the surface can be different for the surfaces considered. In order to better understand the bonding scheme we have performed NEXAFS measurements described in the following paragraph.

3.4.4 Bonding scheme: NEXAFS results.

The NEXAFS technique allows the determination of the electronic structure and orientation of the molecules adsorbed on surfaces [20], as briefly described in chapter 2. In general it is possible to correlate specific NEXAFS features with molecular functional groups and, in some cases, individual bonds in such a way that the total spectrum can be considered as a combination of elementary spectra. This is the so called building block principle. However before using this procedure it should be noted that it presents some limitations: the delocalization of the electronic charge across multiple functional groups leads to new molecular orbitals combining the properties of the conjugated groups. In such cases the NEXAFS features of the individual groups can be modified significantly and new features may appear.

The analysis of the NEXAFS spectra usually is not trivial. Since they are composed of a large number of features, before comparing their differences in the monolayers grown on different surfaces, it is needed to recognize them according to the literature within the building block picture. Therefore we started the analysis by considering the NEXAFS spectra of a multilayer of L-methionine molecules that has to be compared with NEXAFS measurements for solid L-methionine [25]. The molecules in the multilayer are in the zwitterionic form as the ones composing L-methionine crystals. In fig. 3.17 the Carbon K-edge NEXAFS for a multilayer of L-methionine is reported. The experimental data are represented by the dotted line, while the solid line is the best fit. In the lower part of the figure the peaks obtained from the best fits are also reported.

The fit was performed by using a single step function representing the ionization edge (IP), even if since from XPS there are different carbon C 1s initial levels, and thus there should be several ionization edges. According to [26] the edge used is the lowest in energy, therefore the analysis for the first peaks is not affected. Even the analysis for the high energy part of the spectra will not be greatly influenced since it contains broad features. In the table reported on the figure the peak positions are summarized. According to [25] and [26] we can attribute P1 and P2 to transitions to $\sigma^{\star}$(C-S) states, more precisely P1 to the -C-S- bond and P2 to the -S-CH_3. The narrow resonance

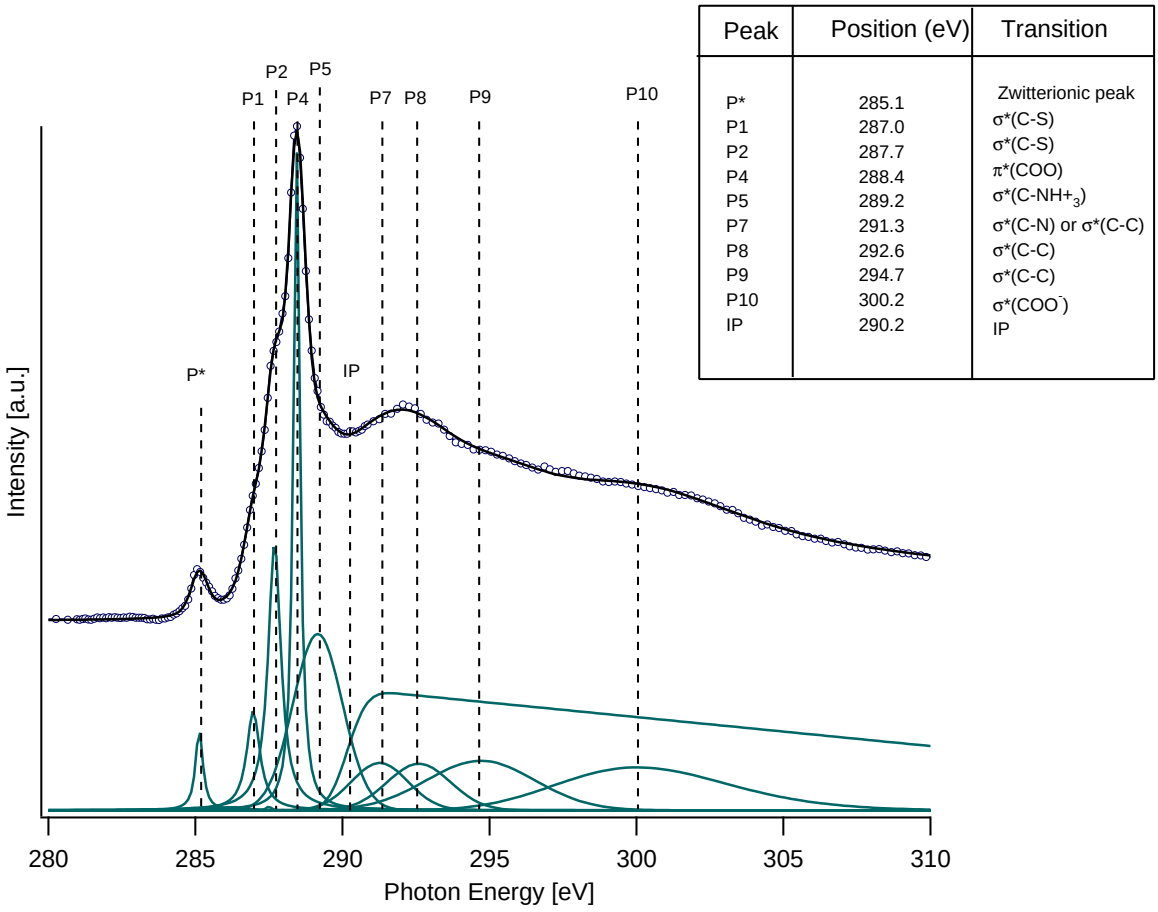

Figure 3.17: Carbon K-edge NEXAFS of an L-methionine multilayer. The dotted lines are the experimental data while the solid black line is the fitting curve. In the bottom part of the figure the peaks obtained from the best fit are also reported.

P4 can be attributed to the $\pi^\star$(COO) transition. P5 is related to the $\sigma^\star$(C-NH_3^+) transition. P7 can be attributed to $\sigma^\star$(C-N) but it can also contain contributions from $\sigma^\star$(C-C) transitions. P8 and P9 are usually assigned to $\sigma^\star$(C-C) transitions, while P10 to the $\sigma^\star$-shaped resonance stemming from the carboxyl group in the deprotonated form (COO^-). There is a strong debate in literature about the assignment of the resonance $P^\star$. Cooper et al. [27] for glycine in the gas phase do not see this resonance, while Zubavichus et al. [28] observed it together with a resonance at 287.5 eV for glycine solid samples measured in partial yield mode. Since it was not visible for samples measured in transmission mode, they assigned it to minor contaminations present on the surface of glycine particles or products of irradiation induced damage of glycine. However the same authors in different works ([29] and [25]) attribute these spectral features to a minor contribution of charge of the aminic carbon and nitrogen atoms to the carboxylate π-system of the glycine molecule. The same conclusion was obtained by several authors [30], [31], [15] for other aminoacids in the solid state or deposited on surfaces. As we will see later we do not observe this feature on the monolayer spectra, therefore we can exclude that its origin is a contamination and we rather think that it is due to the delocalized state.

At this point we have identified the Carbon K-edge NEXAFS resonances of the L-methionine and we can compare their behavior when 1ML is deposited on Ag(111) and Au(110). Unfortunately it was not possible to measure the Carbon K-edge NEXAFS on Au(111), but since the morphology and the chemistry of the resulting film from HAS measurements and from XPS is identical to Ag(111), we can assume that the geometry of the molecule bonded to the surface is the same for both substrates.
In fig. 3.19 the Carbon K-edge NEXAFS measurements for 1ML of methionine on Ag(111) and Au(111) are reported. The measurements were performed for two orientations of the surface with respect to the polarization vector of the light: parallel and perpendicular. The geometrical orientation of the sample and the angles that will be used in the following are defined in figure 3.18. This allows us to understand the angle of the bonds with respect to the surface plane as described in chapter 2.

The fitting is performed by using the same peaks found in the multilayer, plus some new resonances indicated in green on the figure. The NEXAFS in the two polarizations for the same sample were fitted by keeping the width and the position of the peaks fixed. The final positions are reported in the tables on the figure. We note that:

1. the main difference between L-methionine molecules on Ag(111) and Au(110) is the oxidation state of the amino group. P5 was attributed in

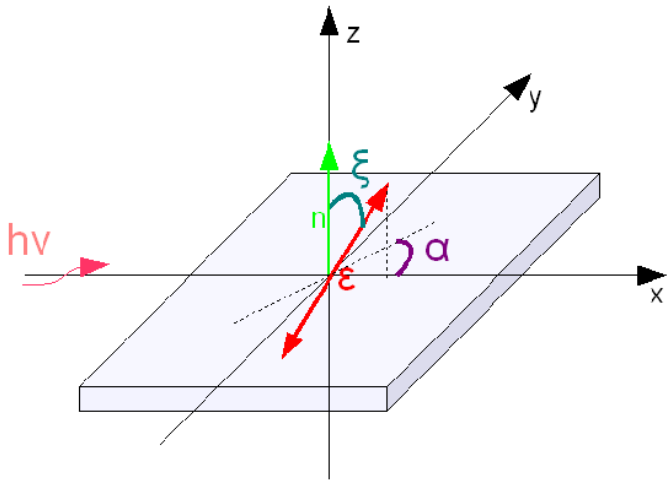

Figure 3.18: Orientation of the sample with respect to the light polarization vector ϵ: the relevant angles are defined.

the multilayer case to $\sigma^\star$(C-NH_3^+) states. In the monolayer on Ag(111), which presents zwitterionic molecules, it is found in the same energy position, while in the layer on Au(110) it is shifted to lower photon energy. The direction of the shift is consistent with the fact that the initial state N 1s is also shifted to lower binding energy, as already explained. However P5 on Au(110) is found at a lower photon energy with respect to the gas phase measurements [32], which can be due to its interaction with the surface. In the spectra on Au(110) there is also another new feature in that spectral region, labeled P6. However it is difficult to discuss its intensity variation since it is too close to the edge.

2. $P^{\star\star}$ is a new resonance, that was not present before. We can attribute it to new states originated from the interaction with the surface. Its intensity for L-methionine on Ag(111) does not vary in the two polarizations, while on Au(110) there is a clear dichroism. Its behavior is similar to the one of peak P5.

3. P3, according to [26] [14], can be associated to a transition from the -C-C-C- chain to a $\sigma^\star$(CH). It is found on both surfaces at the same photon energy and shows a strong dicroism.

4. P4 is found at the same position for both the surfaces. It was observed

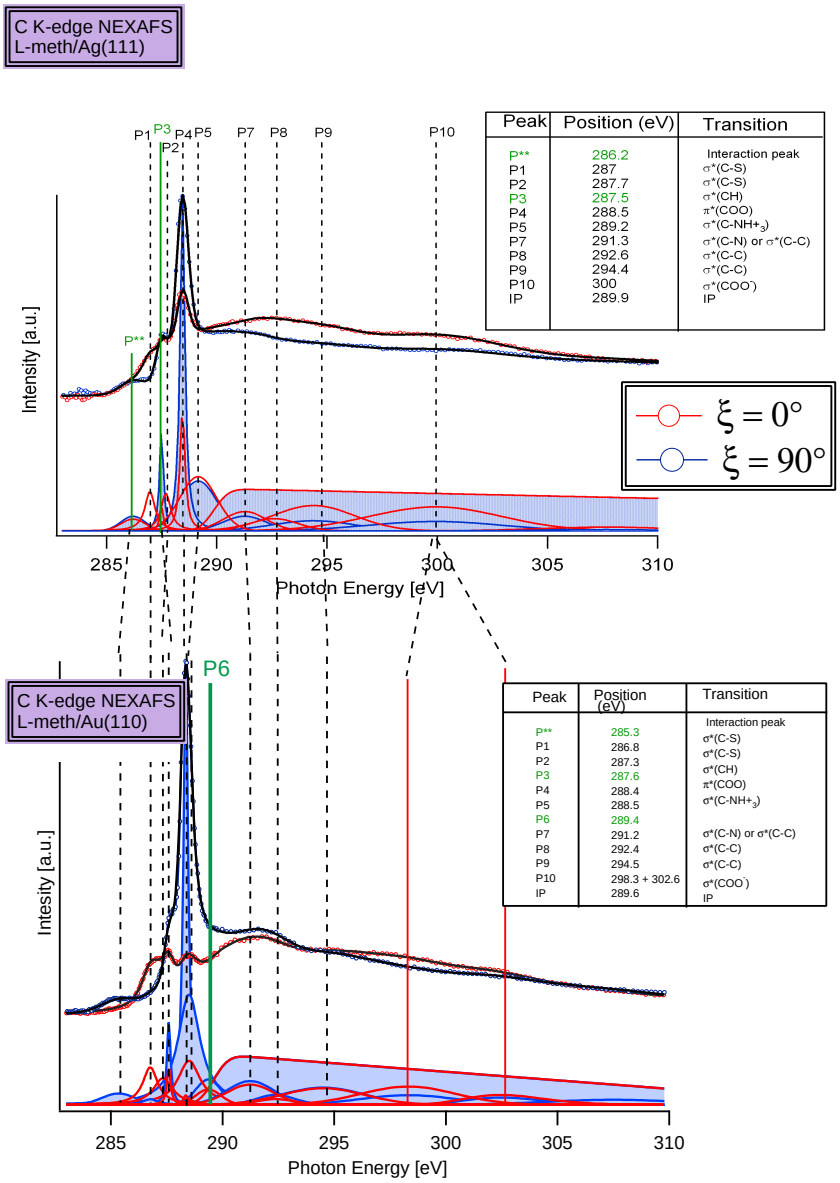

Figure 3.19: Carbon K-edge NEXAFS measurements for L-methionine films on Ag(111) (top graph) and Au(110) (bottom graph). For each surface the spectra are acquired for the light polarization parallel to the surface (red) and perpendicular to the surface (blue).

in literature that its position will not change when the carboxyl group is protonated [26]. The -COO^- plane is flat on Au(110), while it is tilted on Ag(111) with respect to the surface.

5. P1 and P2 in the Ag(111) case are zero when the light polarization is perpendicular to the surface, which means that C-S-C is flat on the surface. On Au(110) there is a small contribution from P1. P1 was associated to the -C-S- bond, therefore this can be an indication of a slightly different geometry of the molecule. P2 on Au(110) shifts to lower photon energy with respect to P3. This can also be due to the stronger interaction in this case of the sulphur lone pair, but we have seen this shift also in the C1 component of the C1s XPS.

6. P10 on Au(110) splits in two components. This is due to the fact that on the surface are present protonated and deprotonated carboxyl groups at the same time.

Peak P5 on Au(110) is very close to P4 and it can be seen as an asymmetry of P4. In order to clarify that it is a separate peak, we have studied the azimuthal dependence of the resonances. This means that with the polarization of the light parallel to the surface ($\xi = 90$ in Fig.3.18) we measure the NEXAFS spectra by rotating the surface by α (as indicated in figure). α is the azimuthal angle and is measured with respect to an high symmetry direction of the surface. In such a way we can determine the orientation of the bonds in the surface plane. In figure 3.20 the C K-edge NEXAFS spectra of L-methionine monolayer on Au(110) for different azimuthal angles are reported. The fits are performed by keeping fixed the positions and the widths of the peaks previously identified.

In this sequence of spectra the existence of Peak P5 is clear. However by looking at the intensity variations for each peak as a function of α (reported in fig 3.21) we can observe that:

- C-S and -C-S- comprise an angle of about 150° since the maxima of P1 and P2 are separated by 30°;

- the -COOH plane has a preferential orientation on the surface as indicated by the intensity variation of P4, that is similar to P11. P11 is usually associated to sigma states of deprotonated carboxyl group. P10 belongs to the protonated one and presents a completely different behavior;

- P7 was previously attributed to $\sigma^\star$ (C-N) or (C-C) states, and indeed presents an azimuthal variation similar to P5, which belongs to states

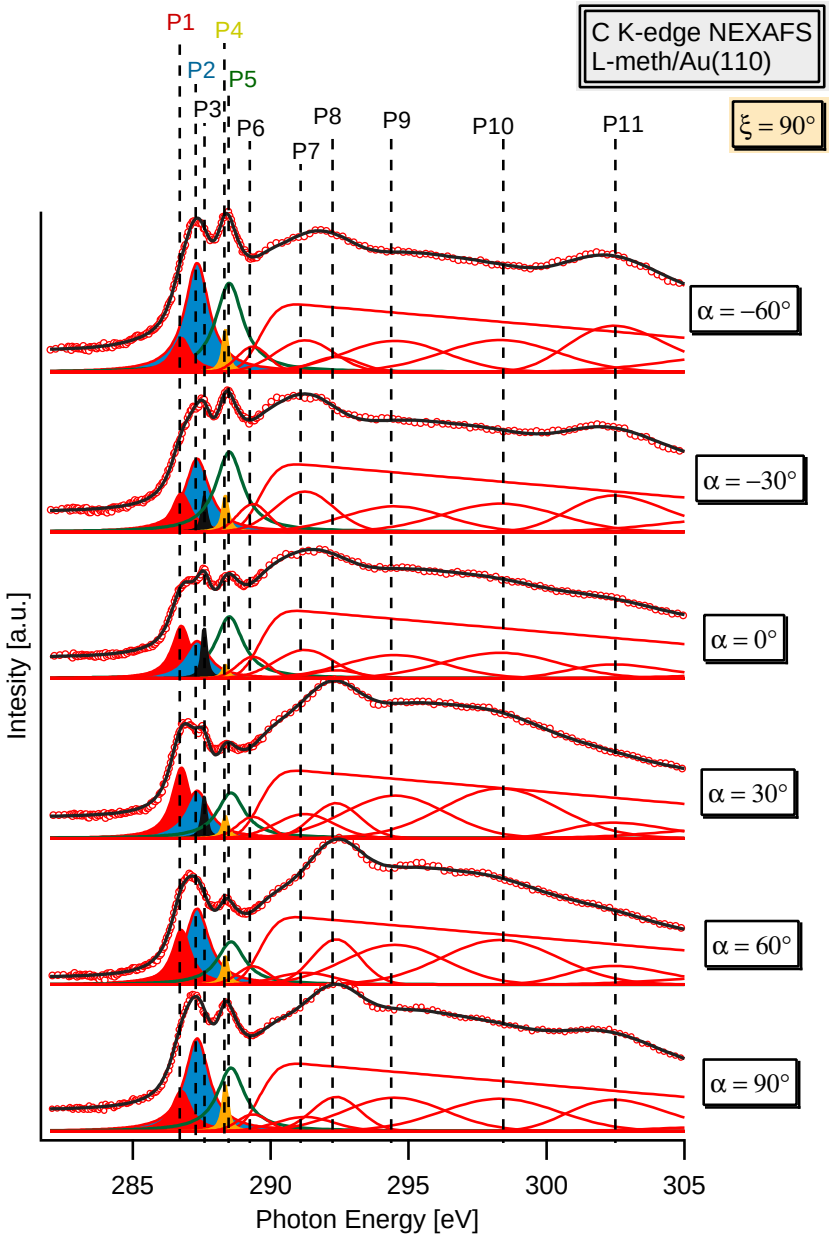

Figure 3.20: Carbon K-edge NEXAFS measurements for L-methionine films on Au(110) for different azimuthal orientations of the light with respect to the surface symmetry directions. For $\alpha = 0°$ the light polarization is parallel to the [0 0 1] substrate direction.

involving the carbon bounded to the nitrogen. However we cannot exclude contributions from C-C, also because this resonance is very broad.

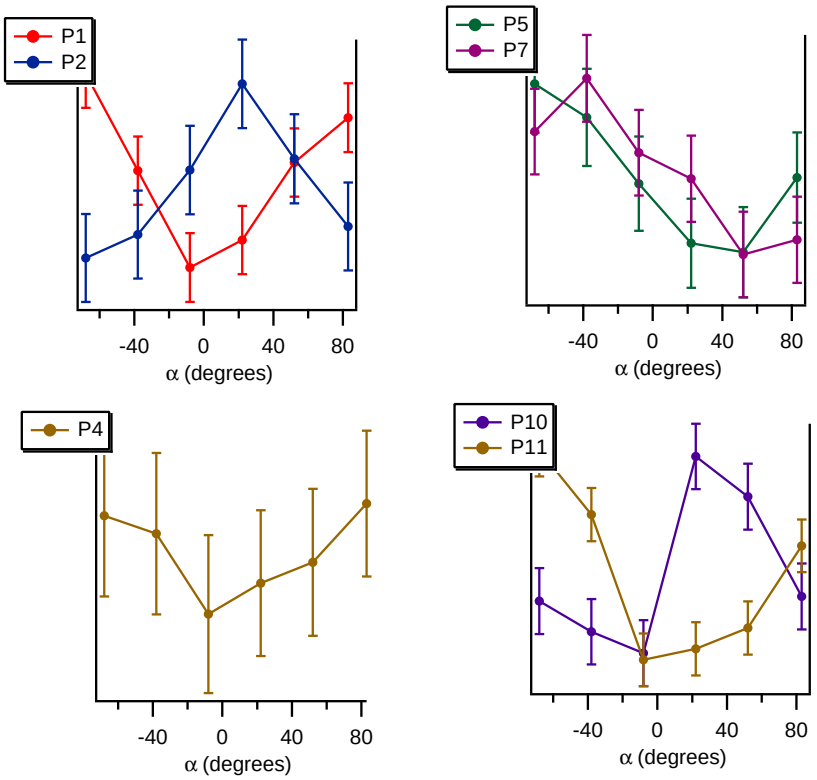

Figure 3.21: Intensity of selected peaks of the fit as a function of the azimuthal angle.

By means of the Carbon K-edge NEXAFS we have determined the orientation of the functional groups with respect to the surface. In this paragraph we will concentrate our attention on the Nitrogen K-edge NEXAFS. In the case of 1ML of L-methionine adsorbed on Au(111) the nitrogen K-edge NEXAFS shows a broad peak at 406 eV (fig. 3.22), characteristic of zwitterionic aminoacids ($-NH_3^+$) [33]. There are also other small features in the low energy part of the spectrum, probably due to radiation induced damage, since they grow with the exposure time to the beam. In the case of L-methionine adsorbed on Au(110) the amino group is in the $-NH_2$ form. The nitrogen K-edge NEXAFS spectrum in this case shows a low energy band located at 403 eV as previously observed in literature [34], but there are also some features

at 400 eV. We can exclude that they are due to radiation induced damage, since we have taken careful measurements by moving the sample and thus exposing fresh parts of the surface to the beam. These states also show a dependence with the polarization angle, which reveals that they are oriented normal with respect to the surface. This new states can be due to the amino group interacting with the surface. An interesting point is that they match well the polar dependence of peak $P^{\star\star}$ of the Carbon K-edge NEXAFS.

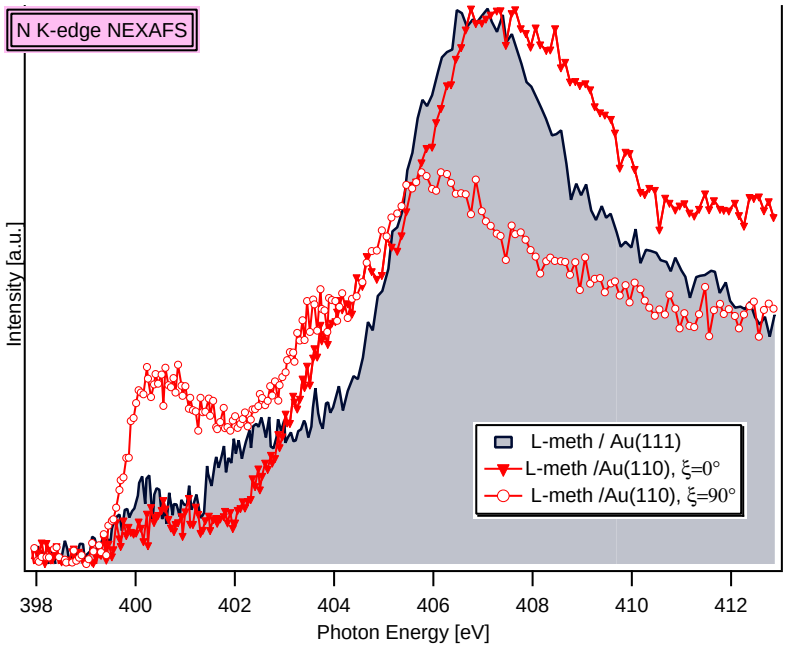

Figure 3.22: Nitrogen K-edge NEXAFS. The black line is the Nitrogen K-edge NEXAFS spectrum of a L-methionine monolayer on Au(111). The red lines are the Nitrogen K-edge NEXAFS spectra of a L-methionine layer on Au(110) for two orientations of the light polarization with respect to the surface.

3.4.5 Discussion.

The following model for molecular adsorption can be adopted: on all the substrates the -S-CH_3 bond assumes the same configuration parallel to the surface. The -C-S- in the Ag(111) and Au(111) case is also flat, while on Au(110) is slightly tilted presumably because the molecule is adsorbing as a different conformer or it is interacting stronger. It was shown by STM break junction measurements and theoretical calculations that the -NH_2 and

the C-S-C groups can bind to Au: the lone pair of electrons on the nitrogen and sulphur respectively can bind the Au atoms, and the bonding is stronger with undercoordinated gold atoms [11], [12]. The interaction of the nitrogen lone pair with Au surfaces will be studied in the next chapter of this theses. The molecule-substrate bonding via the lone pair is in competition with the molecule-molecule hydrogen bonding. On Ag(111) and Au(111) (that have few undercoordinated atoms with respect to the (110) surface) hydrogen bonding is favored, and therefore the molecules are free to move on the surface and form zwitterionic dimers. On Au(110) the molecules bind stronger to the surface via the sulphur lone pair and the nitrogen lone pair. Since the amino group is involved in binding, the molecules cannot form hydrogen bonds between -NH_2 and -COOH to form zwitterionic dimers. We can exclude bonding with the carboxyl group, since from the NEXAFS measurements it is parallel to the surface.

The fact that the molecule will adsorb in different conformers depending on the type of interaction with the surface is not surprising and was already observed for other aminoacids. Jones et al [15] for alanine on Cu(110) found a variety of chiral and achiral surface superstructures determined by different molecular conformers with the adsorption geometry where the O atoms of the carboxylate group and the N of the amine group are approximately atop Cu atoms. The same situation was observed even for glycine on Cu(110) [13], [14].

The conclusion is that the surface geometrical structure and electronics determines the chemical groups binding to the substrate, therefore selects the geometry of the conformer and the final chemical state of the molecule adsorbed.

3.5 L-methionine on Cu(111)

In this section the self-assembly of L-methionine molecules on Cu(111) surfaces will be presented. It will be shown that the oxidation state of the amino acid molecules and the morphology of the supramolecular structures formed strongly depend on the substrate temperature. The substrate temperature during deposition changes the chemical state of the adsorbed molecules, therefore the binding geometry to the substrate is modified and consequently the general structure of the film is changed.

This work has been performed in collaboration with the group of prof. Barth (TU München, Physik Department). The STM images presented in this section were performed at UBC (Canada) by A. Schiffrin.

3.5.1 Film structure and morphology on Cu(111).

The morphology of self-assembled L-methionine films grown by thermal evaporation on Cu(111) was studied by means of Helium Atom Scattering and Scanning Tunneling Microscopy. We have already mentioned that as in the case of Ag(111) and Au(111) the molecules assemble in linear structures, but the morphology of the supramolecular assemblies strongly depends on the substrate temperature during molecular deposition.

If the deposition is performed at temperatures below 250 K, the 2D-HAS diffraction maps exhibit an hexagonal diffraction pattern (top image of fig. 3.23). For experimental convenience the two Cartesian axis have Δk_x rotated by 10° with respect to the [0 -1] reciprocal direction). The diffraction peaks are broad (average width of 0.14 AA^{-1}) and are rotated by 10° clockwise with respect to the high-symmetry directions of the Cu(111) substrate. The surface presents a partial long range order. We call this phase low temperature LT-phase. The STM measurements performed on similar samples show in fact that at 240 K the molecules nucleate into small stick-like clusters with partial linear ordering, as reported in the bottom image of figure 3.23. These formations grow following a 10° clockwise tilt with respect to the high-symmetry axis of the underlying lattice.

If the samples in the LT-phase are gently heated up to 320-340 K, the diffraction features become better defined and the diffraction hexagon rotates by 20 degrees counterclockwise: the 2D-diffraction map in figure 3.24 (top image) is obtained after heating the sample of the LT-phase up to 320 K. In the second graph of fig. 3.24 the rotation of the hexagonal diffraction pattern is followed by looking at the evolution during a flash of the LT phase up to 320 K of the diffraction peaks corresponding to a section of the 2D-map at $\Delta k_y = -0.2$ Å^{-1} (indicated by the red line A on the 2D-maps for the LT- and

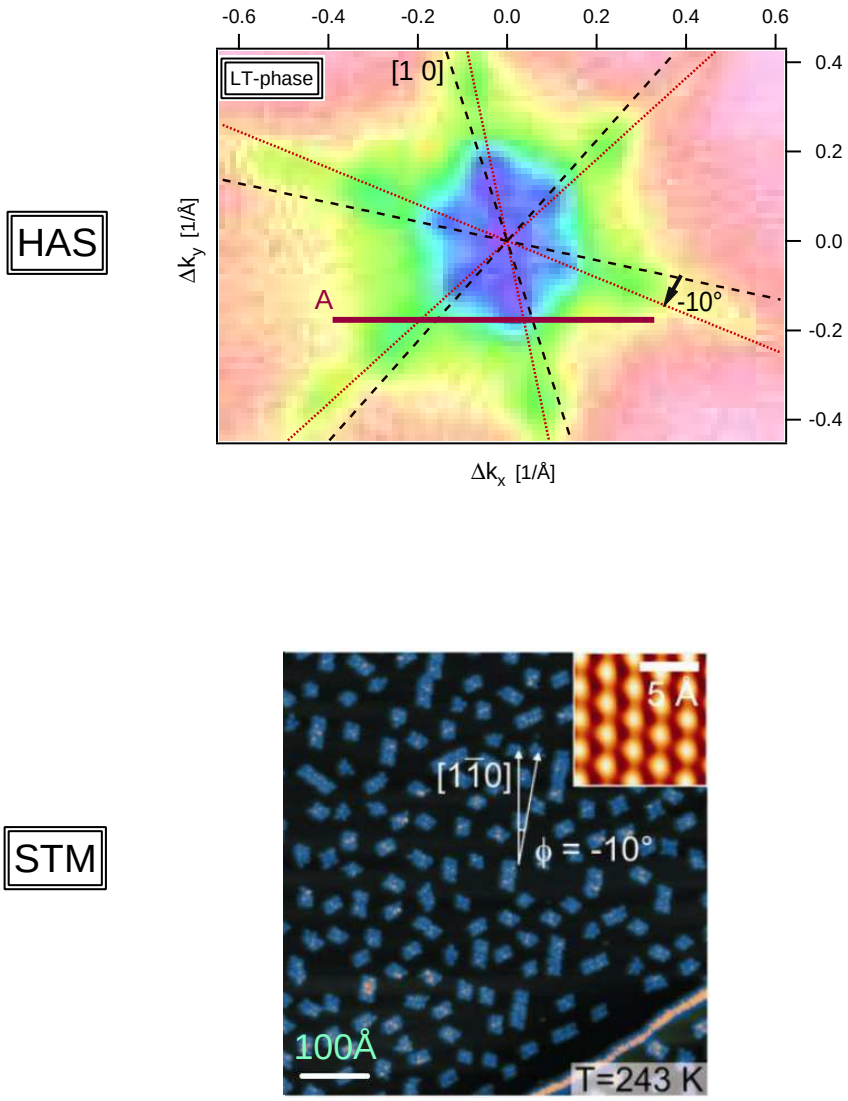

Figure 3.23: Top image: HAS diffraction map of the L-methionine submonolayer formed by deposition at 250 K. The hexagonal pattern presents diffuse features rotated by 10° with respect to the $< 10 >$ orientations (indicated by the black dashed lines). The lattice basis sets are defined as in figure 3.5. Bottom image: STM measurement of a L-methionine submonolayer deposited on Cu(111) at T=240 K ($I = 0.1nA, U = -100mV$). Scale bar: 100Å. The crystal direction $[1 - 10]$ corresponds to [1 0] with our basis set. Inset: atomic resolution of the Cu(111) substrate.

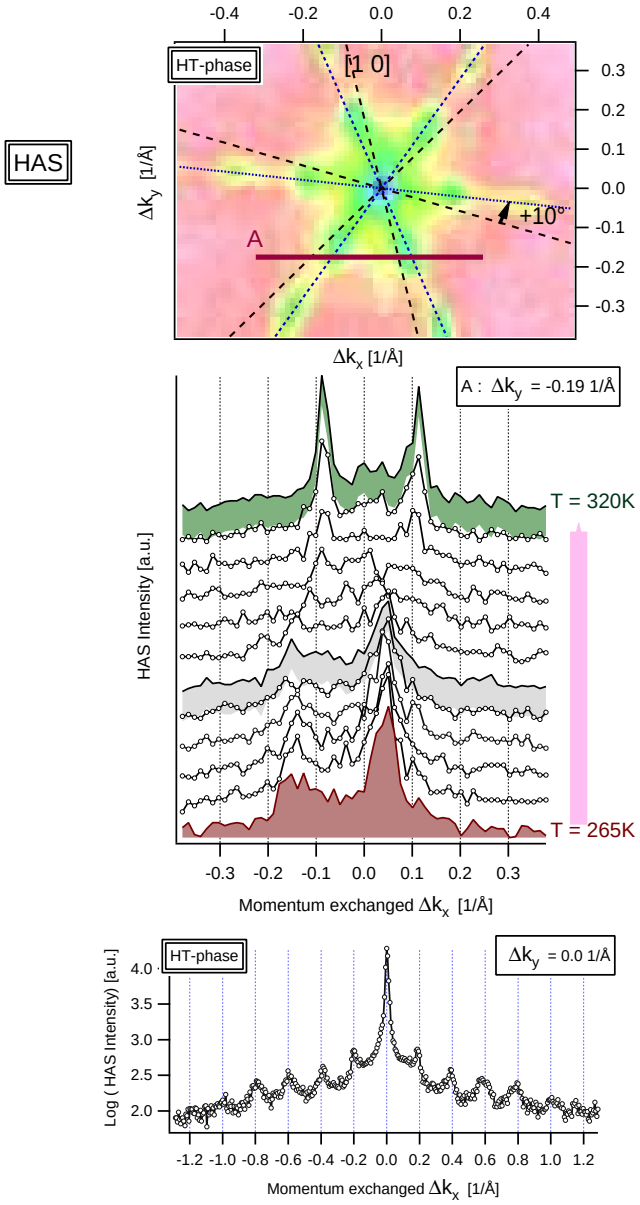

Figure 3.24: Top image: HAS diffraction map of the L-methionine submonolayer formed by deposition at 250 K and flash up to 320 K (HT-phase). The hexagonal pattern presents peaks rotated by $-10°$ with respect to the $< 10 >$ orientations (indicated by the black dashed lines). Central graph: HAS diffraction spectra along the direction indicated by the red line in the top image ($\Delta k_y = -0.20 \text{Å}^{-1}$) for substrate temperatures from 265 K to 317 K . Bottom graph: HAS diffraction spectrum of the (HT-phase) along the direction $[[10]+10°]$. The molecules arrange in periodic structures with average period of 33Å (calculated from the positions of the diffracted peaks).

HT-phases). The change in the width of the diffraction peaks is an indication of an increased size of the domains contributing to the long range order: the small clusters, as seen in the STM images in fig. 3.25, form long chains. The diffraction pattern in the bottom graph of fig. 3.24 is a section of the 2D-diffraction map for the HT-phase along the diffraction peaks direction: the peaks are spaced by 0.19 Å^{-1}, which corresponds to 33 Å periodicity perpendicular to the chain direction. We call this phase high temperature HT-phase.

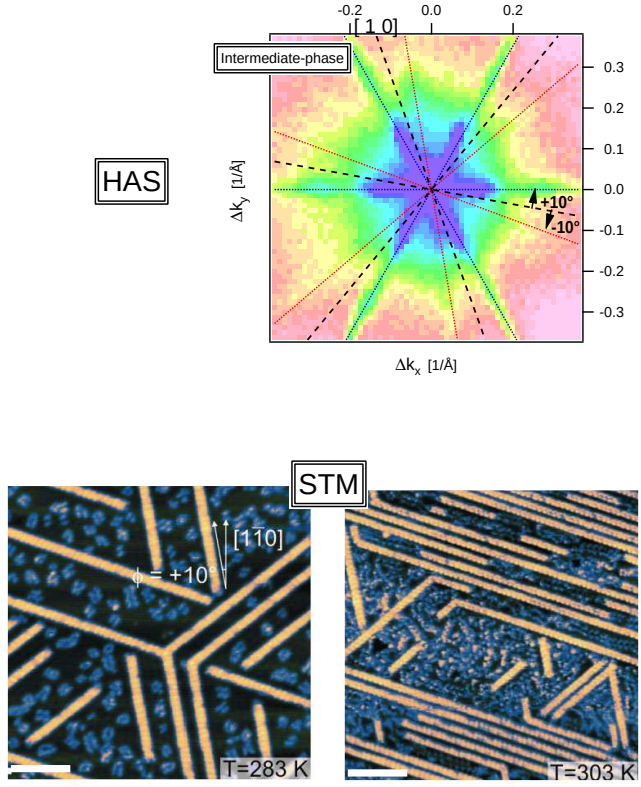

Figure 3.25: Top image: HAS diffraction map of the L-methionine submonolayer formed by deposition at 300 K. LT-phase (with directions identified by the red dashed lines) and HT-phase (with directions identified by the blue dashed lines) coexists. The black dashed lines identify the $< 10 >$ orientations. Bottom images: STM measurements after L-methionine depositions on Cu(111) at $T = 280K (I = 0.1nA, U = -100mV)$ and $T = 300K$ $(I = 0.06nA, U = -100mV)$. Scale bar: $100\dot{A}$.

The deposition at substrate temperatures greater than 250K is characterized in the bidimensional HAS diffraction maps by the coexistence of two diffraction patterns, that means of both HT and LT phases (fig. 3.25). The corresponding STM images, shown in fig. 3.25, present the formation of one-dimensional arrays with long-range order which we associated to the HT phase. Their orientation is shifted of 10 degrees counter-clockwise relative to the high-symmetry axis of the substrate. Both phases coexist in a given temperature range, indicating a non trivial transition process between both entities. However the ratio between the two phases is highly temperature dependent: at a higher temperature, the well-ordered linear pattern prevails.

This thermally activated orientational switch represents an eniantiomorphic reordering of the system and must be related to the chiral signature of the molecular building units. In the following paragraph we will see that it is driven by the change in the chemical state of the amino acid molecules.

3.5.2 Chemistry of the films.

The chemical state (or oxidation state) of L-methionine molecules in the LT- and HT-phases can be determined by means of X-ray photoemission spectroscopy (XPS), as already explained in the previous sections.

On both phases the O 1s XPS spectrum (not shown) presents a single component with binding energy at about 531.3 ± 0.1 eV. It can be attributed to the oxygens in the deprotonated carboxyl group -COO^-. Therefore both phases (LT and HT) comprise L-methionine molecules with a deprotonated carboxyl group.

The N1s XPS spectra are shown in figure 3.26. The two phases are clearly different:

- in the LT-phase (red trace) the N 1s spectrum shows two distinct peaks that can be fitted as two components, N1 and N2, at binding energies $E_{N1} = 399.5 \pm 0.1$ eV and $E_{N2} = 401.5 \pm 0.1$ eV. According to the previous section, N1 can be associated to nitrogens in the -NH_2 form, while N2 to the ones in the -NH_3^+ form. By combining these information with the ones about the carboxyl group, we can conclude that the LT-phase comprises therefore molecules in the anionic ($NH_2 - R - COO^-$; $R = CH_3SCH_2CH_2CH$) and zwitterionic ($NH_3^+ - R - COO^-$) form.

  We have controlled by means of fast XPS data acquisition (parallel acquisition, 200 channels) with 1s time resolution that the anionic component of the LT phase is intrinsic to the supramolecular assembly and not an artifact due to beam exposure. We have then studied whether the ratio between the zwitterionic and anionic molecules changes with

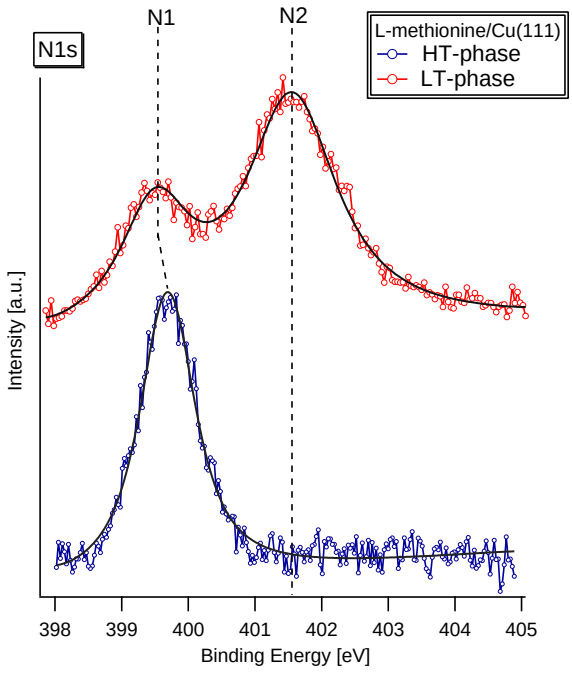

Figure 3.26: N1s XPS spectra of L-methionine on Cu(111) for the low (red) and high (blue) temperature phases. The dotted lines are the experimental data, while the black solid lines are the fitting curve.

coverage. The inset in Fig. 3.27 (a) represents the ratio r between the areas of the Voigt curves fitting N2 and N1 respectively, depending on the molecular coverage θ. The depositions are performed at low temperatures. The molecular coverage was obtained from the overall XPS N 1s intensity combined with the HAS specular measurements during L-methionine deposition: the relative molecular coverage is estimated from the total N1s integrated intensity, whereas the attenuation of HAS specular intensity monitors the portion of L-methionine covered Cu substrate. Complete disappearance of HAS specular intensity is assigned to a saturated molecular layer (i.e. $\theta = 1$ML). It becomes clear that there is an increasing trend of r with respect to θ, meaning that there is an increase of the zwitterionic species with coverage. Morphologycally, it has been observed in the STM data that the molecules, having enough thermal energy to diffuse at the deposition temperature (for high as well as for the low temperature cases), bind first to the substrate step edges, where the Cu atoms are less coordinated and therefore their interaction with the biomolecules is stronger. This indicates that the aminoacid molecules bound to the substrate step-edges are in the anionic form and are related to the XPS N1 peak. Once there are enough species to saturate the step-edges, the zwitterionic chain emerge. The intensity of the N2 XPS peak (attributed to zwitterionic molecules) increases once the molecules have decorated the step edges. The STM image of figure 3.27 (c) shows the decoration of the step edges by the molecules for the low temperature case, indicated by the white arrows. This hypothesis is corroborated in the XPS N1s spectrum of figure 3.27 (b), where a substrate with higher density of step edges was considered for the low temperature molecule deposition.

Such a rough surface was obtained by Ar+ sputtering at 0.3 keV after the usual cleaning procedure of the sample. The reduced surface order was monitored by HAS specular reflectivity as well as specular width. Here the amino group N1 (attributed to -NH_2) clearly prevails, revealing that zwitterionic L-methionine species dominate over anionic ones only for a high order Cu(111) substrate, i.e., a substrate presenting large flat (111) terraces and low step-edge density.

- in the HT-phase (blue trace of fig. 3.26) the N 1s peak can be fitted with one component at $E_{N1} = 399.7 \pm 0.1$ eV. It can be attributed to the nitrogens in the neutral amino group ($-NH_2$). The position of this peak is shifted between the two phases by 0.2 eV. This shift can be explained in terms of the coordination of the surface atoms on the steps and on the flat terraces on which the binding energy could be

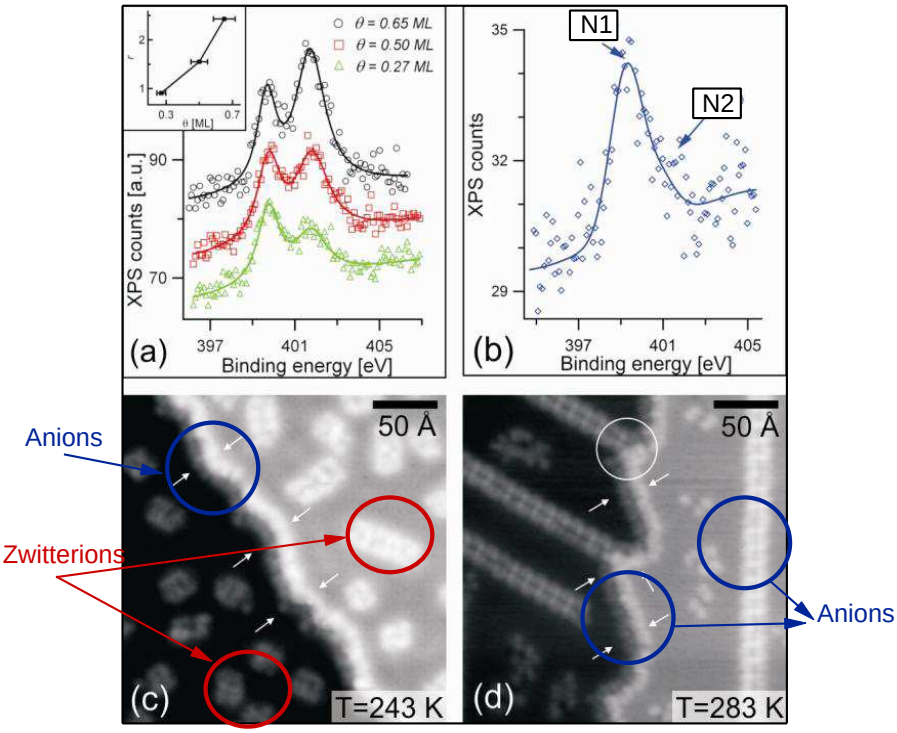

Figure 3.27: (a) N1s XPS spectra for the LT phase at three different coverages. Inset: ratio r between the area of the Voigt curves for peaks N1 and N2 as a function of the coverage θ. The relative intensity of the N2 component increases with molecular coverage. (b) N 1s XPS spectrum for a high step-edge density surface. The N1 component prevails. (c) STM topographical image (I=0.1 nA, U=-200 mV) of the low temperature phase prepared at 243 K. L-methionine molecules are bound to the step-edges (white arrows). (d) STM topographical image (I=0.1 nA, U=-500 mV) of the high temperature phase prepared at 283 K: the step-edges are perturbed by the bonded molecular species (white arrows) and the nucleation of the ordered molecular phase is linked to the low coordinated adsorption sites (white circle).

different. The molecules in the HT-phase are therefore anionic.

In conclusion, the molecules on flat Cu(111) terraces for samples grown at low temperatures are in the zwitterionic form, while for high temperatures they are in the anionic form. Moreover on flat Cu(111) terraces the deprotonation of the ammonium group takes place between 280 and 300 K (in the transition from the LT-phase to the HT-phase), whereas on a surface presenting a high density of step-edges this process is already observed at 260 K. The Cu plays a catalytic role for the deprotonation of the ammonium group, the temperature dependence of this chemical process evidences a lower activation barrier at the step-edges.

In previous works on the assembly of alanine and glycine on Cu(110) surfaces, it was stated that the molecules bind on a-top surface sites with the amino ($-NH_2$) and deprotonated carboxyl ($-COO^-$) groups [13, 14]. In our case, from the analysis of the carbon C1s spectra for the LT- and HT-phases shown in fig.3.28, by using the assignments for the peaks presented in the previous section (C1 and C2 are assigned to the carbons bounded to sulphur, C3 to the -C-C-C- , C4 to the carbon bounded to the nitrogen and C5 to the one in the carboxyl group), the main differences between the two phases are present on the carbons bounded to the nitrogen and the oxygen. They shift to lower binding energy in the HT-phase with respect to the LT-phase, therefore by using a simple image charge model we can expect that both the carboxyl group and the amino group become closer to the surface going from the LT to the HT phase.

The reorientation of these two functional groups in the two phases is also confirmed by the NEXAFS carbon K-edge measurements. In fig. 3.29 are reported the carbon K-edge NEXAFS spectra for the LT- and HT-phases. The red traces in both graphs are the spectra acquired with the light polarization parallel to the surface, while the blue traces are the ones acquired with the light polarization perpendicular to the surface. The black lines are the best fits to the experimental data and at the bottom of each graph the peaks obtained from the best fits are also reported.

The peaks used in the fits are the same used in the previous section. It is evident that there are no strong variations between the two phases. The peak P1 was previously assigned to states formed upon adsorption and is present also in the case of Cu(111) for both phases. P2 and P3 were assigned to $\sigma^\star$(C-S) states. On Ag(111) and Au(110) they were strongly dichroic, while on Cu(111) the dichroism is poor. Their energy position in the LT-phase is identical to the Ag(111) case, while in the HT-phase there is a slight shift. This is connected to a shift in the C1 and C2 components of the carbon C1s XPS spectrum already observed. Going from the LT- to

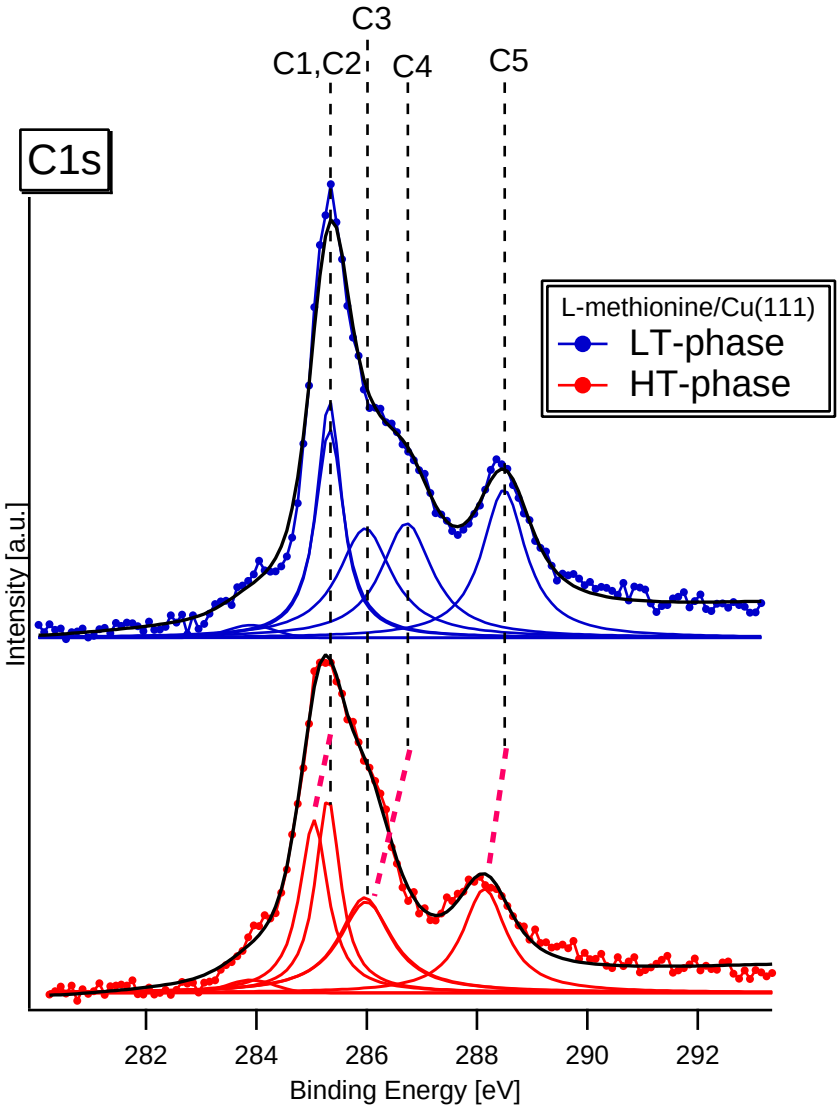

Figure 3.28: C1s XPS spectra for the LT-(blue) and HT-phases (red). The dotted lines are the experimental data, while the black solid lines are the fitting curves. On the bottom of each spectra the peaks obtained from the best fit are also reported.

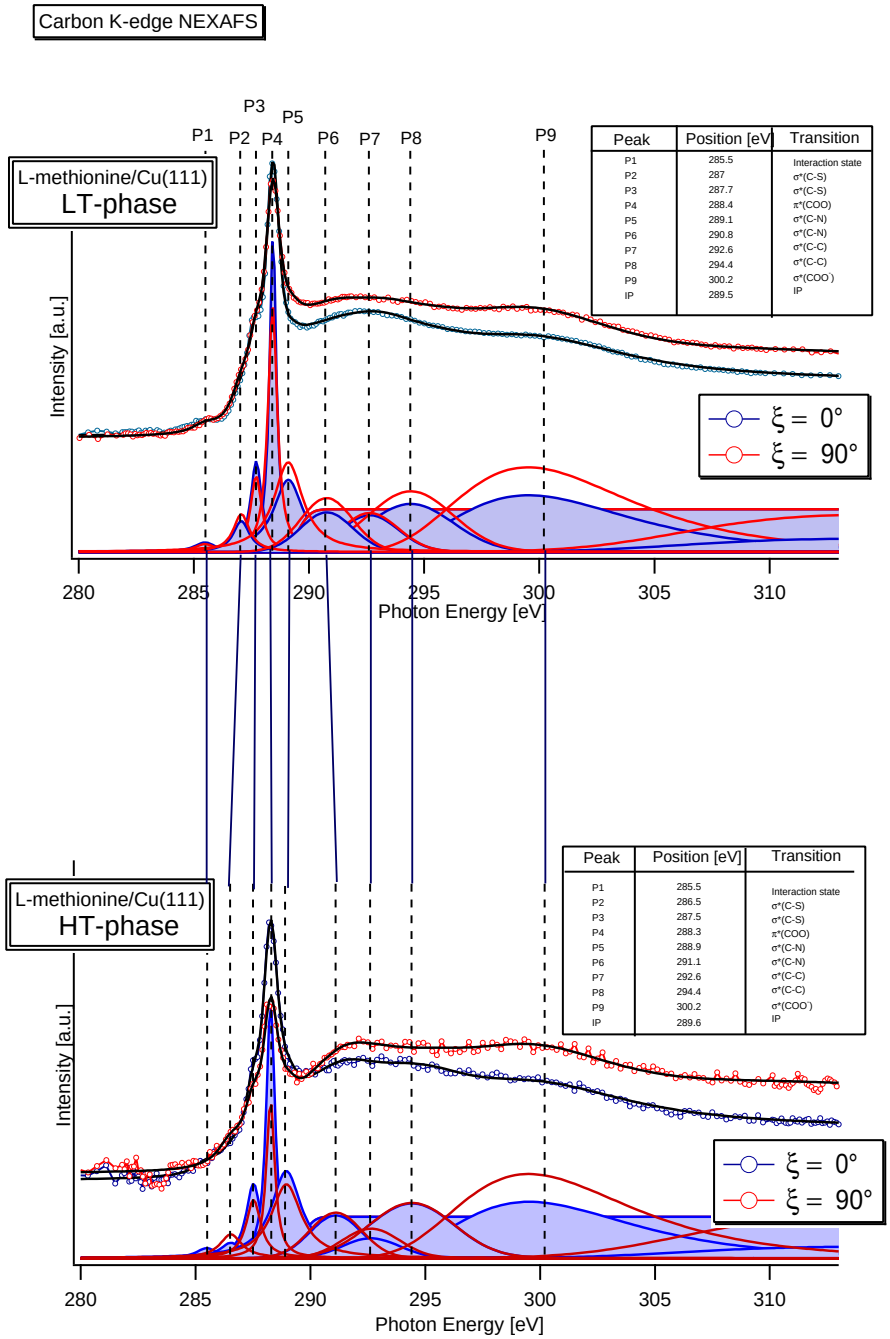

Figure 3.29: C K-edge NEXAFS measurements for the LT (top) and HT (bottom) phases. Each measurement is performed for the light polarization parallel to the surface $\xi = 90°$ and perpendicular to the surface $\xi = 0°$.

the HT-phase the C-S bonds change slightly. P4 was previously assigned to the $\pi^\star$(COO) state. P5 and P6 are $\sigma^\star$ states involving the nitrogen. Their position changes between the two phases reflecting the change of the oxidation state of the amino group following the same trend as on Ag(111) and Au(110). Interestingly the tilt of the COO^- plane changes between the two phases. The same yields for the C-N which tilts towards the normal of the surface. This can be related to the formation of new bonds with the surface atoms.

3.5.3 Discussion

From the observations presented, it is evident that the chemical state of L-methionine molecules on Cu(111) and the morphology of the formed films strongly depend on the substrate temperature during deposition. The LT-phase includes zwitterionic molecules which assemble into small clusters rotated by 10° with respect the $< 10 >$ substrate directions. These cluster are composed of dimers of molecules, as shown in figure 3.30(a), which is a high resolution LT-STM measurement.

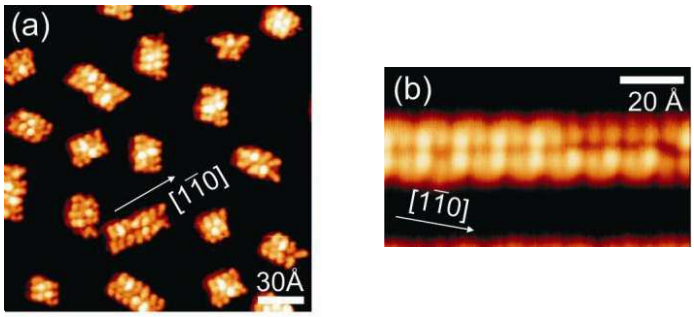

Figure 3.30: Molecular resolution STM data of LT- and HT-phases. (a) Molecular resolution of clusters in the LT-phase: dimerization and partial directional growth is observed along directions tilted 10° clockwise of the surface $< 10 >$ orientations (equivalent to $< 110 >$ crystal orientations) (I=0.1 nA, U=-100 mV). (b) Molecular resolution along the growth direction of the highly ordered phase (I=0.1 nA, U =-600 mV).

We can assume that the intermolecular bonding scheme is similar to the one found in the L-methionine/Ag(111) and Au(111) system, the 10° clockwise rotation with respect the $< 10 >$ orientations being necessary to match the energetically favorable adjacent intermolecular distance to the smaller

lattice constant of the Cu(111) substrate. In contrast to the highly linear regularity of the gratings found on Ag(111), the zwitterionic assembly in the LT-phase on Cu(111) shows only restrained one dimensional extensibility, which could be related to the reduced mobility and higher nucleation density of the adsorbate on the more reactive Cu(111) substrate.

The HT-phase is composed of anionic molecules with extended 1D order and a 10° counter-clockwise tilt relative to the $< 10 >$ orientations of the substrate. The rows in this phase are also composed of strings of dimers as shown in figure 3.30(b). The high resolution STM images evidence that the regularity in this dimer arrangement is significantly higher. A question remains concerning how an attractive interaction is possible between negatively charged entities as the anionic molecules. The polarizability of the metallic substrate plausibly enables the assembly process by screening the molecular negative charge through charge density redistribution. This hypothesis is supported by molecular mechanics simulations [35].

The described results present a scenario where the thermally activated ammonium deprotonation causes the orientational transformation between the low and high temperature cases. The low temperature preferential orientation of the supramolecular arrangement along a 10° clockwise tilt with respect to the $< 10 >$ directions represents already an adsorbate induced break of the threefold symmetry imposed by the surface crystalline structure: the molecular chiral signature leads to an enantiomorphic organization reflecting a preferential adsorption configuration. Work by Weigelt et al. [36] showed chiral switching due to thermally driven conformational changes of individual molecular units, whereas our system is characterized by collective chiral switching mediated by a thermally activated catalytic chemical reaction. The ammonium deprotonation reassigns a preferential adsorption-configuration, and the chiral properties of the system are altered as a consequence.

Bibliography

[1] Barth J.V., Costantini G., Kern K., Nature, 437 (2005) 671

[2] Barlow S.M., Raval R., Surf. Sci. Rep., 50 (2003) 201

[3] Barlow S.M., Raval R., Curr Opin in Colloid and Interface Science, 13 (2008) 65

[4] Schiffrin A., Riemann A., Auwärter W., Pennec Y., Weber-Bargioni A., Cvetko D., Cossaro A., Morgante A., Barth J.V., PNAS, 104 (13) (2007) 5279

[5] Schiffrin A., Reichert J., Auwaerter W., Jahnz G., Pennec Y., Weber-Bargioni A., Stepanyuk V. S., Niebergall L., Bruno P., Barth J.V., Phys. Rev. B., 78 (2008) 035424

[6] Peelle B. R., Krauland E. M., Wittrup K. D., Belcher A. M., Langmuir, 21, 6929 (2005)

[7] Strong A. E., Moore B. D., Chem. Comm., (1998) 473

[8] Gonnella G., Terreni S., Cvetko D., Cossaro A., Mattera L., Cavalleri O., Rolandi R., Morgante A., Floreano L., Canepa M., J. Phys. Chem. B, 109 (2005) 18003

[9] Cooper E., Krebs F., Smith McD., Raval R., J. Elec. Spec. Rel. Phen., 64/65 (1993) 469

[10] LeParc R., Smith C. I., Cunquerella M. C., Williams R. L., Fernig D. G., Edvards C., Martin D. S., Weightman P., Langmuir, 22 (2006) 3413

[11] Venkataraman L., Klare J. E., Nuckolls C., Hybertsen M. S., Steigerwald M. L., Nature, 442 (7105), 904 (2006)

[12] Park J. S., Whalley A. C., Kamenetska M., Steigerwald M. L., Hybertsen M. S., Nuckolls C., Venkataraman L., JACS, 129 (51), 15768 (2007)

[13] Nyeberg M., Hasselstrom J., Karis O., Wassdahl N., Weinelt M., Nilsson A., Pettersson L.G.M., J. Chem. Phys. , 112(12) (2000) 5420

[14] Hasselström J., Karis O., Weinelt M., Wassdahl N., Nilsson A., Nyberg M., Petterson L.G.M., Samant M.G., Stohr J., Surf. Sci., 407 (1998) 221

[15] Jones G., Jones L.B., Thibault-Starzyk F., Seddon E.A., Raval R., Jenkins S.J., Held G., Surf. Sci., 600 (2006) 1924

[16] Bozack M.J., Zhou Y., Worley S.D., J. Chem. Phys., 100 (11) (1994) 8392

[17] L. Floreano, G. Naletto, D. Cvetko, R. Gotter, M. Malvezzi, L. Marassi, A. Morgante, A. Santaniello, A. Verdini, F. Tommasini, G. Tondello, Rev. Sci. Instrum. 70 (1999) 3855

[18] Seah M.P., Smith G.C., Antony M.T., Surf. Interface Anal 15 (1990) 293

[19] Powell C.J., Erickson N.E., Jach T., J. Vac. Sci. Technol. 20 (1981) 625

[20] Stöhr Nexafs Spectroscopy, Springer-Verlag, Berlin, 1992

[21] Narasimhan S., Vanderbilt D., Phys Rev Lett, 69(10) (1992) 1564

[22] Robinson I.K., Physical Review Letters 50 (15) (1983) 1145

[23] Smith N. V., Chen C. T., Weinert M., Phys. Rev. B, 40(11) (1989) 7565

[24] Plekan O., Feyer V., Richter R., Coreno M., De Simone M., Prince K. C., Carravetta V., J. Phys. Chem. A, 111 (43) 10998

[25] Zubavichus Y., Shaporenko J., Grunze M., Zharnikov M., J. Phys. Chem. A, 109 (2005) 6998

[26] Kaznacheyev K., Osanna A., Jacobsen C., Plashkevych O., Vahtras O., Agren H., Carravetta V., Hitchcock A.P., J. Phys. Chem. A, 106 (2002) 3153

[27] Cooper G., Gordon M., Tulumello D., Turci C., Kaznatcheev K., Hitchcock A.P., J. Elec. Spec. Rel. Phen., 137-140 (2004) 795

[28] Zubavichus Y., Zharnikov M., Schaporenko A., Grunze M., J. Elec. Spec. Rel. Phen., 134 (2004) 25

[29] Zubavichus Y., Shaporenko A., Grunze M., Zharnikov M., J. Phys. Chem. B, 110 (2006) 3420

[30] Yang L., Plashkevych O., Vahtras O., Caravetta V. and Agren H., J. Synch. Rad., 6 (1999) 708

[31] Plashkevych O., Carravetta V., Vahtras O., Agren H., Chem. Phys., 232 (1998) 49

[32] Plekan O., Feyer V., Richter R., Coreno M., De Simone M., Prince K. C., Carravetta V., J. Elec. Spec. Rel. Phen., 155 (2007) 47

[33] Luo M.F., MacLaren D.A., Shuttleworth I.G., Allison W., Chem. Phys. Lett., 381 (2003) 654

[34] Otero E., Urquhart S.G., J. Phys. Chem. A, 110 (2006) 12121

[35] Schiffrin A., Reichert J., Pennec Y., Auwärter W., Weber-Bargioni A., Marschall M., Dell'Angela M., Cvetko D., Bavdek G., Cossaro A., Morgante A., Barth J. V., in preparation

[36] Weigelt S., Busse C., Petersen L., Rauls E., Hammer B., Gothelf K.V., Besenbacher F., Linderoth T.R., Nature Mat., 5 (2006) 112

Chapter 4

Amines on gold.

4.1 Introduction.

One of the main goals of nanotechnology is the miniaturization of electronic devices through exploitation of unique properties of matter at the nanoscale lengths. This technological request should lead to the development of novel applications and devices where nanostructures, molecules and quantum dots are the active elements of the device. At present, one of the most active areas of study is the development of electronic devices based on single organic molecules. However despite great efforts dedicated to the investigation of these systems, comprehensive conceptual understanding of electron transport in molecular systems is lacking, which limits the development of molecular devices and technologies that would be based on them.

Since the first model of molecular rectifier proposed by Aviram and Ranter in 1974 [1], a large variety of techniques for measuring electron transport properties of single organic molecules have been developed. The most successful techniques have been the statistical techniques of STM (Scanning Tunneling Microscope) break junction [2] and mechanically controlled break junction (MCBJ) [3, 4]. In the STM break junction technique an Au scanning microscope tip is repeatedly (several thousands of times) crashed in and moved out of an Au surface in molecular solution, while in the MCBJ a thin gold wire is repeatedly broken in a controllable way in presence of molecules. In both cases, as soon as the Au point contact is stretched and finally broken, one molecule can be trapped between the tip and the substrate or between the two wires respectively and form a metal-molecule-metal junction. It is then possible to apply a bias to the electrodes and measure the current passing through the molecule.
Although reliable and reproducible experiments have been reported recently

[5], serious problems, such as uncertainty about the number of conducting molecules in the junction and the poor control of contact geometry still remain to be resolved.

When a molecule is settled between two electrodes to form a metal-molecule-metal junction its electronic structure is affected by the electrodes because of molecule-electrode coupling: part of the states of the molecule spread into the electrode and at the same time part of the electrode states also spread into the molecule. The coupling between the discrete energy levels in the molecule and the continuum states of the leads affects the electron tunneling through the molecular junction (fig. 4.1)

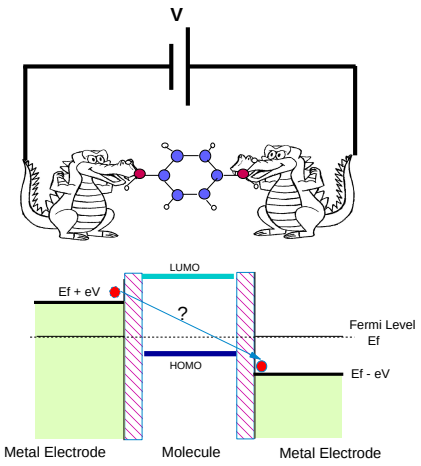

Figure 4.1: Sketch of a metal-molecule-metal junction and relative energy level diagram. HOMO and LUMO are the highest occupied molecular orbital and the lowest occupied molecular orbital respectively.

Transport characteristics are influenced by intrinsic molecular properties such as molecule length, conformation, gap between the highest occupied (HOMO) and lowest unoccupied (LUMO) molecular orbitals, and the alignment of this gap to the metal Fermi level [6]. Also the nature of the chemical linker groups used to bind molecules to metal electrodes plays a fundamental role: in ref [7] it was shown that the conductance of Au-molecule-Au junctions where the molecules are alkanes terminated with either amines (-NH_2), dimethyl phosphines (-PMe_2) or methyl sulfides (-SMe) exhibits large differences.

The chemisorption of thiol (-SH) terminated molecules on Au surfaces has been widely studied in the past 30 years [8]: the strong Au-S bond was therefore employed in the first break junction studies [2]. Recently it was

shown [5, 9] that amine (-NH_2) anchored molecular junctions exhibit well defined and experimentally more stable transport properties with respect to thiolated (-SH) molecules. This is surprising since the thiol-Au chemical bond is considerably stronger than the amine-Au bond and therefore one may expect that the stronger molecule-electrode link would reduce the stochastic switching and result into a more stable molecular junction. Moreover the weak amine coupling to the electrode would imply a decreased junction transparency for electron current.
The reason for the well-defined and stable conductance of amine anchored single-molecule junctions was attributed to the fact that the amine-Au bond takes place through the nitrogen lone-pair and it is relatively insensitive to the local structure [9, 11]. I will remember here that in chemistry the lone-pair on an atom is a valence electron pair that does not bind or is not shared with other atoms. Examining electron transport through molecules sandwiched between two gold contacts with first principle methods, Kim et al. [10], showed that the conductance is governed by the energies, spatial extent, and symmetries of the orbitals near the Fermi level rather than by the strength of the bonding.

Few experimental studies on the adsorption of amines onto surfaces have been reported ([12, 13, 14, 15, 16]), but none of them involved gold surfaces. Recently several theoretical studies, stimulated by the transport experiments, were performed in order to understand the binding of amines to Au surfaces and further explain the conductance experiments.
Hoft et al. [17] performed a Density Functional Theory study of the adsorption energetics of various amine compounds on the Au(111) surface. They concluded that:

- the sites with high coordination (bridge, fcc and hcp (fig. 4.2)) on the (111) surface are unfavorable for molecular adsorption and produce negligible adsorption energies. All the amine-terminated molecules studied adsorb more strongly when coordinated to gold adatoms located in the fcc position on the (111) surface or in the on-top site. The calculated adsorption energies are 0.3 eV $< E_{ads} <$ 0.6 eV (confirmed by [10], [18] and [5]) in the first case, and 0.1 eV $< E_{ads} <$ 0.3 eV in the second case.

- the interaction with the substrate is not strong in any of the adsorption sites, therefore little distortion of the molecule occurs upon adsorption. In fact the optimized geometry of the adsorbed molecules is close to the gas phase optimum geometry.

- the orientation of the amine molecule is always with the nitrogen point-

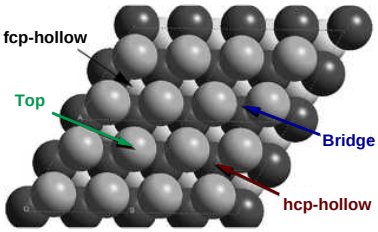

Figure 4.2: High symmetry adsorption sites on a (111) surface.

ing toward the substrate. The aromatic amines are adsorbed with the ring substituents relatively flat to the surface suggesting that part of the binding energy comes from interaction between delocalized π-electrons on the aromatic ring and the gold surface. In fact, when the molecule is adsorbed onto an adatom this interaction with the surface is weaker and consequently the ring is less flat on the surface.

- the responsible for the gold-amine bond is a *donation-back donation mechanism* in which the nitrogen atom donates charge into the surface which then backdonates into the amine molecule. Although bonding for the aromatic amines is complicated by the interaction of the electrons in the π-orbitals of the ring with the surface, it has been shown that the charge in that orbitals is not donated into the surface.

According to the first point, the bonding of amine terminated molecules on Au surfaces is weak, but site selective. In a different theoretical study, Kosov et al. [19], by comparing the absorption of benzenethiol (BT) and aniline molecules on Au(111) surfaces and on Au(111) surfaces with adatoms on the fcc sites, have shown that aniline adsorbs only on the second type of surfaces or on on-top sites of the first type, while benzenethiol adsorbs equally well on all the Au surfaces. The adsorption energy of the aniline with vertical benzene ring on the Au(111) surface with adatom sites is 0.5 eV larger than the one of the most stable non lying adsorption geometry on the Au(111) surface. Instead adsorption energies of benzenethiol on both surfaces are very similar (2.7 eV). Therefore in a Au-molecule-Au junction, where the molecule is the 1,4-benzenediamine (BDA), which is the equivalent of aniline with two amino groups to allow bonding to both electrodes, the number of accessible geometries is much smaller than that for the benzenedithiol (BDT). Only one geometry is sterically and/or energetically accessible for BDA junctions whereas three different geometries are possible for BDT. This suggests that

it is more likely for the amine terminated molecules to form single molecule junctions than for thiol terminated molecules.

In this chapter I will report on the adsorption and the energy level alignment of different amine-terminated molecules on Au surfaces.

First, we propose to answer the question whether do amines bind to Au(111) surfaces and if they prefer under coordinated gold sites. For this reason we have studied the adsorption of p-toluidine and 1,4-benzenediamine on two different surfaces, Au(111) and Au(110), whose atoms have different coordination. The characterization of the growth of these two molecules on Au(111) and Au(110) is reported in section 4.3 and in section 4.4, respectively. The experimental evidences show that the molecules bind stronger to Au(110) surfaces, that means to surfaces with lower coordinated atoms. From the X-ray Photoemission Spectroscopy (XPS) and Near Edge X-Ray Absorption Fine Structure (NEXAFS) data presented we can conclude that the amino group is involved in the bonding of the molecule to the surface.

Second, we aim to study the electronic structure of the molecular layer by means of Resonant photoemission spectroscopy (RPES). This is presented in section 4.5. In RPES experiments, as described in chapter 2, electrons in a particular core level are first photoexcited by soft X-ray photons to a resonant bound state with the system remaining charge neutral (XAS). This is followed by deexcitation of the system via predomaninantly Auger-like transitions. If the excited electrons are localized at an excited orbital for a sufficiently long time two new transitions are possible: resonant Auger transition, where the final state has two holes left in the occupied molecular orbitals and one excited electron in the unoccupied molecular orbitals or resonant photoemission where the final state has one hole left in the occupied molecular orbitals and is in an energetically equivalent final state as normal valence band photoemission. If the molecular orbitals are strongly coupled to the substrate, there is the possibility of interface charge transfer in which the excited electrons directly decays into the substrate conduction band and the core hole decays via a normal Auger process leaving a two hole final state. The RPES signal intensity, which corresponds to the presence of resonant Auger and resonant photoemission transitions, can be used as an indicator to reflect the coupling strength between the molecules and the substrate and to reveal changes in the extent of localization of molecular orbitals.
For the two molecules studied, electrons excited from C1s core level to empty orbitals localized on the carbons bounded with the amino groups experience a fast charge transfer, which can be an indication that the coupling of the molecule with the surface takes place through the amino groups.

Third, in section 4.6 I will present the characterization of the alignment of the occupied molecular orbitals with respect to the Fermi level for three ben-

zene substituted diamines monolayers on Au(111). This information, that has been obtained from RPES and Ultraviolet Photoemission Spectroscopy (UPS) measurements, is essential, as will be explained later, to help to understand the differences between the conductance values calculated from the theory and the measured values in STM-break junction experiments.

4.2 Experimental details.

All the measurements presented in this chapter were performed at the ALOISA/HASPES beamline. The experiments were performed under ultrahigh vacuum (UHV) conditions. The molecules studied (p-Toludine, 1,4-Benzenediamine (BDA), Tetramethyl-1,4-Diaminobenzene (TMBDA), Tetrafluoro-1,4-Diaminobenzene (4F-BDA)) are depicted in figure 4.3. The first three were purchased from Sigma-Aldrich, the last from TCI-America. All of them have purity above 98%, only p-Toluidine was 90% pure.

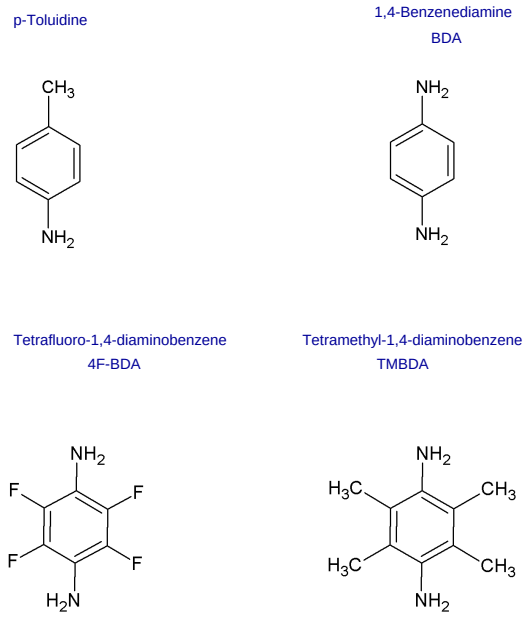

Figure 4.3: Scheme of the aromatic diamino molecules studied.

The Au(111) and Au(110) samples were prepared in UHV by repeated Ar^+ sputtering cycles at an energy of 0.8 keV, followed by annealing at a temperature of 770 K.

The molecules were vapor-deposited onto the Au substrates from a glass crucible kept at room temperature. Before each deposition the surfaces were checked by means of XPS to be contaminat free (oxygen, carbon, sulphur, nitrogen). During deposition, the substrate was held at different temperatures ranging from 240 K to 350 K in order to obtain different molecular coverages.

All XPS, NEXAFS and RPES spectra have been measured from a freshly deposited film and by keeping the sample temperature below 150 K to minimize the radiation damage. Moreover the sample has been continuously moved during data acquisition in order to expose fresh sample regions to the beam. In fact, we observed that the exposure to the synchrotron radiation beam causes damage. Indication of the damage are the slight changes in the N1s and C1s XPS profiles and, more clearly, the appearance of new features in the N K-edge NEXAFS in the region between 395-400 eV. In fig. 4.4 this changes are shown for a BDA multilayer.

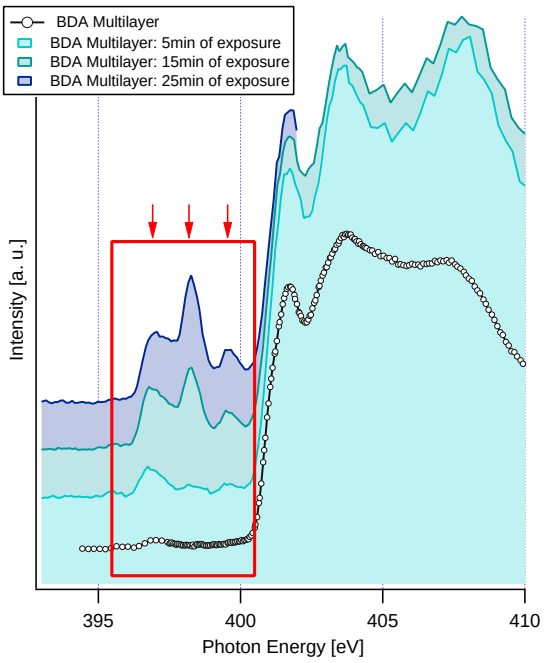

Figure 4.4: Nitrogen K-edge NEXAFS spectra of a pristine multilayer of 1,4-Benzenediamine (dotted lines) and of a multilayer of 1,4-Benzenediamine after exposure to the X-rays.

It is well known that aromatic diamines can polymerize in different conditions and even when exposed to light ([20, 21]). A specific molecule can form

a large variety of polymers with different properties [20]. If we consider the 1,4-Benzenediamine (1,4-BDA), the polymerization can proceed via bonding of the amino group of one molecule with the carbons on the benzene ring not attached to the nitrogen of a second molecule or via the formation of double bonds between the amino groups of different molecules. It was not possible to find in literature Nitrogen K-edge NEXAFS measurements of the polymers formed from 1,4-BDA. However we can consider for comparison the Nitrogen K-edge NEXAFS measurements performed on polyaniline by Henning et al. [22]. Polyaniline is obtained from polymerization of aniline. Aniline contains a benzene ring with attached a single amino group and its polymerization involves the bonding of the amino group to the carbons of the benzene ring, as in the first type of polymer of 1,4-BDA. In this case the reported Nitrogen K-edge NEXAFS is very similar to our measurements [22]. In case of polymerization via the formation of double bonds between the amino groups, this can also produce the appearance of new peaks in the Nitrogen K-edge NEXAFS in the region 395-400 eV [23].

All the reported XPS spectra have been taken at 500 eV photon energy with an overall energy resolution of about 300 meV [25]. The binding energies on the XPS spectra were calibrated with respect to the literature Au4$f_{\frac{7}{2}}$ value at 84 eV [24].

C K-edge and N K-edge partial yield NEXAFS measurements were performed on the sample with an incident grazing angle of 6°. The absolute photon energies were calibrated with the absorption spectra of gas phase CO and nitrogen gas measured in the ALOISA ionization cell [25]. The measured spectra were normalized by dividing the signal from the film with the one taken on the clean substrate. This normalization procedure is described in [26].

4.3 p-Toluidine and 1,4-Benzenediamine on Au(111).

4.3.1 p-Toluidine

The characterization of the growth of p-toluidine films on Au(111) has been performed by means of XPS and NEXAFS.

As starting point we choose the multilayer of p-Toluidine deposited on the sample kept at 250 K. The XPS N1s and C1s spectra are reported in figure 4.5 (brown traces). The nitrogen N 1s XPS spectra shows a single peak at $E_{N^1_{1s}} = 399.7 \pm 0.1$ eV. The carbon C 1s can be fitted with two components located at $E_{C^1_{1s}} = 285.0 \pm 0.1$ eV and $E_{C^2_{1s}} = 286.1 \pm 0.1$ eV.

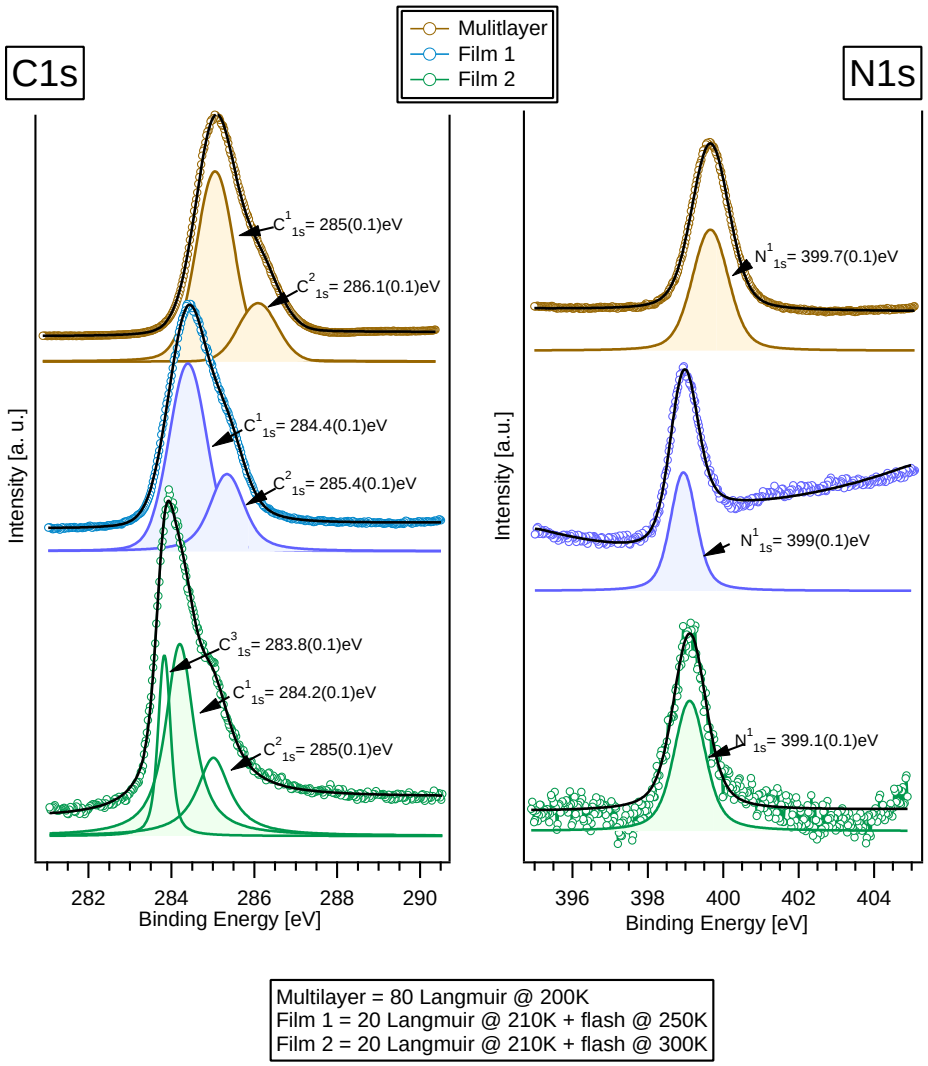

Figure 4.5: C1s and N1s XPS spectra of different layers of p-toluidine on Au(111). (The preparation procedure is indicated in the figure.) The dotted curves are the experimental data, while the black solid lines are the best fits. On the bottom of each spectrum the peaks obtained from the best fit are also reported.

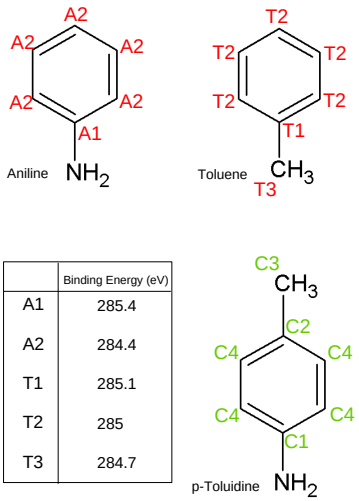

	Binding Energy (eV)
A1	285.4
A2	284.4
T1	285.1
T2	285
T3	284.7

Figure 4.6: Sketch of the Aniline, Toluene and p-Toluidine molecules. In the table are reported the measured C1s XPS binding energies for Aniline and Toluene taken from [12, 27].

The molecule contains four chemically inequivalent carbons (C1, C2, C3, C4), as shown in figure 4.6. According to the literature values for the C 1s binding energies of aniline [12] and toluene [27] (reported in the table of fig. 4.6), we assign $E_{C^2_{1s}}$ to the carbon bonded with the amino group (C1), while the other three carbons (C2, C3, C4) are close in energy and can be included in the broad component $E_{C^1_{1s}}$.

To achieve monolayer or submonolayer coverages, the multilayer can be then gently heated whereby the physisorbed molecules are desorbed.
By looking at the variations in the XPS spectra for N 1s and C 1s upon flashing, it is possible to identify two coverages with distinct spectroscopic characteristics (fig. 4.5). The first (Film 1: blue lines) has been obtained by flashing the multilayer at 250K, while in the second (Film 2: green lines) the sample was heated up to 300K. From the attenuation of the Au_4f signal in the XPS measurements it was not possible to determine the coverage, since the attenuation is quite small. Instead the spectroscopic signature of the multilayer and second layer is clear. Therefore in the following I will always refer to monolayer or submonolayer coverages when the XPS peaks of the multilayer or second layer are not present.

The N 1s XPS spectra for this two coverages are single peaks at $E_{N_{1s}} = 399 \pm 0.1$ eV and 399.1 ± 0.1 eV respectively.

The C 1s spectra in the first case (Film 1) can be fitted with the same two components as the multilayer shifted to lower energy by an amount of 0.6 eV and 0.7 eV for $E_{C^1_{1s}}$ and $E_{C^2_{1s}}$, respectively. In the second case (Film 2) the component $E_{C^1_{1s}}$ shifts to lower binding energy by 1.1 eV with respect to the value of the multilayer, while the main component splits into two peaks. The component $E_{C^3_{1s}}$ can be assigned to the methyl group of the p-toluidine (C3), while the other to the remaining carbons in the benzene ring (C2,C4).

A tentative model that can explain these results is the following: for low coverages the molecules lie flat on the surface, while for intermediate coverages the molecules are slightly tilted on the surface with the nitrogen always bounded to the gold substrate. The methyl component shifts to higher binding energy since the methyl group lies at a larger distance from the surface. The nitrogen N 1s XPS peak remains at the same binding energy since the amino group is bound to the surface.

This model is confirmed by the NEXAFS spectra at the nitrogen and carbon K-edges reported in fig 4.7.

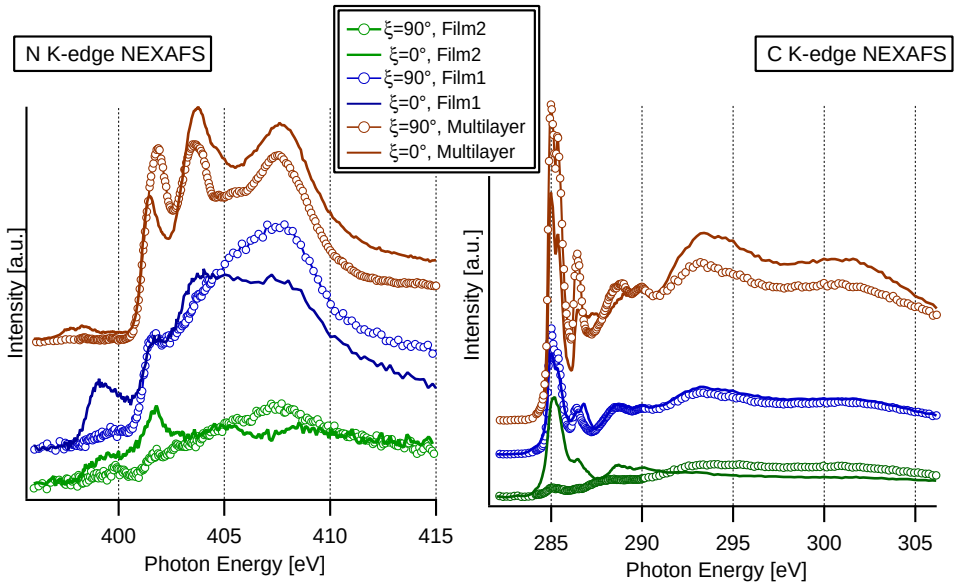

Figure 4.7: Nitrogen K-edge NEXAFS and Carbon K-edge NEXAFS for the thin films of p-Toluidine on Au(111) described in figure 4.5. For each coverage two measurements were performed, one with the light polarization parallel to the surface ($\xi = 90°$) and one perpendicular to the surface ($\xi = 0°$). The angle ξ is defined as in figure 3.18.

The nitrogen and the carbon NEXAFS spectra for the multilayer acquired

with the polarization parallel ($\xi = 90°$) or perpendicular ($\xi = 0°$) to the surface exhibit a weak dichroism. This can mean that the molecules are almost disordered or all of them are tilted at the so called "magic angle" (54.7°) [26].
The spectra for the other two coverages show an interesting behavior. For low coverages (Film 2), the first peak in the C1s NEXAFS, usually assigned to the $\pi^\star$ state localized on the benzene ring [12], presents a strong dichroism, meaning that the benzene ring is flat or almost flat on the surface. For intermediate coverages (Film 1) the molecules are tilted on the surface since the spectra acquired with $\xi = 0°$ and $\xi = 90°$ are quite similar. If we look at the nitrogen K-edge NEXAFS spectra it is possible to notice that they present a very broad peak at 400 eV, which is not visible in the pristine multilayer. In the multilayer, however, the small features in the pre-edge region below 400 eV are a signal of polymerization (as already discussed in the previous section). Some recent calculations have shown that the Nitrogen K-edge NEXAFS of the amino group bonded to Au adatoms via the lone pair presents states whose energy position is lowered by about 2 eV with respect to the gas phase molecules. Therefore the broad peak at 400 eV visible for the two thin films can be an indication of the interaction of the amino group with the surface.

4.3.2 1,4-Benzenediamine/Au(111)

The characterization of the growth of 1,4-Benzenediamine (BDA) films on Au(111) was also performed by means of XPS and NEXAFS. As in the case of p-toluidine the starting point was a multilayer, which was subsequently flashed at different temperatures: respectively 270K, 295K and 315K.

The BDA molecule in the multilayer presents only two chemically different carbons separated in binding energy by 0.9 eV, as shown in fig 4.8. Consistently with the assignments provided in the previous section, we can attribute $E^1_{C_{1s}}$ to the carbons of the ring attached to the amines (C1) and $E^2_{C_{1s}}$ to the remaining ones (C2).

In fig. 4.9 the XPS C1s and N1s spectra are reported for BDA films at different coverages denoted as Film 1, Film 2 and Film 3. They were obtained by depositing 50 Langmuir at room temperature and then by annealing the sample at 3 different temperatures as indicated on the figure. For Film 3 the nitrogen peak presents a single component (N1) and the carbon one is composed by two peaks. This suggests that all the molecules on the surface at this coverage are chemically equivalent. In this case we can hypothesize, by comparing these data with the p-toluidine ones, that the molecules are flat on the surface with both nitrogens in contact with the surface.

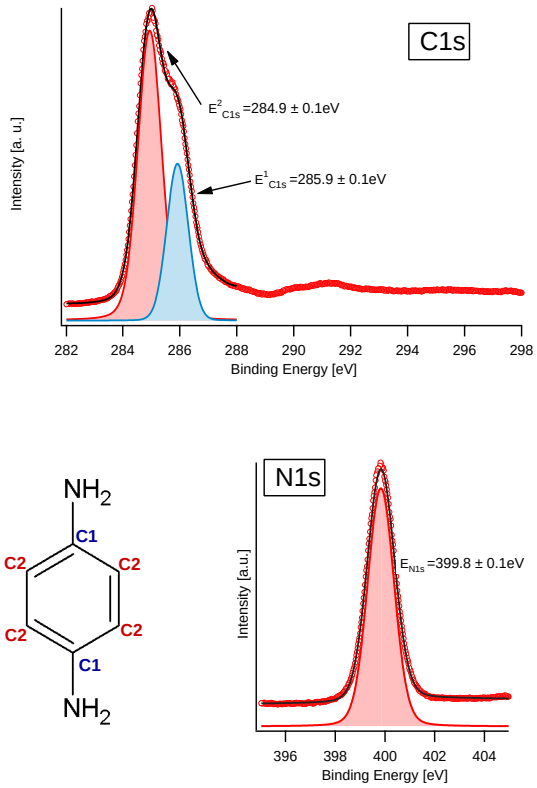

Figure 4.8: C1s and N1s XPS spectra of a multilayer of 1,4-Benzenediamine. The dotted lines are the experimental data and the solid lines are the best fit. On the bottom of each spectrum the peaks obtained from the best fit are also reported.

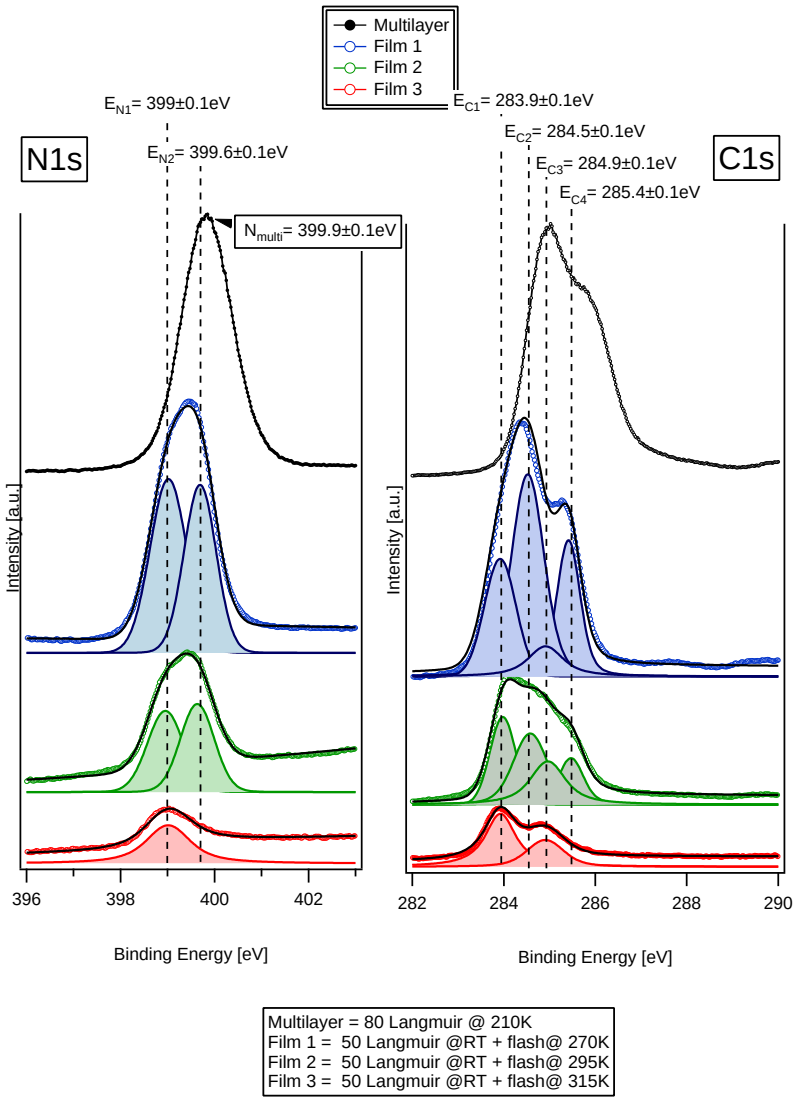

Figure 4.9: C1s and N1s XPS spectra of different layers of 1,4-Benzenediamine on Au(111). (The preparation procedure is indicated in the figure.) The dotted curves are the experimental data, while the black solid lines are the best fits. On the bottom of each spectrum the peaks obtained from the best fit are also reported.

By increasing the coverage a second nitrogen component shows up and also a second pair of carbon peaks, indicating the presence of molecules in a different chemical environment with respect to the flat ones. One possibility is that the molecules adsorb on top of a first layer of flat molecules. A second possibility is that as in the case of p-toluidine the molecules do reach a higher packing density via the change of the angle between the surface and the benzene ring and remain bounded only with one nitrogen.

In the previous section the appearance of states at 400eV in the nitrogen K-edge NEXAFS spectra was attributed to the interaction of the amino group with the metal surface. This states are also visible for the coverages of Film 2 and Film 3 of BDA on Au(111), as reported in fig.4.10 (top left). In particular, the carbon K-edge NEXAFS for Film 3 (top right) confirms that the benzene ring is flat on the surface since the first two peaks that are associated to $\pi^\star$ transitions on the benzene ring present a strong dichroism. Another signal of interaction of the molecule with the surface is that the peaks in the Carbon K-edge NEXAFS going from the multilayer to the monolayer exhibit a strong broadening [26]. Finally in the low coverage case (Film 3), the nitrogen NEXAFS dichroism is the same as the one for p-toluidine flat on the surface (fig.4.10, bottom).

4.3.3 Conclusion

From the data presented in this section the same adsorption scheme for 1,4-Benzenediamine and p-Toluidine on Au(111) can be adopted. In particular, the first deposition stages are characterized in both cases by molecules adsorbed with the benzene rings flat on the surface. For the p-Toluidine molecules, by increasing the molecular coverage the angle between the benzene rings and the surface changes, but the amino groups remain still interacting with the surface. For the 1,4-Benzenediamine molecules, the increase of the coverage produces a similar rearrangement of the benzene rings and only one of the two amino groups remains interacting with the surface. We can conclude that the amino group can be therefore responsible of bonding of the molecules to the Au(111) surface. The interaction of the amino lone pair with the Au surface can be identified with the broad peak at 400 eV in the Nitrogen K-edge NEXAFS spectrum.

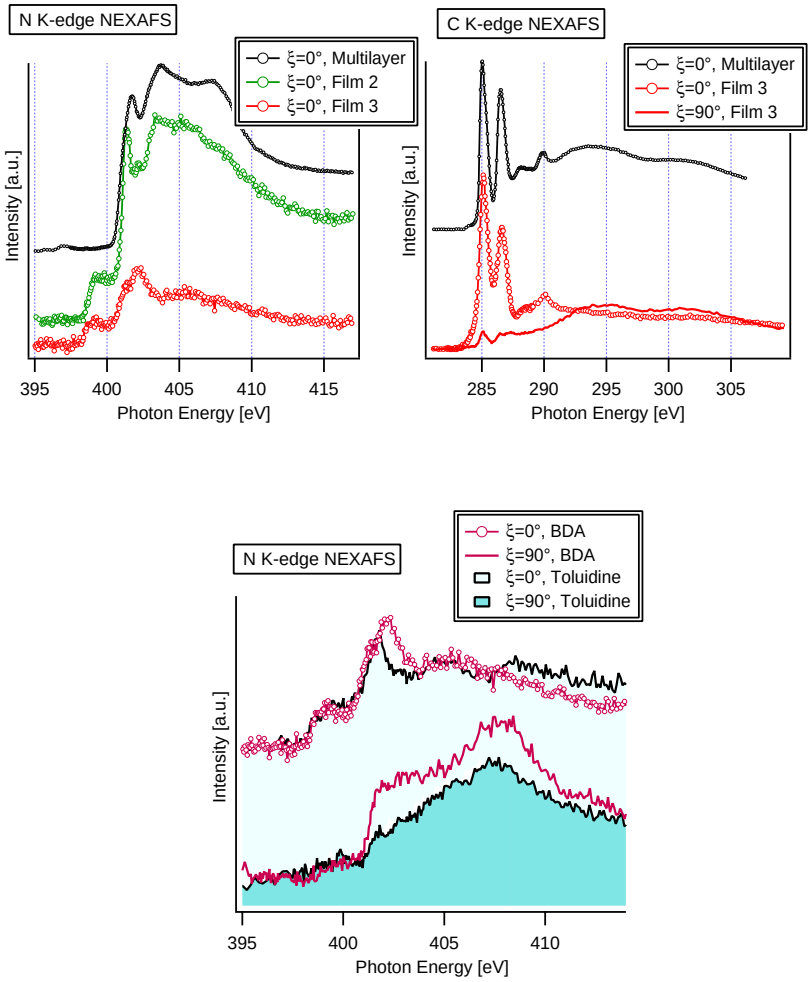

Figure 4.10: Top left: Nitrogen K-edge NEXAFS of the layers of 1,4-BDA corresponding to the XPS in figure 4.9. Top right: Carbon K-edge NEXFAS of the layers of 1,4-BDA of selected coverage. Bottom: Nitrogen K-edge NEXAFS of the low coverage of 1,4-BDA film compared with the NEXAFS of the low coverage film of p-toluidine. The spectra acquired with the light polarization perpendicular to the surface are displayed with an offset for clarity. In all the graphs the angle ξ, that is the angle between the light polarization and the surface, is defined as in figure 3.18

4.4 p-Toluidine and 1,4-Benzenediamine on Au(110).

4.4.1 p-toluidine/Au(110)

The study of the growth of p-toluidine on Au(110) was performed by looking at the changes in the C1s and N1s XPS spectra of films obtained by dosing 18 Langmuir of molecules with the substrate kept at different temperatures: 250 K, 260 K, 305 K, 330 K.

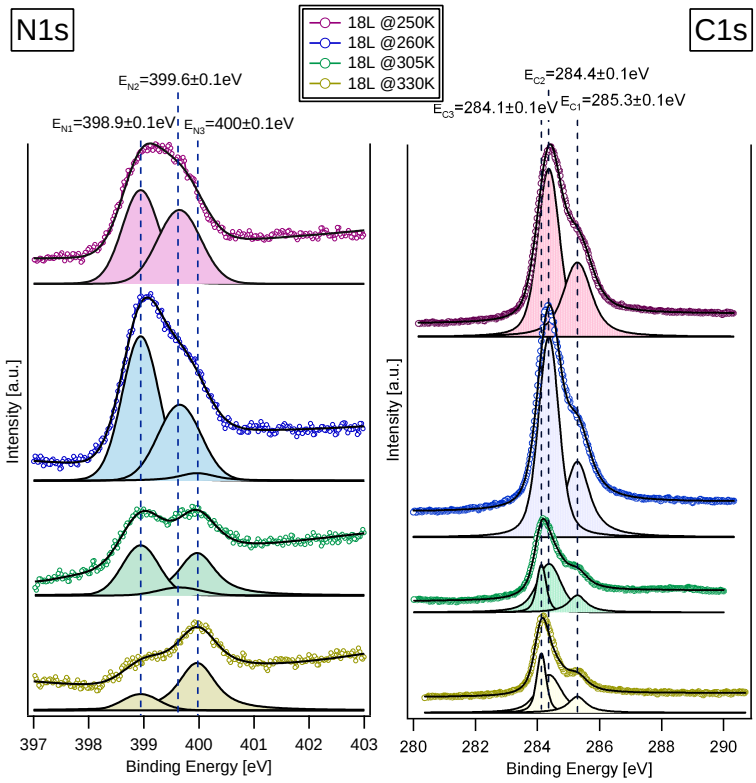

Figure 4.11: C 1s and N 1s XPS spectra of different layers of p-Toluidine on Au(110). The dotted curves are the experimental data, while the black solid lines are the best fits. On the bottom of each spectrum the peaks obtained from the best fit are also reported.

The first point to be underlined is that it is possible to deposit material at higher temperatures with respect to Au(111). This means that the molecules adsorb more strongly on Au(110) than on Au(111) and this is a clear indication that the molecules on the two gold surfaces present different

binding energy. This point will be more thoroughly addressed studying the desorption of a 1,4-benzenediamine film by means of HAS in the next section.

In figure 4.11 the N 1s and C 1s XPS spectra for all the depositions are reported. The film growth at 250 K presents two nitrogen peaks at $E_{N1} = 398.9 \pm 0.1$ eV and $E_{N2} = 399.6 \pm 0.1$ eV. The C 1s specrum can be fitted with two components at $E_{C1} = 285.3 \pm 0.1$ eV and $E_{C2} = 284.4 \pm 0.1$ eV. By comparing this values with the one found on the (111) surface, we can assign N1 to the nitrogen atoms bound to the surface and N2 to the nitrogen atoms at larger distance from the surface. The C1 peak can be attributed to the carbon atom connected with the amino group, while the C2 peak contains the contributions of all the remaining carbon atoms. Because of the presence of two nitrogen peaks we can conclude that at this coverage only a fraction of the molecules are bound to the surface via the amino groups.

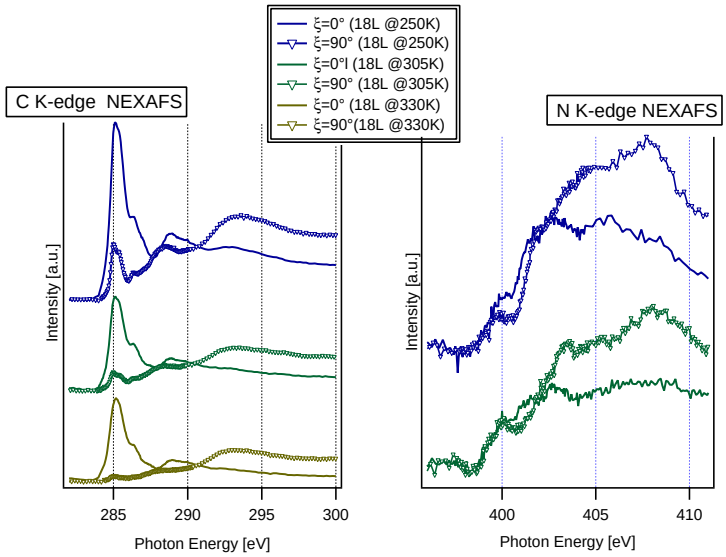

Figure 4.12: Carbon K-edge and Nitrogen K-edge NEXAFS spectra for different depositions of the p-toluidine on Au(110). The procedure for film preparation is indicated in the legend. The spectra were acquired with the light polarization parallel ($\xi = 90°$) or perpendicular ($\xi = 0°$) to the surface. The angle ξ between the light polarization and the surface is defined as in figure 3.18.

For the films obtained with higher substrate temperature during deposition, the unbound nitrogen peak disappears and a third peak appears at $E_{N3} = 400 \pm 0.1$ eV. The carbon shows morover a component at $E_{C1} = 284.1 \pm 0.1$eV that on Au(111) was associated with the methyl group inter-

acting with or very close to the gold. The new nitrogen component can be associated to molecules bound to a different adsorption site on the surface or can be related to some change on the nitrogen of the molecule due to the annealing process.

In figure 4.12 the Carbon K-edge NEXAFS and the Nitrogen K-edge NEXAFS for selected depositions are reported. From the polar dependence of the C1s NEXAFS, it is clear that at higher temperatures, the benzene rings become more flat on the surface. The spectra on the Carbon K-edge do not show new features with respect to the multilayer, a part broadening of the peaks that can be due to the interaction with the surface. Therefore probably if there are structural or chemical changes in the molecules due to the heating, these affect mainly the amine termination of the molecule. The nitrogen NEXAFS shows again the states at 400eV that we have associated to the molecules interacting to the surface via the nitrogen atom. From these results we can conclude that this interface is more disordered than the one on Au(111) and presents molecules adsorbed in several different ways. However we found a confirmation that in this case the nitrogen bonds to the Au atoms.

4.4.2 1,4-Benzenediamine/Au(110)

In figure 4.13 the N 1s and C 1s XPS spectra are reported corresponding to the multilayer (Film 1) and three coverages (Film 2, Film 3 and Film 4) of 1,4-Benzenediamine on Au(110). The procedures followed for the film preparation are indicated on the figure. The coverage decreases going from Film 1 to Film 4.

The N1s XPS spectrum of the multilayer shows a single peak at $E_{Nmulti} = 400 \pm 0.1$ eV. For lower coverages (Film 2 and 3) the nitrogen XPS signal can be decomposed into two components at $E_{N1} = 398.8 \pm 0.1$ eV and $E_{N2} = 399.6 \pm 0.1$ eV. By using the assignments done for p-toluidine in the previous section, we can attribute E_{N2} to the unbound $-NH_2$ and E_{N1} to the $-NH_2$ interacting with the surface. At lower coverages (Film 4) a third component shows up at $E_{N3} = 399.9 \pm 0.1$ eV. It is found at the same binding energy as the one found for low coverages in the system of p-toluidine on Au(110), that was also attributed to bounded nitrogens on the (110) surface. By heating the sample to higher temperatures, the peak at E_{N2} completely disappears and the peak at E_{N3} becomes dominant as shown in fig. 4.14. This behavior is similar to the p-toluidine case.

The C 1s XPS spectrum for the multilayer in fig. 4.13 presents two main components splitted by 0.9 eV, that can be assigned to *C*-N ($E_{C1multi}$) and C-*C*-C ($E_{C2multi}$). Film 2 and Film 3 present four peaks that can be attributed to two different types of molecules on the surface. In particular the intensities

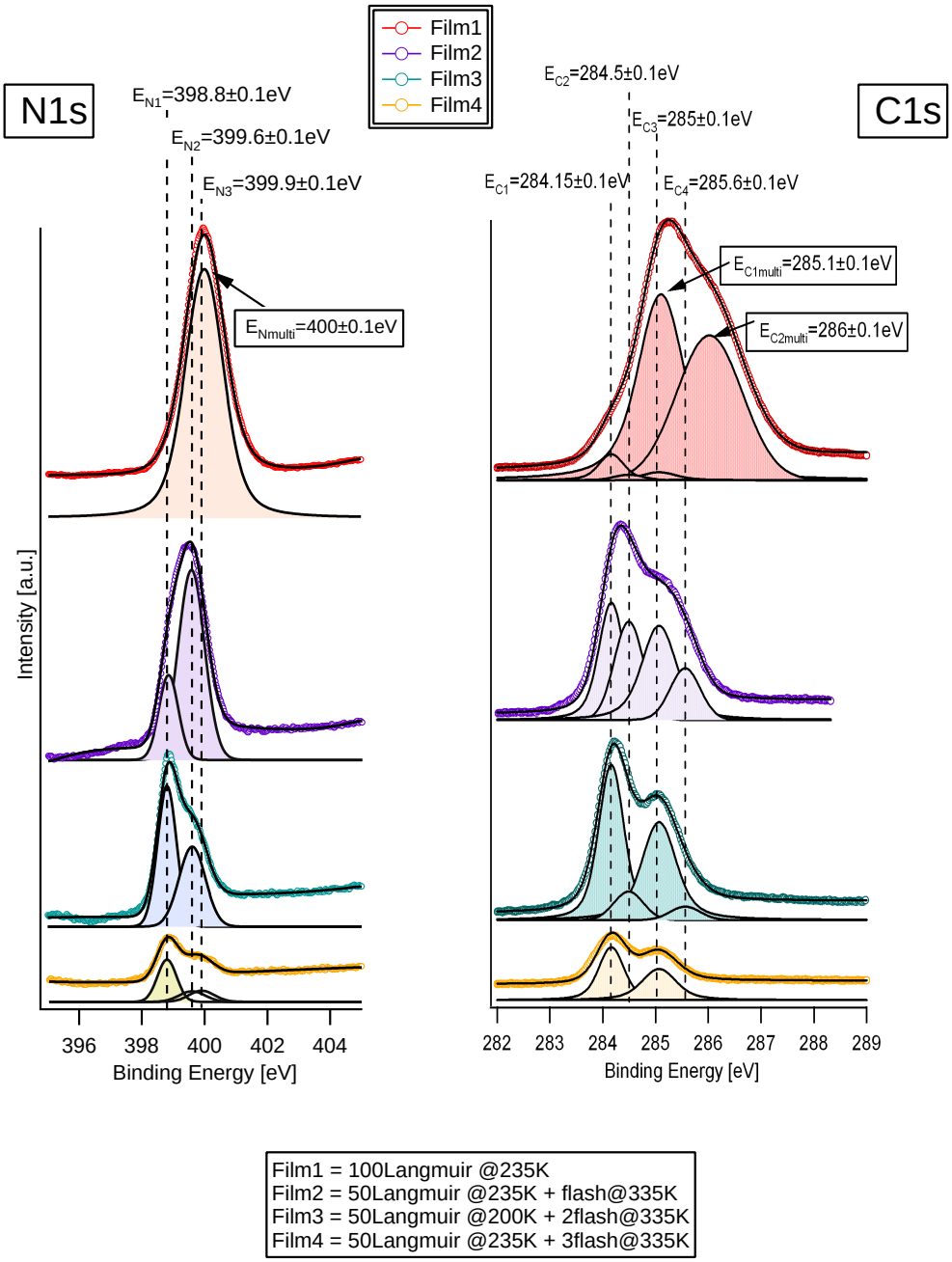

Figure 4.13: N s and C 1s XPS spectra for films of 1,4-BDA on Au(110). The preparation procedures are indicated in the legend. The dotted curves are the experimental data, while the solid black lines are the best fits. On the bottom of each spectrum the peaks obtained from the best fit are also reported.

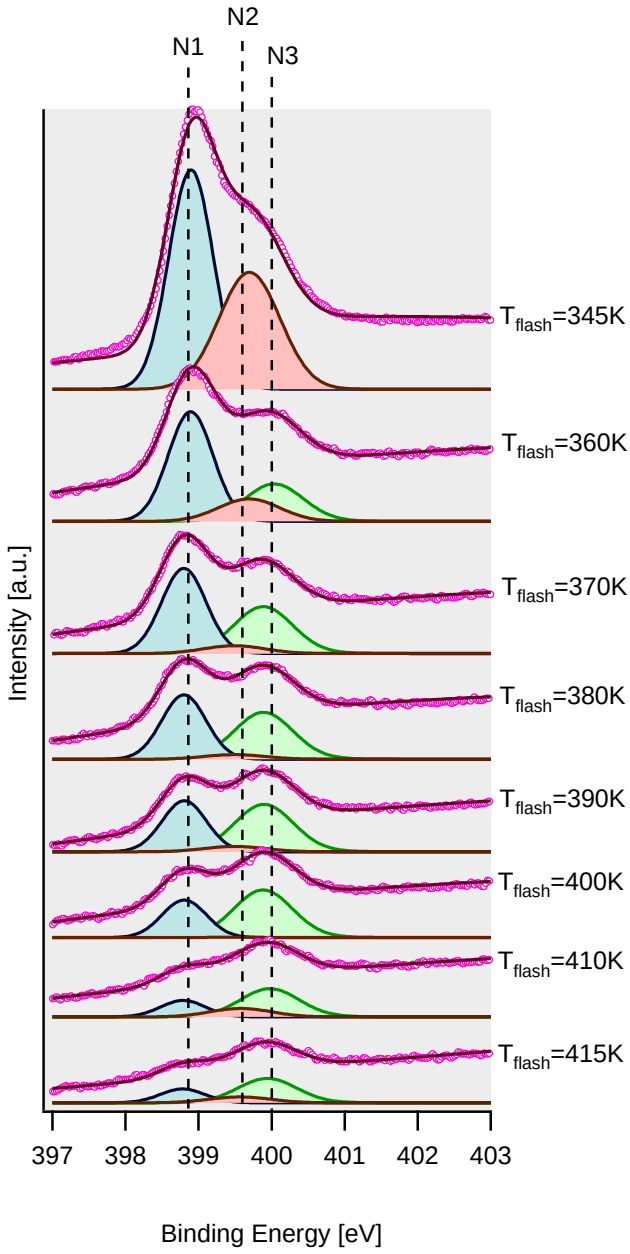

Figure 4.14: N 1s XPS spectra of a film of 1,4-BDA on Au(110) taken at 270 K after consecutive flashes at the reported temperatures. The dotted lines are the experimental data. On the graph are also reported the fits and the peaks obtained from the best fit for each spectrum.

of the peaks at E_{C2} and E_{C4} decrease by lowering the coverage following the decrease of the E_{N2} component (free amino group). Therefore we can assign them to a second layer of molecules lying on bounded molecules of the first layer characterized by E_{C1} and E_{C3}.

In figure 4.15 are reported the Nitrogen K-edge and Carbon K-edge NEXAFS spectra for the molecules of the multilayer (Film 1) and for the two coverages previously identified as Film 2 and Film 4. For each film the measurements were performed with the light polarization parallel ($\xi = 90°$) and perpendicular ($\xi = 0°$) to the surface as defined in figure 3.18. In the low coverage case (Film 4) from the Carbon K-edge NEXAFS spectra we can conclude that the benzene rings lie almost flat on the surface. Moreover the spectra for the Nitrogen K-edge are similar to that of the p-Toluidine on Au(110) and present the 400eV feature previously assigned to the amino group interacting with the surface.

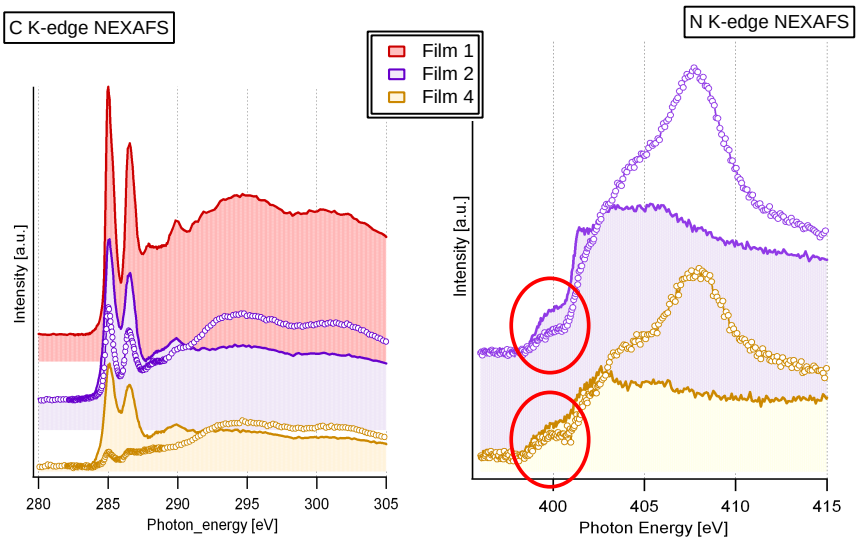

Figure 4.15: Carbon K-edge and Nitrogen K-edge NEXAFS of the corresponding films in fig. 4.13. The measurements were performed with the light polarization parallel ($\xi = 90°$, dotted lines) and perpendicular ($\xi = 0°$, solid lines) to the surface.

We can conclude that the 1,4-BDA molecules can bind to Au(110) in two distinct configurations, identified by the two N1s XPS peaks, while on Au(111) the bound amino groups are always present in just one configuration since there is only one N1s XPS peak for the bound molecules. This can be explained by taking into account that Au(110) is composed by surface atoms having coordination equal or lower with respect to Au(111) and, as already

mentioned, recent calculations have shown that amines bind preferentially on undercoordinated gold atoms [9]. Therefore on Au(110) more adsorption sites are allowed.

By taking into account the coordination of the surface atoms, the binding of the molecules to the Au(110) surface should be favoured with respect to the Au(111) surface. This is confirmed by the comparison of Helium Atom Scattering (HAS) measurements on 1,4-Benzenediamine films grown on Au(110) and Au(111).
The top graph of figure 4.16 shows the change of the HAS specular intensity while heating multilayers of 1,4-Benzenediamine grown at 200K on Au(111) and Au(110) respectively. As described in chapter 2, the scattering potential of the He atoms in the incident beam depends on the surface corrugation, therefore changes in the surface corrugation can be monitored as changes in specular reflectivity during surface processing. The multilayer presents an high degree of disorder therefore at 200 K there is no signal from specular beam. The increase of the HAS specular intensity during the flash signals the presence of sample regions with lower surface corrugation. This can be due to the presence of islands with ordered molecules or to the presence of islands of uncovered substrate regions. The 1,4-BDA films were heated up to the HAS specular intensity corresponding to the clean surface was recovered. From the measurements we can conclude that on Au(110) 1,4-BDA molecules are strongly bound with respect to Au(111), since the desorption ends at higher temperatures.

By following the variation of the HAS specular intensity during the desorption of the multilayer grown on Au(110), it is evident that there is an interval of temperatures in which the specular intensity does not change. This is an indication that for that temperatures in the range of 320-370 K the molecules rearrange without desorbing. From the measurement of the HAS diffraction pattern for multilayers heated up to 350 K (not shown), the surface presents a times 3 reconstruction along the [1 0] direction (the directions are given with respect to the lattice vectors in fig. 3.13). The same reconstruction can be obtained by depositing molecules with the sample kept at 330K, as shown in the bottom part of figure 4.16. The image in the bottom left of figure 4.16 shows the change of the diffraction pattern taken along the [1 0] direction while depositing molecules with the sample at 330K. In the abscissa is reported the momentum exchanged and in the ordinate is reported the deposition time. Each cut at fixed deposition time of this image is a section of the reciprocal space along the [1 0] direction. In the graph on the right two profiles are reported corresponding to diffraction scans at almost the beginning (A) and the end (B) of the deposition. The starting point is the (1x2) missing row reconstruction for the clean Au(110)

surface. At the end of the deposition (B) the (1/2,0) peak disappears and the (1/3,0) peak appears, which is a fingerprint, that there is a 3-fold periodicity along the [1 0] direction.

4.4.3 Conclusion.

From the data presented in this section we can conclude that both p-Toluidine and 1,4-Benzenediamine adsorb more strongly on Au(110) than on Au(111). The Nitrogen K-edge NEXAFS spectra for submonolayer or monolayer of both molecules on Au(110) present the broad peak at 400eV, that in the previous section was attributed to molecules bound to the surface with the amino group. The N 1s XPS spectra of the molecules bound on Au(110) are characterized by two distinct peaks at 398.8 eV and 399.9 eV, while on Au(111) there is only a single N1s XPS peak at 399.6 eV. This difference can be explained by taking into account that Au(110) is composed by surface atoms having coordination equal or lower with respect to Au(111) and, as already mentioned, recent calculations have shown that amines bind preferentially on low coordinated gold atoms [9], as the ones on the Au(110). Therefore on Au(110) more adsorption sites are allowed.

4.5 RPES: molecule-surface interaction.

The role of the molecule-metal interface is clearly a key issue in molecular electronics. In particular the spatial configuration of the molecules adsorbed and the orientation and modification upon adsorption of the molecular orbitals determines the charge transfer. Wang et al. [28], as an example, showed that for 4-fluorobenzenethiol monolayers on Au(111) there is a configuration dependent ultrafast electron transfer that directly reflects the delocalization of molecular orbitals for molecules standing up or lying down. The molecular orbitals experience a localization-delocalization transition resulting from hybridization between them and the metal surface.

In this section the charge-transfer characteristics of the system molecule-gold surface is studied by means of Resonant Photoemission Spectroscopy (RPES). As already discussed in chapter 2, this technique is based on the identification of electron emission decay channels (nonradiative decay) following resonant excitation of core level electrons (C1s in our case) into unoccupied molecular states (LUMO+n, $n \geq 0$). In this chapter the unoccupied molecular orbitals will be named as LUMO+n, $n \geq 0$ and the occupied molecular orbitals as HOMO-n, $n \geq 0$, where LUMO+0 (or LUMO) and HOMO+0 (or HOMO) are respectively the Lowest Unoccupied Molecular

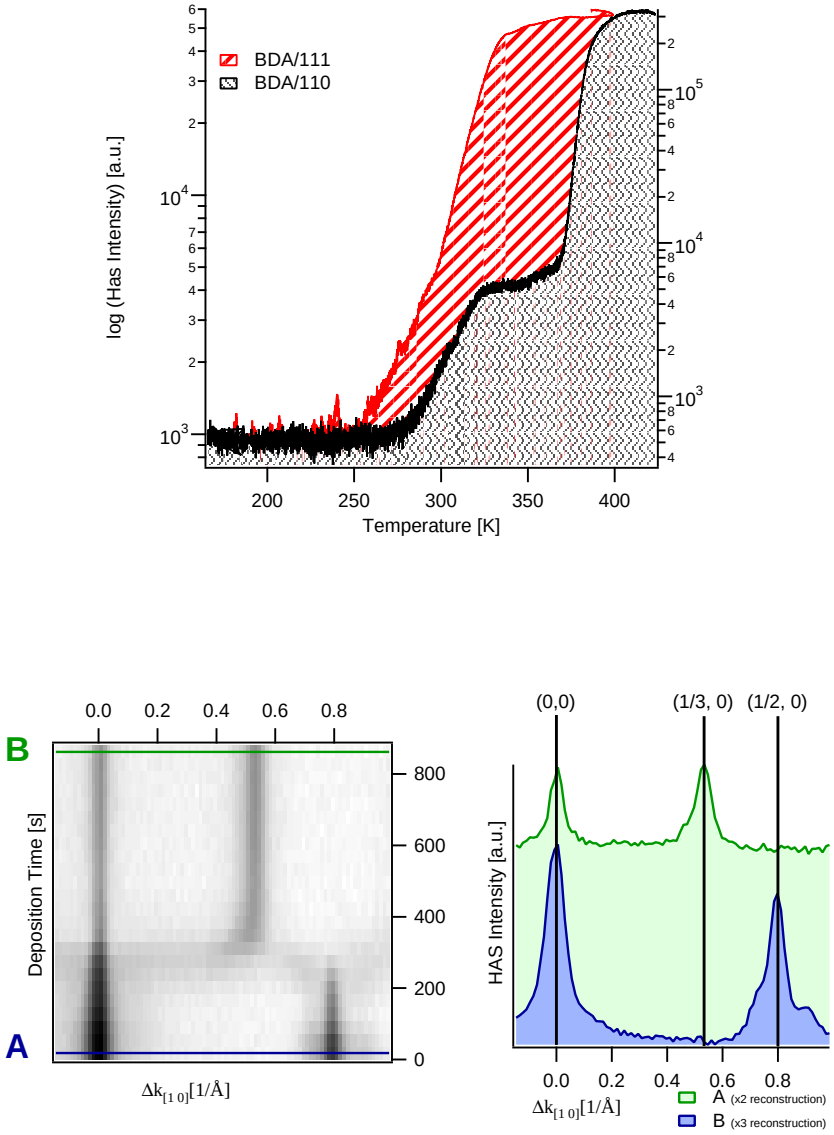

Figure 4.16: Top graph. HAS specular intensity during desorption of multilayers of 1,4-BDA grown on Au(110) and on Au(111). Bottom left. Change of the diffraction pattern taken along the [1 0] direction while depositing molecules with the sample at 330K. In the abscissa is reported the momentum exchanged and in the ordinate is reported the deposition time. Each cut at fixed deposition time of this image is a section of the reciprocal space along the [1 0] direction. Bottom right. Profiles of the image on the left corresponding to diffraction scans at almost the beginning (A) and the end (B) of the deposition.

Orbital and the Highest Occupied Molecular Orbital.

As underlined in chapter 2, a participator decay (fig. 2.8) can occur only if three conditions are satisfied:

1. the photon energy allows the transition from the core level (C1s) to the empty molecular state (LUMO+n, n $\geq$ 0). This is the usual XAS event and is governed by the dipole selection rule.

2. the decay, that takes place through non radiative Auger emission, requires a spatial overlap among the involved wavefunctions of the core level (ψ_{core}), the occupied state ($\psi_{\text{HOMO-n}}$) and the empty state ($\psi_{\text{LUMO+n}}$).

3. the molecules should not be strongly coupled with the substrate (or to each other), otherwise it is possible that the core-excited electron is transferred to the conduction band of the substrate within the core hole lifetime, therefore resonant decay channels are quenched and the excited state can only decay via normal non resonant Auger process. Such a quenching of participator channels is recognized in the diminished intensity of RPES-related spectral features of molecular adsorbates.

Starting from a multilayer of molecules, under the hypotheses that intermolecular electron hopping is significantly slower than the core hole decay, we can identify in a combined way the HOMO-m state in the valence band (VB) and the transition to the LUMO+n state in the NEXAFS spectra. In fact resonating spectral features in the VB spectrum (HOMO-m) in correlation with NEXAFS absorption peaks (LUMO+n) occur only if point 1 and 2 are satisfied, that means that the filled state wavefunction ($\psi_{\text{HOMO-m}}$, m $\geq$ 0) is spatially located close to the core site (ψ_{core}) and so must be also the LUMO+n wavefunction ($\psi_{\text{LUMO+n}}$).

The top left image of fig. 4.17 is the measured carbon K-edge RPES of a multilayer of 1,4-BDA. On the abscissa the electron binding energy is reported, while on the ordinate the photon energy. Each cut at fixed photon energy of this image is a VB spectrum. In the graph on the top right is reported the carbon K-edge NEXAFS spectrum (black solid line) acquired simultaneously with the RPES.

It is evident that some states in VB resonate when measured with photon energies corresponding to the two sharp features of the NEXAFS spectrum, that are transitions to LUMO+m states. In the bottom right graph of fig. 4.17 the fit of each VB spectrum in the RPES measurement is reported performed by using the minimum number of peaks required for a good fit in the pre-resonance and post-resonance region. Their relative positions with

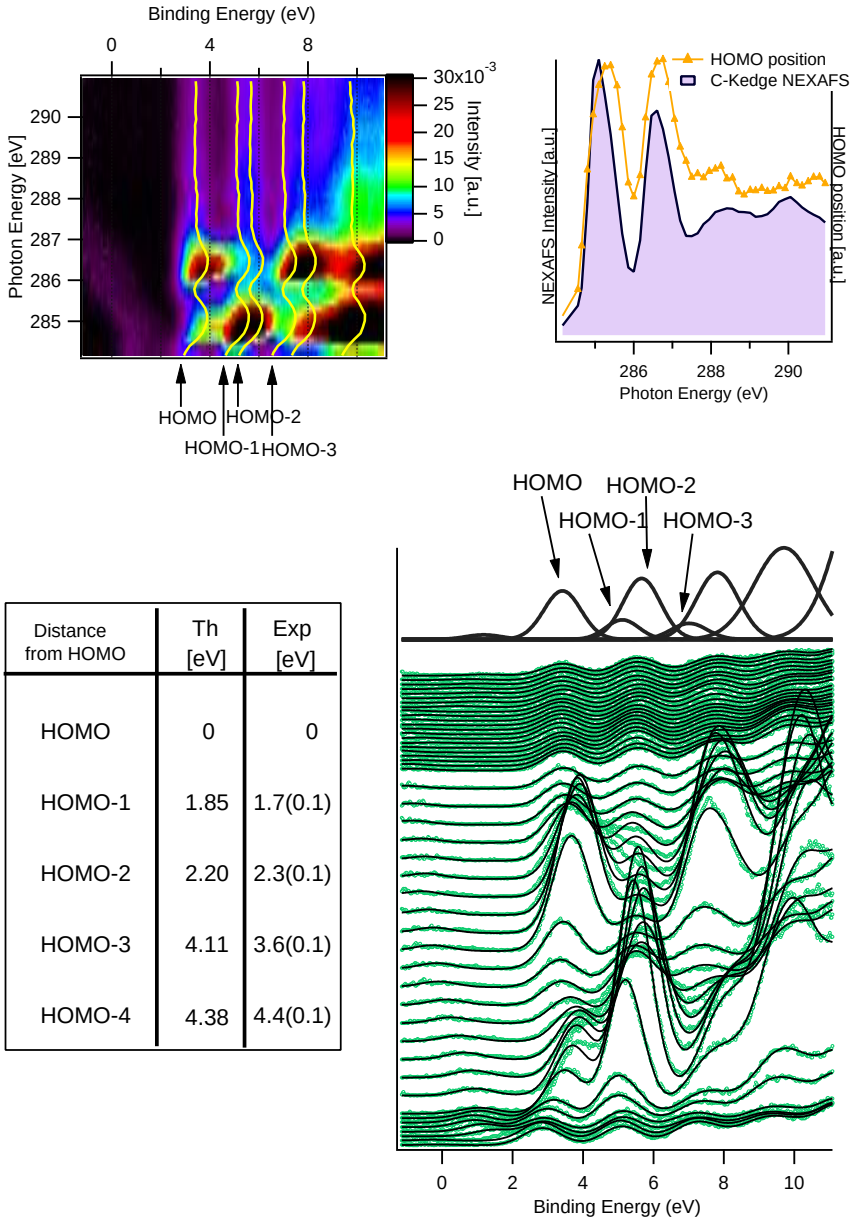

Distance from HOMO	Th [eV]	Exp [eV]
HOMO	0	0
HOMO-1	1.85	1.7(0.1)
HOMO-2	2.20	2.3(0.1)
HOMO-3	4.11	3.6(0.1)
HOMO-4	4.38	4.4(0.1)

Figure 4.17: Top left: Carbon K-edge RPES of a multilayer of 1,4-BDA. The abscissa is the binding energy, the ordinate is the photon energy and the color scale is the intensity. Each cut at fixed photon energy is a valence band spectrum. The yellow lines are the positions obtained from the best fit of the HOMO-m states for each valence band spectrum. Top right: Carbon K-edge NEXAFS spectrum measured simultaneously with the RPES. On the same graph is also reported the variation of the position of HOMO for each photon energy. Bottom left: Energy position of the HOMO-n peaks with respect to the HOMO from the experimental data (Exp) and calculated ones (Th). Bottom right: Fit of the RPES. The dotted green lines are the measured valence band spectra, while the black solid lines are the fitting curves.

respect to the HOMO identified in the fitting procedure are reported in the table of fig. 4.17, together with the values obtained from a calculation for a gas phase molecule (RHF performed with GAMESS code). The calculated relative positions are close to the experimental ones. The width and the relative positions of the peaks in the fit have then been kept fixed and their intensity variation with the photon energy has been followed. It should be noted that the position of the first HOMO was not constrained, and as indicated in the top right graph, it follows the NEXAFS signal: this can be due to charging effects. The fit does not work well for the resonating spectra, while it is quite good out of resonances. This can be related to several reasons. First, since there is some charging, the shape of the peaks can change. Second, it is possible, if the film is not thick enough, to have some contributions from the monolayer which can give a different contribution to the spectra. Third, on resonance it is possible to have spectator Auger decay or Auger decay from HOMO-1. This corresponds to new peaks on the resonating spectra that are underestimated by the fit. With the fitting procedure used, we take into account only of the contributions from the participator Auger decay.

After having performed the best fit, it is possible to look at the intensity variations for each HOMO-n with respect to the photon energy, as reported in the top graph of fig. 4.18. In the bottom graph of fig. 4.18 the isosurface plot of the charge density for the first HOMOs and LUMOs is reported, which provides a visualization of the orbital geometry. Assuming that the molecular orbitals are similar to the ones in the gas phase, the conditions for resonance are met if the nth-HOMO spatially overlaps the mth-LUMO. The spatial overlap, judged in a qualitative way, is reported as the color scale of the filled circles of fig. 4.18: where black means high overlap. Therefore LUMO resonates mainly with HOMO-1 and LUMO+1 with HOMO and HOMO-3.

It is important for the following discussion to note that the assigned LUMO is localized mostly on the carbon atoms of the benzene ring not attached to the amino groups in contrast to the LUMO+1.

The same procedure can be applied to the p-toluidine multilayer as shown in fig 4.19 and 4.20. The geometry of the calculated molecular orbitals in this case is similar to the BDA, but the substitution of one amino group with one methyl group produces a split of LUMO+1 with respect to the BDA, since the initial state for the two carbons bound with the methyl and the amino groups are different. In XPS they are separated by about 1 eV (see fig. 4.5).

The interaction of the molecule with the surface can induce changes in the RPES. Some participator channels can be quenched if the excited electrons are quickly transferred to the metal before the usual decay, which results in a diminished intensity with respect to the multilayer and the gas-phase

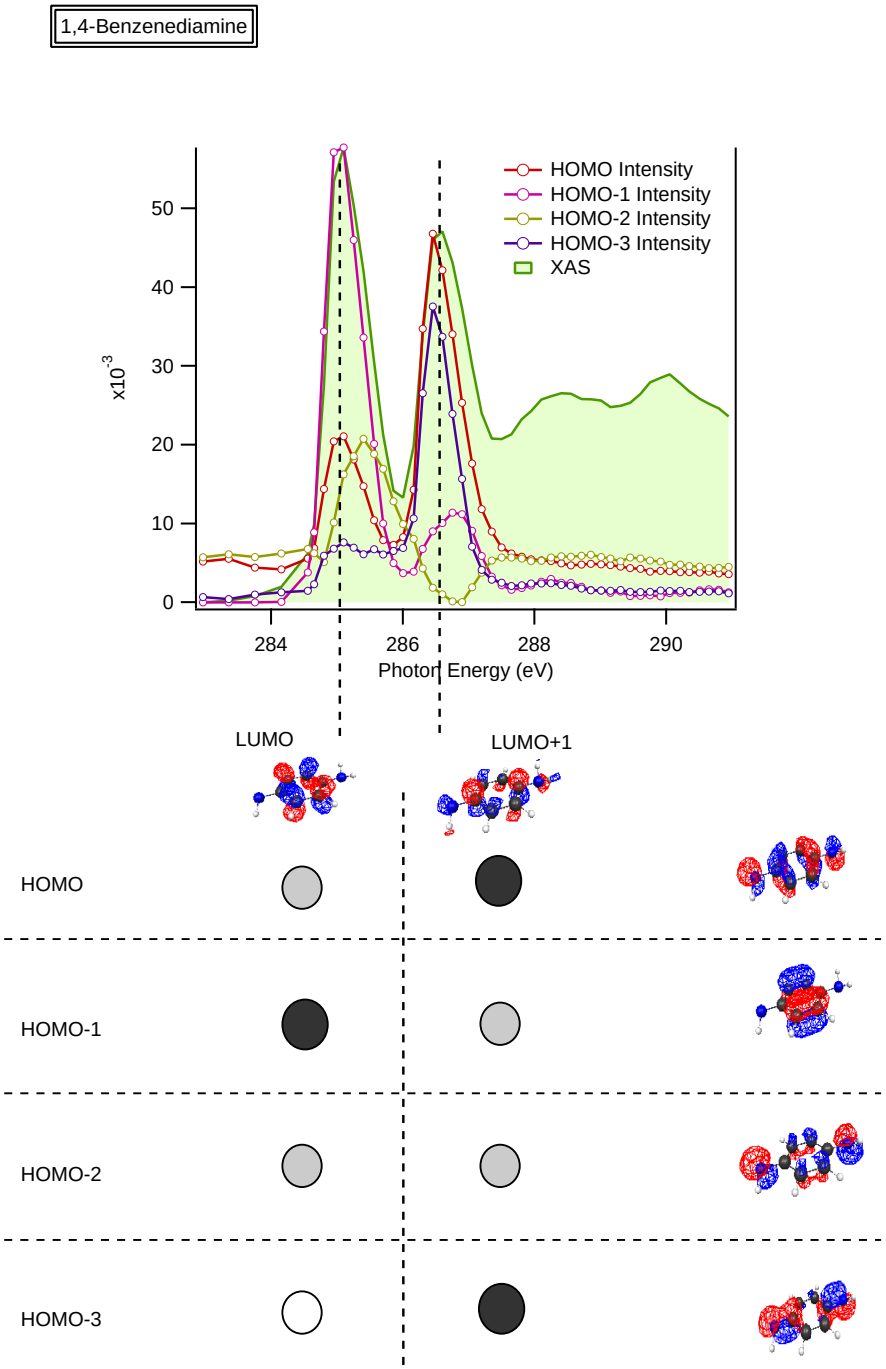

Figure 4.18: Top graph: Intensity variation of the fitted HOMO-n (n= 0, 1, 2, 3) as a function of the photon energy. On the same graph is also reported the NEXAFS spectrum. Bottom graph: Isosurface plot of the charge density of the first LUMOs and HOMOs obtained from calculations for gas phase molecules. The white, gray and black circles identify the overlap among each LUMO and HOMO: black means high overlap.

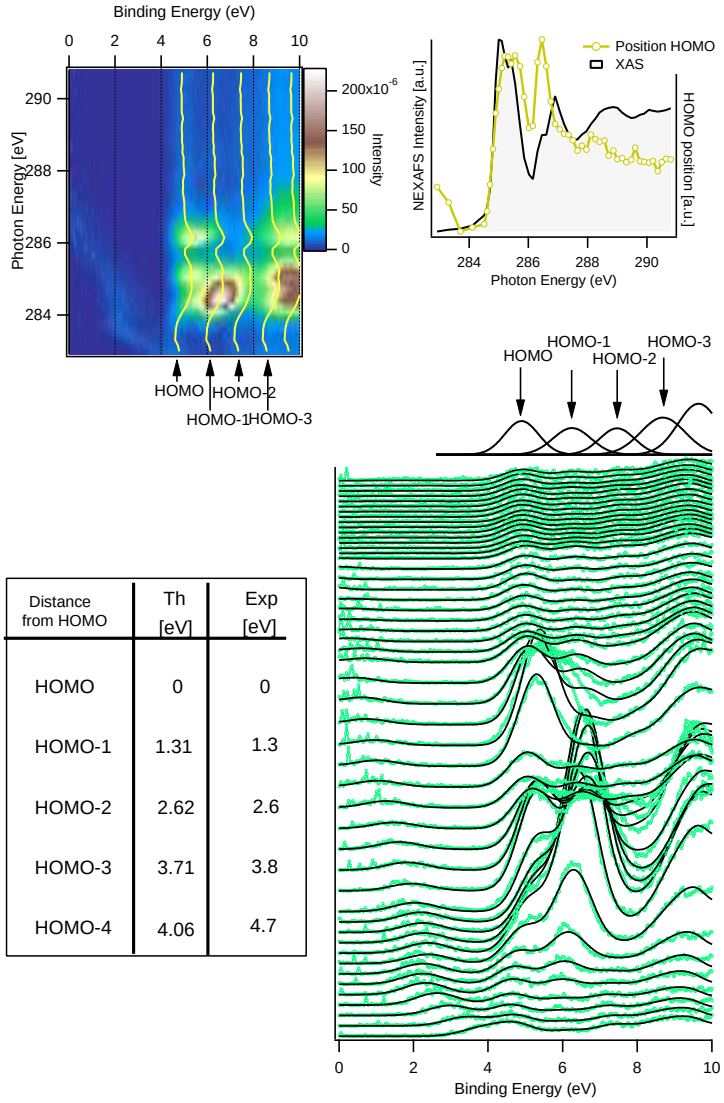

Distance from HOMO	Th [eV]	Exp [eV]
HOMO	0	0
HOMO-1	1.31	1.3
HOMO-2	2.62	2.6
HOMO-3	3.71	3.8
HOMO-4	4.06	4.7

Figure 4.19: Top left: Carbon K-edge RPES of a multilayer of p-toluidine. The abscissa is the binding energy, the ordinate is the photon energy and the color scale is the intensity. Each cut at fixed photon energy is a valence band spectrum. The yellow lines are the positions obtained from the fit (as described in the text) of the HOMO-m states for each valence band spectrum. The peak at binding energy in the range 0-4 eV is the C 1s photomession with photon energy double with respect to the selected one. It scales linearly with the photon. In this plot this is not the case since the points ordinate axis are not equally spaced. Top right: Carbon K-edge NEXAFS spectrum measured simultaneously with the RPES. On the same graph is also reported the variation of the fitted position of HOMO for each photon energy and it scales as the NEXAFS. Bottom left: Energy position of the HOMO-n peaks with respect to the HOMO from the experimental data (Exp) and calculated ones (Th). Bottom right: Fit of the RPES. The dotted green lines are the measured valence band spectra, while the black solid lines are the fitting curves.

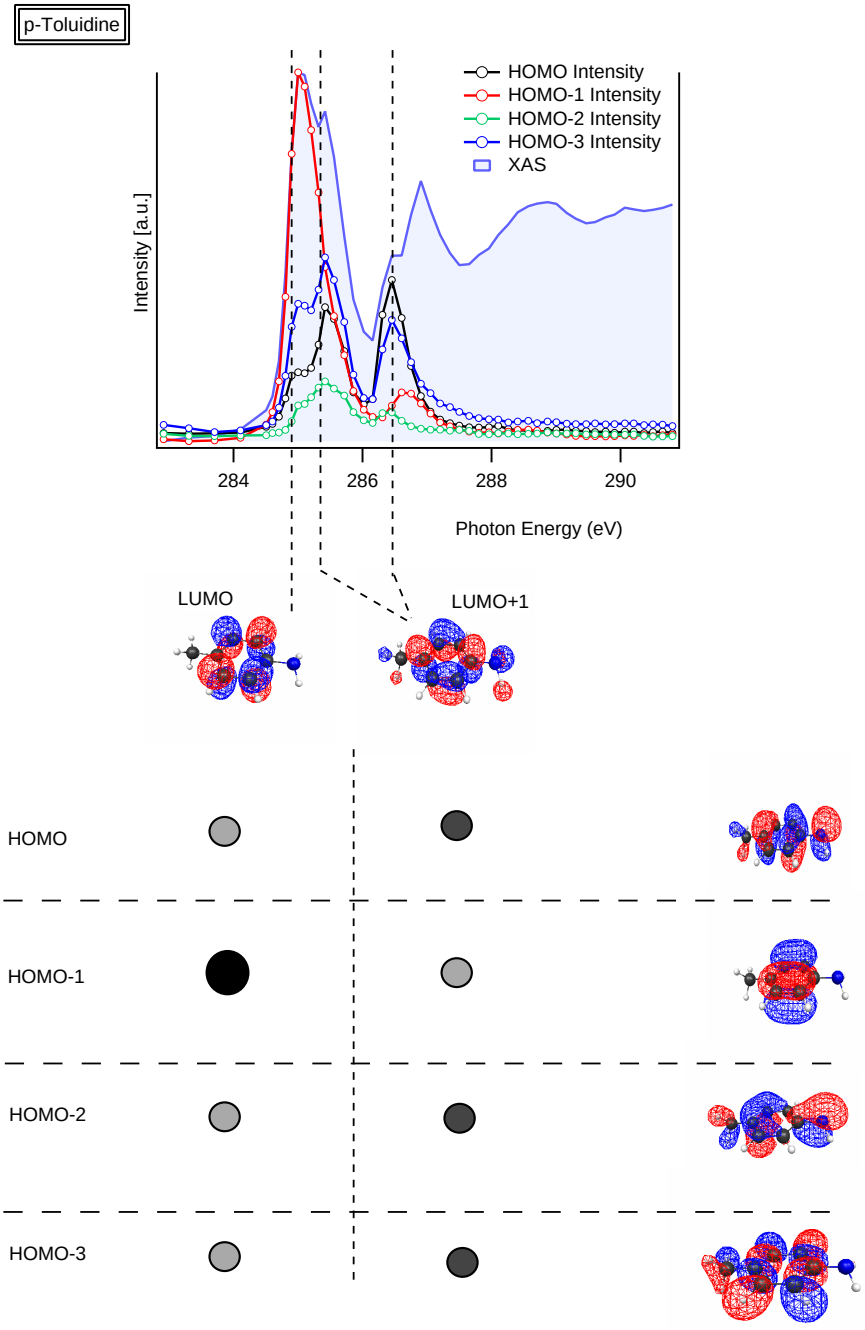

Figure 4.20: Top graph: Intensity variation of the fitted HOMO-n (n= $0, 1, 2, 3$) as a function of the photon energy. On the same graph is also reported the NEXAFS spectrum. Bottom graph: Isosurface plot of the charge density of the first LUMOs and HOMOs obtained from calculations for gas phase molecules. The white, gray and black circles identify the overlap among each LUMO and HOMO: black means high overlap.

of RPE-related spectral features of molecular adsorbates. In figure 4.21 the Carbon K-edge RPES of a multilayer (top left) and a monolayer (top right) of flat BDA molecules on Au(111) are reported. By comparing the two measurements it is evident that:

- the HOMO-m states in the monolayer are shifted towards lower binding energy with respect to the multilayer, and follow as well the resonances. This shift can be explained within the image charge model by taking into account the different distances in the monolayer and multilayer of the molecules from the surface.

- the shift of the HOMOs going from the multilayer to the monolayer is not a rigid shift, but the relative positions of the HOMO states change. This can be due to modifications of the molecular orbitals due to bonding to the surface even if the interaction of the molecule with the surface is very weak.

It is therefore difficult to compare directly the intensity variations of the HOMO states of the multilayer with the ones of the monolayer, without knowing their modifications from calculations. However it is possible to follow another way to study the charge transfer from a qualitative point of view. This can be measured by comparing the NEXAFS signal, that measures the probability to promote a core electron into an unoccupied state, and the NEXAFS-RESPES signal. In order to explain how to obtain the last quantity one has to think at the RPES in the following way: for each photon energy we are measuring a valence band spectra, that means for each photon energy we are collecting electrons. If for each photon energy we sum all the electron measured from the Fermi level up to a certain binding energy (S), we obtain a partial yield NEXAFS with the cut-off given by S. In the following we will call the NEXAFS obtained with this procedure NEXAFS-RPES. In the usual partial yield NEXAFS at the carbon K-edge the cut-off used is 245 eV, meaning that we are collecting electrons in the region from zero up to 30-40 eV. If in the NEXAFS-RPES some peaks present in the NEXAFS disappear or their ratio with others is changed, this is the evidence that charge transfer had occurred.

The spectra on the bottom of figure 4.21 are the NEXAFS (solid blue curve) measured in parallel with the RPES and the NEXAFS-RPES (dotted green and red curves) obtained by integrating the RPES over different BE windows with cut-offs S1=16eV and S2=10eV. It is clear that the cut-off should be large enough to include some resonant features, otherwise the measurement is only a NEXAFS from just one transition. By using the same energy window on the monolayer and on the multilayer, in the monolayer the

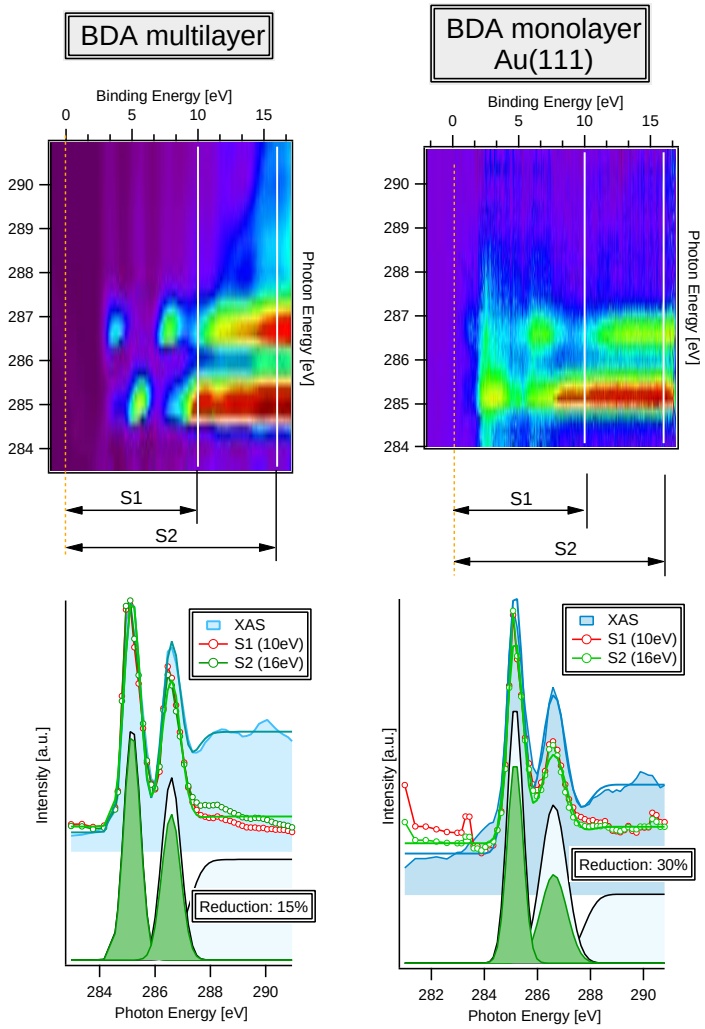

Figure 4.21: Top left: Carbon K-edge RPES of a multilayer of 1,4-BDA. Top right: Carbon K-edge RPES of a monolayer of flat 1,4-BDA on Au(111). Bottom left: NEXAFS (XAS trace) and NEXAF-RPES at two different cut-offs (S1 and S2) of the multilayer of 1,4-BDA. At the bottom are reported also the peaks used for fitting the two curves. Bottom right: NEXAFS (XAS trace) and NEXAF-RPES at two different cut-offs (S1 and S2) of the monolayer of 1,4-BDA on Au(111). At the bottom are reported also the peaks used for fitting the two curves.

ratio between LUMO and LUMO+1 in the NEXAFS-RPES with respect to the NEXAFS exhibits a bigger variation (30% vs 15%) than the multilayer.

At this point, I have to clarify the procedure used to scale the NEXAFS and NEXAFS-RPES spectra in figure 4.21. In general it is possible to have charge transfer to the substrate from all the unoccupied states once populated, but in some particular cases [28, 29] the NEXAFS-derived LUMO, that is a core excited state, can shift below the Fermi level due to the presence of the core-hole. In that case charge transfer is not anymore allowed in the core excited state and it is possible to normalize all the spectra at the LUMO intensity. Unfortunately in our cases the LUMO excited peaks are always above the Fermi level, and that charge transfer is always energetically allowed even from these states. We have chosen to scale the spectra in such a way no NEXAFS-RESPES features goes above the NEAXFS since the number of electrons collected with 10eV cut-off should be less than 30-40eV cut-off.

In the figure 4.21 the NEXAFS and NEXAFS-RPES spectra were fitted by using only two gaussian (one for each LUMO) and an edge. Going from the multilayer to the monolayer the ratio between the intensities of the peaks corresponding to transitions to LUMO and LUMO+1 states had changed. This means that charge transfer occurs in the monolayer of flat 1,4-BDA on Au(111). Moreover LUMO+1 exhibits the stronger decrease and as we already have observed it is localized on the carbons bounded to nitrogen. This could mean that there is a fast charge transfer to the substrate from orbitals localized on the nitrogen. We cannot exclude that also the carbon atoms bounded to other carbon atoms have a contribution in the charge transfer, but it is faster on LUMO+1 with respect to LUMO. In conclusion the amino group plays a central role in the transfer of the charge to the substrate. We will be back on this point in the next section.

The same analysis can be applied to the p-toluidine layers. In figure 4.22 the carbon K-edge RPES of a multilayer of p-toluidine and of a sub-monolayer of p-toluidine on Au(111) and on Au(110) are reported. The assignment of the HOMOs and LUMOs for the multilayer has been already described in figure 4.20. As for 1,4-BDA the positions of the HOMOs (and therefore of the resonances) in the monolayer and sub-monolayer are shifted towards lower binding energy with respect to the multilayer. Consistently with the image plane model the shift is bigger for Au(111) than for Au(110). Moreover the relative intensities of the resonances is clearly different in the three cases. In the multilayer case, for all the selected binding energy windows, given by the cut-off S, there is no change in the ratio of the LUMO and LUMO+1 between the NEXAFS and the NEXAFS-RPES. However changes are evident by choosing the same energy windows for the films on Au(111) and Au(110).

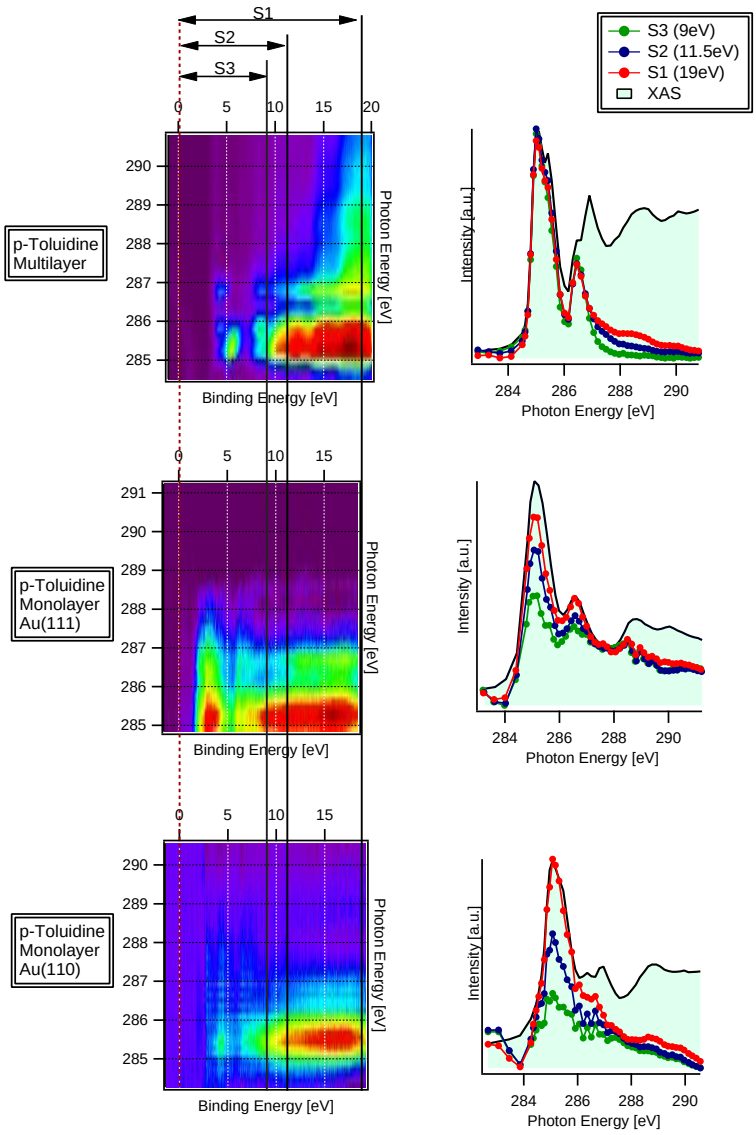

Figure 4.22: Top left: Carbon K-edge RPES of a multilayer of p-toluidine. Top right: NEXAFS (XAS trace) and NEXAFS-RPES at three different cut-offs (S1, S2 and S3) of the multilayer of p-toluidine. Middle left: Carbon K-edge RPES of a monolayer of flat p-toluidine on Au(111). Middle right: NEXAFS (XAS trace) and NEXAFS-RPES at three different cut-offs (S1, S2 and S3) of the monolayer of p-toluidine on Au(111). Bottom left: Carbon K-edge RPES of a layer of p-toluidine on Au(110). Bottom right: NEXAFS (XAS trace) and NEXAF-RPES at three different cut-offs (S1, S2 and S3) of the layer of p-toluidine on Au(110).

In both cases, as already underlined, the normalization is performed in such a way the NEXAFS-RPES is always less than the NEXAFS, which can lead to an overestimation of the charge transfer. Charge transfer is taking place for both the orbitals on the two surfaces, but the ratio between LUMO and LUMO+1 changes with respect to the multilayer: on both cases LUMO+1 is reduced and on Au(110) the reduction is stronger. As for BDA, the main difference between LUMO and LUMO+1 is that LUMO+1 contains some contributions from the carbon atoms attached to the nitrogen. The changes in the RPES can indicate a strong modification of the orbitals at least partially localized on the nitrogen upon adsorption, and again are an indication that charge transfer to the substrate takes place through orbitals involving the amino group.

We can conclude that for both molecules the amino group is deirectly involved in transferring the charge to the substrate.

4.6 Energy level alignment.

In this section I will analyze the relationship between the results presented in section 4.5 and the theoretical description of molecular conductance usually employed to explain conductance experiments.

In the introduction to this chapter, I have already underlined that, from a qualitative point of view, in order to understand the flow of current through molecules, several ingredients are needed. Three among them that are very important are [35]:

1. an energy level diagram showing the molecular energy levels relative to the Fermi energy in the metallic contacts;

2. an estimate of the broadening of molecular levels due to coupling to the contacts;

3. the spatial profile of the applied potential under bias.

I will remember here that the energy level alignment in the junction is not just the alignment of the metallic work functions of the contacts and the ionization potential or electron affitinity of the molecule with respect to the vacuum level, in fact several factors can produce shifts in the positions of the levels of the molecule with respect to the ones of the electrodes, for example due to the presence of interfaces [32]. An important point is that the broadening (Γ) of the molecular levels due to coupling to the contacts is related to the time τ it takes for an electron placed in a level to escape into the contact ($\Gamma = \frac{\hbar}{\tau}$), or in other words is the rate at which electrons

are injected into the level from the contact. Γ in fact could be different for different energy levels.

These ingredients are the basis for most of the theoretical descriptions of molecular conduction or, more generally, of the current-voltage characteristics of a metal-single molecule-metal junction. In the following I will briefly describe the fundamental equations employed, more details can be found in [35, 36, 37]. In general all the theoretical approaches use variants of the Landauer formula [39].

Landauer's formula was historically obtained for a system of two one-dimensional leads connecting two macroscopic electrodes (electron reservoirs) via a scattering object or a barrier characterized by a transmission function $\mathcal{T}(E)$. The zero temperature conductance, measured as the limit $\Phi \to 0$ of the ratio I/Φ between the current and the voltage drop between the reservoirs, is

$$g = \frac{e^2}{\pi\hbar}\mathcal{T}(E)(E_F)$$

with E_F the Fermi Energy of the electrodes and the conductance of an ideal one-dimensional lead is therefore $g_0 = \frac{e^2}{\pi\hbar} = 12.9\ \mathrm{K}\Omega^{-1}$.

In cases where the leads have finite size in the direction normal to the propagation, so that they support traversal modes, the current for a voltage difference Φ between the electrodes is given by

$$I = \int_0^{+\infty} dE[f(E) - f(E + e\Phi)]\frac{g(E)}{e}$$

$$g(E) = g_0 \sum_{i,j} \mathcal{T}(E)_{ij}(E)$$

where f(E) is the Fermi distribution in the electrodes and $\mathcal{T}(E)_{ij}$ is the probability that a carrier coming from the left, say, of the scatterer in traversal mode i will be transmitted to the right into transversal mode j. The sum is performed over all traversal modes whose energy is smaller than E_F.

It is possible to replace the expression based on transmission coefficients $\mathcal{T}(E)$ by an equivalent expression based on scattering amplitudes, or T matrix elements, between zero order states localized on the electrodes [36]:

$$\sum_{i,j} \mathcal{T}_{ij}(E) = 4\pi^2 \sum_{l,r} |T_{l,r}|^2 \delta(E - E_l)\delta(E - E_r).$$

In the previous formula (i,j) denotes a scattering state of energy E, characterized by an incoming state i on the left electrode and an outgoing state j on the right electrode. On the right side of the equation, l and r denote zero-order states confined to the left and right electrodes, respectively. T is

the corresponding transition operator whose particular form depends on the details of the confinement.

If we consider a molecular junction where the coupling between the metal electrodes is weak, than it is convenient to write the system's Hamiltonian as the sum $H = H_0 + V$ of a part H_0 that represents the uncoupled electrodes and spacer and the coupling V between them. In the weak coupling limit the T operator

$$T(E) = V + VG(E)V$$
$$G(E) = (E - H + i\epsilon)^{-1}$$

is usually replaced by its second term only. The first direct term in fact can be disregarded if we assume that V couples the states l and r only via states of the molecular spacer. In the previous formulas was used the Non-equilibrium Green's Function Formalism (NEGF). This is because it allows to deal with multiple levels with arbitrary broadening as in the case of molecules [35].

In literature the low bias conductance through polyphenyls attached to gold electrodes via amine end groups has been described as a non resonant tunneling process or superexchange [5]. This is a simple theoretical model which relies on a single electron (hole) picture in which the donor-bridge-acceptor (DBA) system, that is the metal-molecule-metal junction, is represented by a set of N levels [40]. This bridge levels do not couple to the thermal environment and their energies have to be high relative to the energy of the transmitted electron. Site 1 of the bridge is attached to the left electrode and site N to the right electrode, therefore

$$T_{l,r} = V_{l1} G_{1N} V_{Nr}.$$

At zero temperature this leads to [36]

$$\sum_{i,j} \mathcal{T}_{ij}(E) = |G_{1N}(E_F)|^2 \Gamma_1^{(L)}(E_F) \Gamma_N^{(R)}(E_F)$$

therefore

$$I(\phi) = \frac{e}{\pi\hbar} \int_{E_F - e\Phi}^{E_F} dE |G_{1N}(E, \Phi)|^2 \Gamma_1^{(L)}(E) \Gamma_N^{(R)}(E + e\Phi).$$

G_{1N} is an element of the reduced Green's function in the bridge's subspace obtained by projecting out the metals' degrees of freedom

$$G = (E - H_b - \Sigma_b(E))^{-1}.$$

Here $H_b = H_b^0 + V_b$ is the Hamiltonian of the isolated-bridge entity in the basis of eigenstates of H_b^0:

$$H_b^0 = \sum_{n=1}^{N} E_n |n><n|;$$

$$V_b = \sum_{n=1}^{N}\sum_{m=1}^{N} V_{n,m}|n><m|;$$

$$\Sigma_{nm}(E) = \delta_{n,m}(\delta_{n,1}+\delta_{n,N})[\Lambda_n(E) - (1/2)i\Gamma_n(E)];$$

$$\Gamma_n(E) = 2\pi\sum_l |V_{ln}|^2\delta(E_l - E) + 2\pi\sum_r |V_{rn}|^2\delta(E_N - E)$$

$$\equiv \Gamma_n^{(L)}(E) + \Gamma_n^{(R)}(E);$$

$$\Lambda_n(E) = \frac{PP}{2\pi}\int_{-\infty}^{\infty} dE' \frac{\Gamma_n(E'}{(E-E')}$$

The transmission problem is thus reduced to evaluating a Green's function matrix element and two width parameters.

This equations can look quite complicate, but the important point here is that in order to solve them it is needed to identify an appropriate Hamiltonian matrix H_b to describe the molecule and the two contacts and to compute the self-energy matrices Σ that account for the effects of the contacts on the molecule.

Several theoretical approaches including ab initio or semi-empirical methods have been used in literature to solve the Hamiltonian problem. A recently developed theoretical model of nanoscale transport (in ref. [30]) relies on a Landauer approach, simplified to treat electronic interactions at a mean field level within density functional theory (DFT). The calculations in this case are performed in two steps: first the geometry and the energy levels of the molecule in the junction are calculated and then the conductance is derived by using the Landauer formula. We will see later that the computed conductances derived with this approach do not match the measured ones. In general it is well known that the DFT suffers the problem of the inherent inaccuracy of the computed LUMO energy and wavefunctions. In this specific case the approximations used introduce errors also in the determination of the positions of the filled energy levels.

However by using this theoretical approach [30], Venkataraman et al. [31, 38] predicted and measured some general trends in the conduction of simple families of amino terminated molecules sandwiched between Au electrodes. In particular they measured the conductance of a series of substituted benzene diamine molecules (shown in the table of fig. 4.23) with the STM break junction technique. The measured values are reported as a function of the calculated gas phase ionization potential of the molecule in the bottom panel of fig. 4.23 taken from [30]. All the studied molecules have the same N-N distance, therefore once the N-Au contact has been established, all of them have the same length. It can be shown [35] that in a donor-bridge-acceptor system as long as the metal Fermi level or equivalently the donor

and acceptor levels are far enough from the molecular levels (HOMO and LUMO), the electron tunneling rate decreases exponentially with increasing molecule length (L) and the measured low bias conductance scales as $\exp^{-\beta L}$. The decay constant β depends on the intrinsic properties of the molecules in the junction and in first approximation it depends on the energy separation between Fermi and the closest molecular level. Since for the measured series, the conductance varies inversely with the calculated ionization potential of the molecules (in the gas phase), the authors in [30] concluded that the occupied states are closest to the gold Fermi level with respect to the unoccupied ones and the conduction takes place through HOMO. This conclusion was

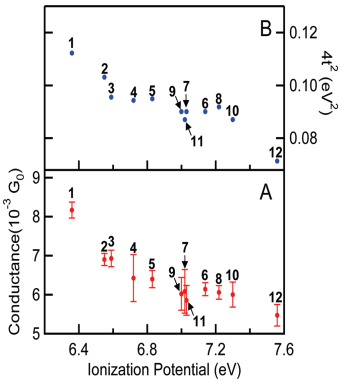

no.	molecule name
1	tetramethyl-1,4-diaminobenzene
2	2,5-dimethyl-1,4-diaminobenzene
3	2-methoxy-1,4-diaminobenzene
4	2-methyl-1,4-diaminobenzene
5	1,4-diaminobenzene
6	2,5-dichloro-1,4 diaminobenzene
7	2-bromo-1,4-diaminobenzene
8	trifluoromethyl-1,4-diaminobenzene
9	2-chloro-1,4-diaminobenzene
10	2-cyano-1,4-diaminobenzene
11	2-fluoro-1,4-diaminobenzene
12	tetrafluoro-1,4-diaminobenzene

Figure 4.23: (A) Measured conductance values against the calculated ionization potential for the series of the 12 molecules reported in the table on the right. (B) Square of the calculated tunnel coupling ($4t^2$) against the calculated ionization potential. Image from ref.[31].

supported by theoretical calculations: in the upper panel of the figure 4.23 the calculated $4t^2$ as a function of the calculated gas phase ionization potential is reported. The calculation [38] is performed by considering the bridge in the donor-bridge-acceptor system as composed by one molecule with attached one gold atom on each amino termination. This bridge entity is then coupled to the Au electrodes. For simplicity only the Au s orbitals and the two nearest relevant orbitals on the diamine were considered. Another approximation was applied on the self-energy by considering only a constant imaginary part Γ. It was then derived that:

$$T(E) \propto \frac{4(2t)^2}{\Gamma^2}$$

with

$$2t \approx \frac{2\tau^2(E_{LUMO} - E_{HOMO})}{(E_{LUMO} - E)(E - E_{HOMO})}.$$

In this equations τ is the coupling of the molecule to one Au atom, while Γ is the coupling of the bridge entity to the electrodes. Therefore $4t^2$ in figure 4.23 is proportional to the conductance. The trend of the calculated conductance values matches well the experimental values.

This conclusion is derived by considering the calculated gas phase ionization potential of the molecules, but as we have underlined at the beginning of this chapter the energy level alignment in the junction can be different. We have measured by means of Ultraviolet Photoemission Spectroscopy (hv=21.2 eV) the valence band spectra of the multilayer and monolayer of three molecules of the series in fig.4.23, in particular n.1 (TMBDA), n.5 (BDA) and n.12 (4F-BDA) (fig. 4.3). In fig 4.24 are reported the UPS measurements on the multilayers of BDA and TMBDA. They were grown by depositing 100 Langmuir at 200 K. For 4F-BDA it was not possible to grow any stable multilayer at the temperatures that can be reached with our cooling system. The HOMO energies of the two molecules with respect to the Fermi energy of the substrate follow the same behavior of the gas phase IP ($E^{TMBDA}_{HOMO} < E^{BDA}_{HOMO}$).

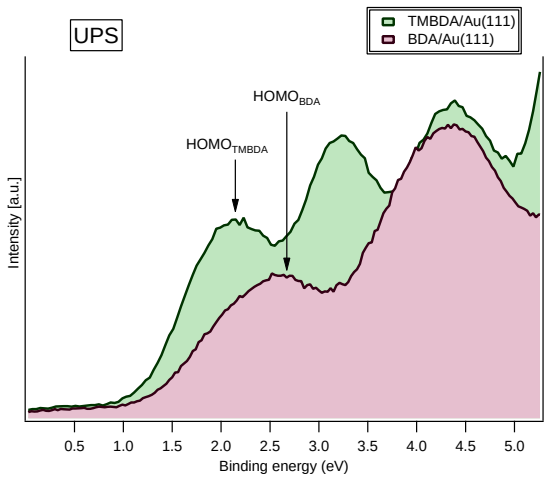

Figure 4.24: UPS (hv=21.2 eV) spectra of a multilayer of BDA and of TMBDA. The arrows identify the positions of the HOMOs for the two layers.

The alignment of the energy levels of the molecule in the junction for sure will be different than in the multilayer or in the monolayer of molecules on the surface, but we expect that for different molecules the shifts of the

positions of the energy levels will follow the same trend in the junction and in the monolayer case. The UPS spectra for monolayer or sub-monolayer depositions of the three molecules on Au(111) are reported in figure 4.25.

While for TMBDA and 4F-BDA an HOMO peak is clearly visible, this is not the case for BDA. In order to determine its energy position we have used the Carbon K-edge RPES, as shown in fig. 4.26. The energy position of the HOMO was determined by subtracting the Valence Band spectra on resonance with the one out of resonance and by fitting the residual with a Gaussian. The energy positions of the HOMO determined are summarized in the following table:

Molecule	HOMO position from UPS	HOMO position from RPES
TMBDA	0.9 ± 0.1 eV	1.2 ± 0.3 eV
1,4-BDA	1.4 ± 0.1 eV	1.6 ± 0.5 eV
4F-BDA	1.5 ± 0.1 eV	-

The differences between the values measured with UPS and the ones obtained from the RPES for each molecule can be related to several factors: first of all the procedure of subtraction of the spectra can introduce errors, therefore the error bars are quite large. Second the alignment of the binding energy scale in the RPES Valence Band spectra is performed by aligning the $Au_{4f_{\frac{7}{2}}}$ peak measured simulateously at the literature reference value. The measured XPS Au_4f peak was fitted with a Gaussian. However the position reported in literature was measured on a clean surface, where the peak contains two components one from the bulk and one from the surface [41]. Once the molecules are adsorbed on the surface the ratio between this two components can change and by fitting the peak with just a Gaussian we can introduce an error. The sequence for the HOMO positions in the monolayers is therefore:

$$E_{HOMO}^{TMBDA} > E_{HOMO}^{BDA} > E_{HOMO}^{4F-BDA}.$$

In writing this sequence we have fixed the binding energy scale as increasing going from the HOMO to the LUMO and the zero is set at the Fermi level. What happens to the alignment of the UMOs in the monolayer? As we have already discussed in chapter 2, we cannot measure the energy position of the LUMO level with NEXAFS, since in the measurement we collect the electrons that are formed after the deexcitation of the system with one electron in the LUMO state but also one hole in the core. Therefore the measured LUMO level (that we will call LUMO*) will lie closer to the Fermi level with respect to the real LUMO. However we can assume that the shift will be the same for similar molecules. It can be deduced from fig. 4.27 that LUMO* level

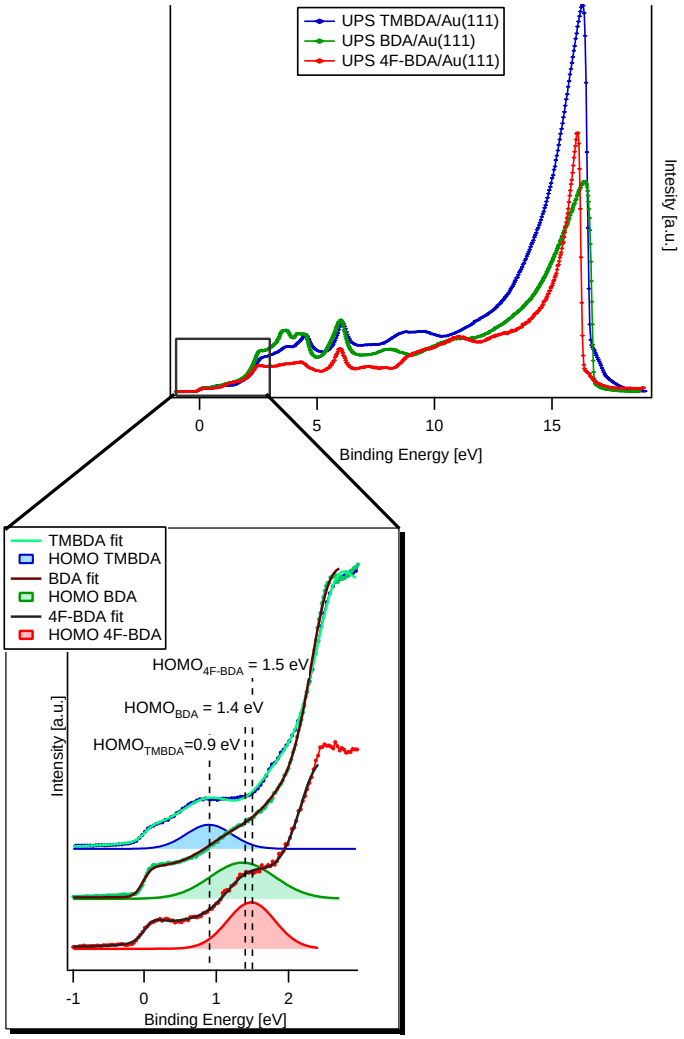

Figure 4.25: UPS (hv=21.2 eV, Bias=20 eV) spectra of monolayers of BDA, TMBDA and 4F-BDA on Au(111). In the bottom panel of this figure the region of the spectra close to the Fermi level is enlarged. The spectra were fitted in that region by using a Fermi edge, a Gaussian for the HOMO peak and a second Gaussian for the rest of the spectra. At the bottom of each spectrum the HOMO peak obtained from the fitting procedure is reported.

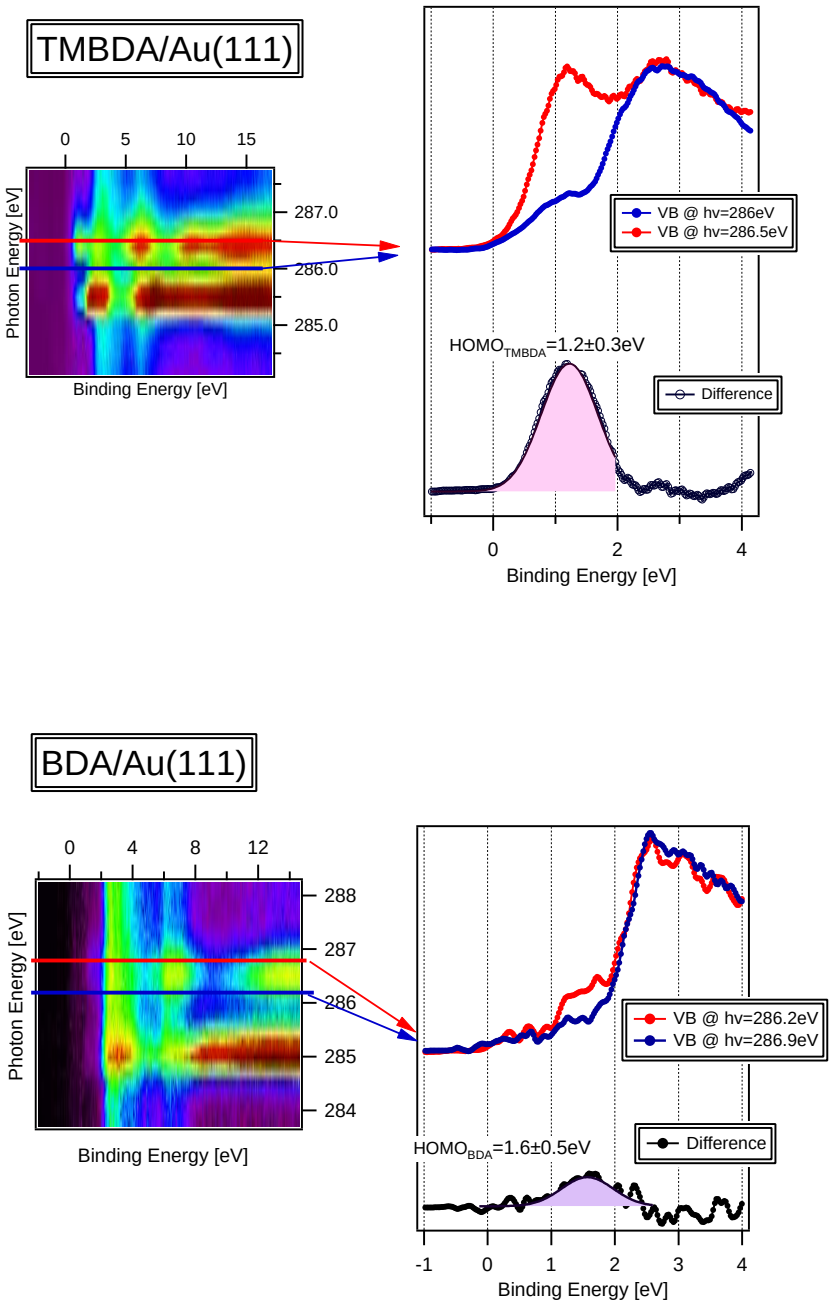

Figure 4.26: Carbon K-edge RPES of a monolayer of TMBDA on Au(111) (top image) and of a monolayer of BDA on Au(111) (bottom image). In the graphs on the right are reported two cuts at fixed photon energy of the RPES image on the right for photon energies on resonance and close to the resonance. On each graph is also reported the difference spectrum among the two y-sections in order to identify the position of the HOMO peak.

of the BDA is closer to the Fermi level than LUMO* level of the TMBDA. Therefore:

$$E_{LUMO}^{BDA} < E_{LUMO}^{TMBDA}$$

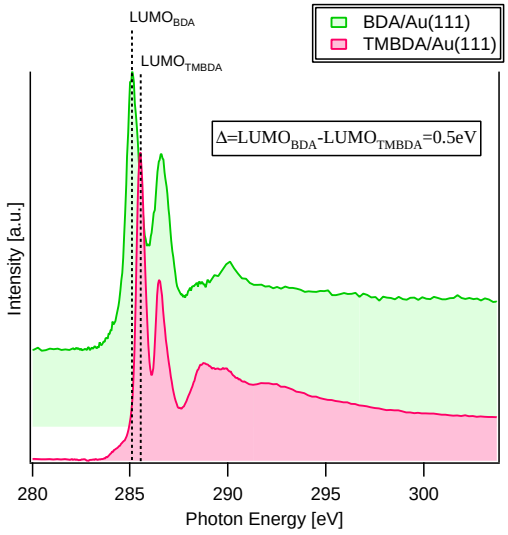

Figure 4.27: Carbon K-Edge NEXAFS spectra of a monolayer of BDA on Au(111) (green trace) and of a monolayer of TMBDA on Au(111) (red trace).

The measurements presented confirm the conduction model through HOMO for the family of molecules studied, but one more point has to be considered: the accordance with the numerical values. This is the main problem with the calculations, since moreover in the majority of cases the computed conductance for molecular junctions largely exceeds the measured values. The origin of the discrepancy between the measured conductance via break junction experiments and the computed one is related to the fact that the calculated tunnel coupling is intimately connected with the DFT derived orbital energies.

We will consider the case of Au-molecule-Au junctions formed with 1,4-Benzenediamine molecules [30]. In this case the calculated average conductance ($0.0046G_0$) in ref. [30] is 7 times larger than the measured one ($0.00064G_0$). The average in the calculation was performed on the conductance values of 15 different atom arrangements. The spread of the calculated values is quite narrow, only of 30%, indicating that the local amine-Au bond does not vary significantly across different junction geometries. Large variations in the molecular tilt angle and bonding configuration can be accommodated with relatively small variations in the Au-N-C bond (which ranges

from 112° to 130°) and N-Au bond lengths. Due to the intrinsic isotropy of the Au 6s orbital modest variations in local bond lengths and angles have minimal impact on the electronic coupling at the low biases relevant for the comparisons with the experiments.

In fig. 4.28 the calculated transmission probability for a specific junction is reported [30]. The transmission probability is proportional, as described, to the measured conductance via the Landauer formula. On the figure isosur-

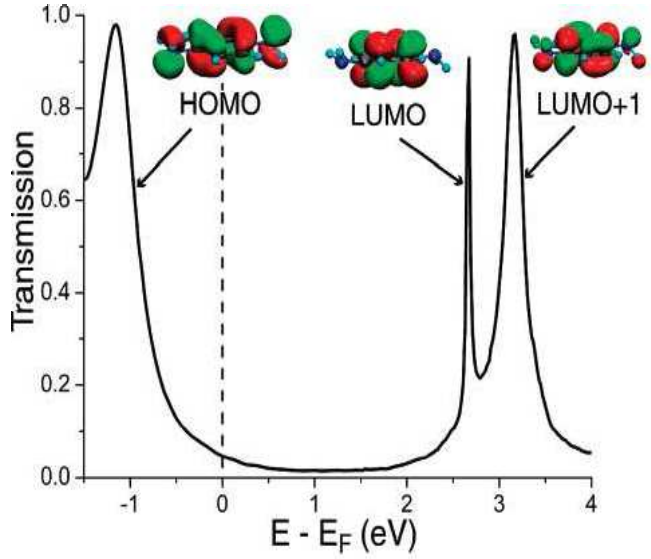

Figure 4.28: Energy-dependent transmission for a 1,4-BDA junction. Isosurface plots illustrate the molecular orbitals responsible for the transmission peaks. [30]

face plots are also reported illustrating the molecular orbitals responsible of the transmission peaks. In general, connecting the molecule to the contacts broadens and shifts the discrete states of the molecule. The broadening of the DOS depends on the strength of coupling to the contacts as well as to the wavefunction of the particular state. The transmission probability often resemble the DOS closely, but if the wavefunction for one level is asymmetric it may couple strongly to only one contact giving a wide DOS peak but a narrow transmission peak.

Given the small effects of the junction geometries on the conductance the authors in [30] exclude that origin of the discrepancy in the values arises from finite temperature fluctuations, and suggest that it can arise from the mean filed theory used in DFT: self-energy errors are introduced by the use

of (LDA or) GGA Kohn-Sham eigenvalues as quasiparticle energies. Two type of errors can be encountered: in the position of the energy levels, which corresponds to the position of the peaks in the transmission curve, or in the width of the peaks in the transmission curve, which is connected with the coupling of the molecule to the electrodes. Quek et al. [30] proposed the following correction to recover the conductance values. Since the self-energy corrections to the KS eigenvalues for small aromatic molecules are expected to be significant and large, whereas such corrections for metallic bulk and surface Au states would be relatively much smaller, especially for states near the Fermi Energy, they propose to correct the calculated values by first looking at the comparison between the experimentally measured ionization potential and the GGA HOMO eigenvalue for a gas phase BDA molecule (fig. 4.29, right). The calculated value in this case has to be corrected by $\Sigma_0^{HOMO} = -3$ eV. However electrostatic polarization of the Au contacts and to a lesser extent the surrounding solvent further modifies the electron removal energy (HOMO level) in the junction by an amount $\Delta\Sigma_0^{HOMO}$. By using a simple physically motivated image charge model [33] they estimate this contribution as $\Delta\Sigma_0^{HOMO} = 1$ eV. HOMO is therefore located at -3 eV from Fermi (fig. 4.29, right). The LUMO resonance is shifted away from Fermi by 2 eV and will not contribute to the low bias conductance. In performing this correction the width of the peaks in the transmission probability was not changed.

Having this model in mind, from our experimental results presented in this chapter we can extract two hints:

- The HOMO level of a BDA monolayer on Au(111) is at 1.6 eV from the Fermi energy and is shifted to lower energy by 0.5 eV with respect to the GGA calculated value in fig. 4.29. This shift is lower with respect to the 2 eV shift estimated by Quek et al. [30]. This difference can be due to the influence of the geometry of the contact to the correction for polarizability. In fact in the calculation a geometry with a cluster of atoms and not a (111) surface is considered. The distance of LUMO* from the Fermi level can be calculated as its energy position in NEXAFS (285 eV) minus the XPS position of the C1s (283.9 eV). Therefore LUMO* is separated from the Fermi level by 1.1 eV. The correction in order to have the energy of LUMO can be estimated from [34] and is at maximum 1 eV. Therefore the distance of LUMO from the Fermi level is about 2.1 eV. The same can be applied to the LUMO+1 level and it can be located at 3.6 eV with respect to the Fermi level.

- In the previous section we have concluded that the charge transfer in monolayers of BDA involves the LUMO+1 orbital. If we consider the

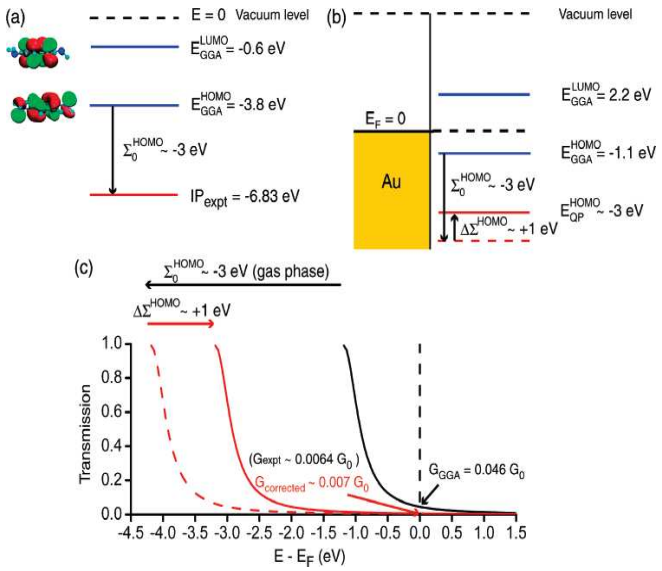

Figure 4.29: Energy level diagrams showing self-energy corrections in (a) the gas phase and (b) the junction. Σ_0^{HOMO} refers to self-energy correction to the GGA HOMO eigenvalue, E_{HOMO}^{GGA}, in the gas phase. In the junction, polarization effects result in a further self-energy correction, $\Delta\Sigma^{HOMO}$, to E_{HOMO}^{GGA}. (c) Changes in transmission curve and conductance due to self-energy correction to the HOMO level in a specific junction.

calculated transmission probability we can see that the peak widths at energies corresponding to HOMO and LUMO+1 levels are broader than the one of the peak corresponding to the LUMO level. These widths are a measurement of the coupling of the molecule to the electrodes, which is therefore different for different orbitals. From our measurements, confirming the theoretical predictions, we can conclude that the coupling is stronger for LUMO+1 than from LUMO. Although this is a qualitative observation, it is a clear point to be issued in the future by appropriate calculations in order to have a good estimation of the coupling to the electrodes.

In conclusion, if we consider the energies for the molecular orbitals determined and the widths of coupling, the conduction still takes place trough HOMO. It is interesting to note that the distance of the HOMO level from the Fermi level changes when considering a different surface. In the case of TMBDA, for example, for the monolayer on Au(111) the HOMO level is at 1.2 ± 0.3 eV from the Fermi level, while in the multilayer it is at 2.1 eV. By considering the Au(110), which has surface atoms with lower coordination, the HOMO position for TMBDA (fig. 4.30) is shifted by 0.5 eV to lower energy with respect to Au(111) (fig. 4.26). In the junction we expect this shift to be also different. What is needed at this point is a calculation for a monolayer of molecules that has to be compared with our experimental values in order to better understand the problem of the the overestimation of the conductance and to be able to predict correct values for HOMOs and LUMOs energies.

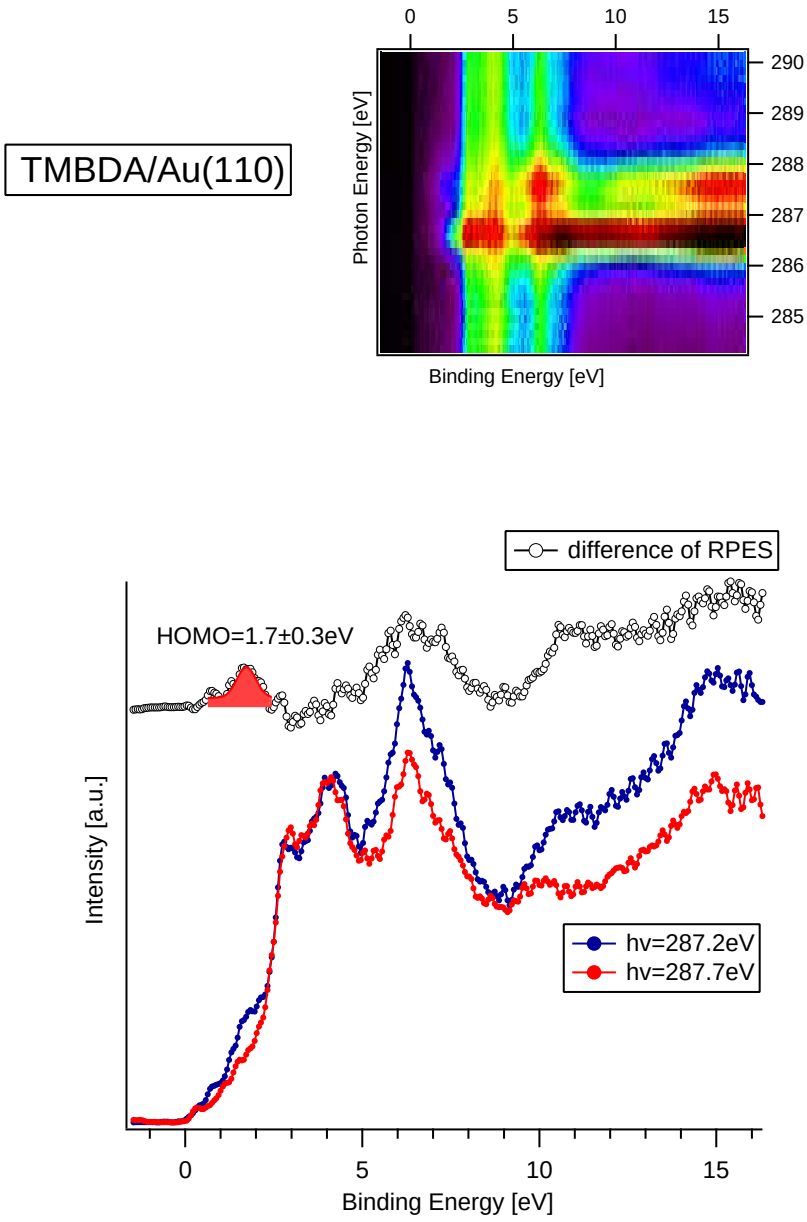

Figure 4.30: Carbon K-edge RPES of a monolayer of TMBDA on Au(110). In the bottom graph are reported two spectra with photon energies of 287.2 eV (close to the resonance) and 287.7 eV (in resonance) and the difference between them. The HOMO is found at 1.7 ± 0.3 eV.

Bibliography

[1] Aviram A., Ratner M.A., J. App. Phys. 42 (1974) 4398

[2] Xu B., Tao N.J., Science 301 (2003) 1221

[3] Reed M.A., Zhou C., Muller C.J., Burgin T.P., Tour J.M., Science 278 (1997) 252

[4] Smit R. H. M., Noat Y., Untied C., Lang N.D., van Hemert M.C., van Rultenbeek J.M., Nature 419 (2002) 906

[5] Venkataraman L., Klare J.E., Tam I.W., Nuckolls C., Hybertsen M.S., Steigerwald M.L., Nano Lett 6(3) (2006) 458

[6] Ji-Ming Z., Zhao-Yu R., Ping G., Jin-Shou T., Jin-Tao B., Chin. Phys. Lett. 25(4) (2008) 1423

[7] Park Y.S., Whalley A.C., Kamenetska M., Steigerwald M.L., Hybertsen M.S., Nuckolls C., Venkataraman L., JACS 129 (2007) 15768

[8] Schreiber F., Progress in Surface Science 65 (5-8) (2000) 151

[9] Venkataraman L., Klare J.E., Nuckolls C., Hybertsen M. S., Steigerwald M. L., Nature 442 (2006) 904

[10] Kim G., Wang S., Lu W., Nardelli M. B., Bernholc J., J. Chem. Phys. 128 (2008) 024708

[11] Cossaro A., Mazzarello R., Rousseau R., Casalis L., Verdini A., Kohlmeyer A., Floreano L., Scandolo S., Morgante A., Klein M.L., Scoles G., Science 321 (2008) 943

[12] Solomon J.L., Madix R.J., Stöhr J., Surf. Sci. 255 (1991) 12-30

[13] Crispin X., Solar Energy Materials & Solar Cells 83 (2004) 147

[14] Kugler Th., Thibaut U., Abraham M., Folkers G., Göpel W., Surf. Sci. 260 (1992) 64

[15] Richardson N.V., Frederick B.G., Unertl W.N., El Farrash A., Surf. Sci. 307-309 (1994) 124

[16] Oh S-Y., Yun Y.-J., Kim D.-Y., Han S.-H., Langmuir 15 (1999) 4690

[17] Hoft R.C., Ford M.J., McDonagh A.M., Cortie M.B., J. Phys. Chem. C 111 (2007) 13886

[18] Liu R., Shen W., Zhang J., Li M., Appl. Surf. Sci. 254 (2008) 5706

[19] Li Z., Kosov D.S., Phys. Rev. B 76 (2007) 035415

[20] Li X.-G., Huang M.-R., Duan W., Yang Y.-L., Chem. Rev. 102 (2002) 2925

[21] Akai N., Kudoh S., Nakata M., J. Phys. Chem. A 107 (2003) 6725

[22] Hennig C., Hallmeier K.H., Szargan R., Synthetic Metals 92 (1998) 161

[23] Otero E., Urquhart S.G., J. Phys. Chem. A 110 (2006) 12121

[24] Seah M.P., Smith G.C., Antony M.T., Surf. Interface Anal. 15 (1990) 293

[25] L. Floreano, G. Naletto, D. Cvetko, Gotter R, M. Malvezzi, L. Marassi, A. Morgante, A. Santaniello, A. Verdini, F. Tommasini, and G. Tondello, Rev. Sci. Instr. 70 (1999) 3855

[26] Stöhr Nexafs Spectroscopy, Springer-Verlag, Berlin, 1992

[27] NIST XPS database: Clark D.T., Kilcast D., Musgrave W.K.R., J. Chem. Soc. Chem. Commun. 517 (1971)

[28] Wang L., Liu L., Chen W., Feng Y., Wee A.T.S., JACS 128 (2006) 8003

[29] Schnadt J., Brühwiler P.A., Patthey L., O'Shea J.N., Södergren S., Odelius M., Ahuja R., Karis O., Bässler M., Persson P., Siegbahn H., Lunell S., Martensson, Nature 418 (2002) 620

[30] Quek S.Y., Venkataraman L., Choi H.J., Louie S.G., Hybertsen M.S., Neaton J.B., Nanolett. 7(11) (2007) 3477

[31] Venkataraman L., Park Y. S., Whalley A. C., Nuckolls C., Hybertsen M. S., Steigerwald M. L., Nonolett.7(2) (2007) 502

[32] Cahen D., Kahn A., Adv. Mater. 15 (2003) 271

[33] Neaton J.B., Hybertsen M.S., Louie S.G., Phys. Rev. Lett. 97 (2006) 216405

[34] Schnadt J., Shiessling J., Brühwiler P.A., Chem. Phys. 312 (2005) 39

[35] Zahid F., Paulsson M., Datta S., Electrical Conduction through Molecules, chapter in "Advanced Semiconductors and Organic Nanotechniques", H. Markoc, Academic Press (2003)

[36] Nitzan A., Annu. Rev. Phys. Chem., 52 (2001) 681

[37] Jortner J., Nitzan A., Ratner M.A., in Introducing Molecular Electronics, Springer Berlin/Heidelberg (2005) 13

[38] Hybertsen M.S., Venkataraman L., Klare J.E., Whalley A.C.,Steigerwald M.L., Nuckolls C., J. Phys. Condens. Matter 20 (2008) 374115

[39] Landauer R., IBM J. Res. Develop., 32 (3) (1998) 306

[40] McConnel H., J. Chem. Phys., 35 (1961) 508

[41] Duckers K., Bonzel H.P., Surf. Sci. 213, 25 (1989)

Chapter 5

Conclusions and Outlook.

In this thesis two systems employing organic molecules deposited on metal surfaces were studied. The aim of this research was the study of the fundamental role of the functional groups constituting the molecules in the formation of ordered self-assemblies on the surfaces and in the transfer of the charge to the surface. As already pointed out in the introduction, this research, that is at a fundamental level, is relevant for the development of future molecular electronics devices.

In the first part of the thesis the study of the self-assembly of L-methionine molecules on metal surfaces is presented. The employed experimental techniques have been Helium Atom Scattering (HAS), for the determination of the morphology of the assemblies, and X-ray Photoemission Spectroscopy (XPS) and Near Edge X-Ray Photoemission Spectroscopy (NEXAFS), for obtaining chemical information on the functional groups and on the bonding geometry. L-methionine is an aminoacid containing three functional groups (amino -NH_2, carboxyl -COOH and thioether C-S-C). Its self-assembly on the surface is driven by molecule-molecule and molecule-surface interactions that originate from the interactions between its functional groups and the surface and between the functional groups of different molecules. In particular, the most relevant type of intermolecular interaction for this system is the hydrogen bonding between the amino and the carboxyl groups: this interaction, that stabilizes the molecules in aminoacid solid crystals, plays a central role in the formation of ordered self-assemblies on the surface. We were interested in understanding the balance between all these interactions in the formation of ordered assemblies, and therefore we have studied L-methionine self-assemblies on different metal surfaces: Ag(111), Au(111), Cu(111) and Au(110). On Ag(111) and Au(111), ordered bidimensional nanogratings of molecules are formed with linear extension in the millimeter range. This structures, as pointed out in the introduction, may serve as use-

ful templates for building up other devices. I have been able to clarify the role of the L-methionine functional groups in the adsorption and therefore to construct the L-methionine self-assembly model: the thioether group is found responsible of the bonding of the molecule to the surface, while the amino and carboxyl groups are rather involved in the formation of hydrogen bond pairing (dimerization), that drives the formation of linear molecular chains. On Cu(111) the interaction with the substrate is stronger and the overall self-assembly ordering is temperature dependent. At temperatures below 250K the proposed adsorption scheme is similar to the Ag(111) and Au(111) case. However the final geometry of the assembly is quite different: instead of long chains of molecules, segmented molecular clusters are formed on the surface. The different geometry of the final assembly has been explained with molecules adsorbing as a different conformer to match the Cu(111) lattice parameter smaller than Ag(111) and Au(111). At temperatures higher than 250 K the molecules deprotonate and bind to the surface via all the functional groups giving rise to an assembly characterized by regular nanogratings. The Au(110) surface presents atoms with lower coordination with respect to the Au(111), that are preferential sites for the adsorption of the amino and thioether groups, as confirmed by our measurements. For all the surfaces considered in the thesis, we have identified the groups binding to the surface and explained how intermolecular hydrogen bonding and the consequent formation of extended chains are induced. An open question remains about the regularity of the nanogratings. A possible explanation is that they are originated by the confinement of the surface electrons, where the molecule to surface bond plays a central role. Besides future theoretical work in order to confirm this scenario, other experimental studies will be performed employing different aminoacid molecules. For example, it will be helpful to study the self-assembly of the L-norleucine. This molecule is analogous to the L-methionine but the sulphur atom is replaced by a carbon atom. This way we can study the role of the thioether group.

In the second part of this thesis I concentrated my attention in understanding the role of the amino functional group in binding the molecules to gold surfaces and in the charge transfer at the surface. In the future molecular electronic devices, complex molecules will be employed as active semi-conducting elements. For example, aminoacids are interesting building blocks for their self-assembly and self-ordering properties. A further step to have a good control on the device properties is to know from a fundamental point of view the role of each functional group in the bonding of the molecule to the electrode and in the charge transfer. I have started with the study of amino terminated molecules since STM Break Junction experiments performed in the group of prof. Latha Venkataraman (Columbia University,

NY), with whom I collaborate, have shown that the Au-single molecule-Au junctions present well-defined and reproducible single molecule conductance, in contrast to junctions employing molecules with thiol functionalizations. A lot of theoretical work has been performed in order to compute the conductance of these systems, but up to now the calculated values overestimate the experimental ones. The main problem in the theory resides in the approximations in the determination of the position of the molecular orbitals at the junction. In a tentative way to solve this problem, we have studied thin films of the amino terminated molecules deposited on gold surfaces. The information on the energy level position is experimentally available via X-ray spectroscopic techniques and may be exploited to model the theory. Therefore I have studied the assembly and the charge transfer of amino terminated aromatic molecules (1,4-Benzenediamine and p-toluidine) on Au(111) and Au(110) surfaces. The film growth was characterized by means of the XPS and NEXAFS techniques. In particular, both molecules adsorb in a flat configuration on Au(111) at low coverage. With increasing the coverage, the benzene rings tilt up in order to accommodate more molecules in the interface layer, always with the nitrogen towards the surface. On Au(110) the adsorption scheme is more complicated since we have identified different N1s XPS components that can be associated to different adsorption sites. Moreover we confirmed experimentally the theoretical predictions that the amino functional groups binds stronger to Au(110) surfaces with respect to Au(111), which is consistent with a preferential binding of the amino group to undercoordinated atoms. I have also studied the charge transfer of the molecular films by means of Resonant Photoemission Spectroscopy (RPES). I have identified the energy levels and the spatial distribution of the molecular orbitals. We observed that the charge transfer takes place via orbitals localized on the nitrogen atoms. This work is relevant as a test for the current theoretical calculations of molecular junctions and for the development of future electronic devices, since we have shown that by means of RPES it is possible to determine the energy level alignment at the molecule-surface interface. In general, the lone pair bonding scheme seems to be a good basis for the development of stable organometallic junctions. Future studies will employ molecules with different functionalizations presenting a lone pair, such as thioether or phosphine groups, and substrates other than Au, in order to identify good candidates for the building of the electronic devices by studying the energy levels and the spatial distribution of the molecular orbitals.

Aknowledgments

First of all I want to acknowledge my tutor prof. Alberto Morgante for introducing me in this field. Thanks for the continuous motivation and day by day help. Thanks for having helped me in finding the right scientific direction for my PhD.

Thanks to Latha Venkatamaran for introducing me to the STM-BJ technique, for the continuous scientific support and for the nice period I spent in her group.

Thanks to all the ALOISA group for help, support, suggestions and also for the nice time I spent with them: thanks a lot to Luca Floreano, Dean Cvetko, Alberto Verdini, Albano Cossaro and Gregor Bavdek. A special thanks goes to Albano Cossaro for his constant help, for the long long scientific discussions and for the "coffee time". Thanks to Alberto Verdini for reading and correcting this thesis. I want to thank also Francesco Bruno for teaching me how to use his program to analyze the data and, more important, for his friendship. The time we share the office was really a great time for me.

Finally I want to acknowledge all my friends, in particular Rossella, Cecilia, Laura ed Elham. Thanks to Paolo for the support in the last months and I could not forget to thank my family. Thanks specially to my parents, who always encouraged me to follow my motivations.